

https://dspace.org/

Synthesis of carbon nanofibers and their subsequent use as catalyst supports for Fischer-Tropsch synthesis

Phaahlamohlaka, Tumelo Nathaniel

2014-07-07
http://hdl.handle.net10539/14891

Downloaded from a DSpace repository. https://dspace.org/

Synthesis of carbon nanofibers and their subsequent use as catalyst supports for Fischer-Tropsch synthesis

By

Tumelo Nathaniel Phaahlamohlaka

Student Number: 674524

A dissertation submitted to the Faculty of Science, University of the Witwatersrand, Johannesburg, in fulfillment for the degree of Master of Science in Chemistry.

Promoter: Neil J. Coville

University of the Witwatersrand, Johannesburg. August 2013

DECLARATION

I declare that the dissertation, which is hereby submitted for a Master of Science at the Faculty of Science, University of the Witwatersrand, Johannesburg is my own unaided work and has not been submitted for examination at any institution.



Tumelo Nathaniel Phaahlamohlaka

On this 29th day of October 2013

DEDICATION

To my parents:

Esther and Mautu Phaahlamohlaka

”Now faith is confidence in what we hope for and assurance about what we do not see” Hebrews 11:1

ACKNOWLEDGEMENTS

I would like to express my sincere gratitude to my supervisor Professor Neil Coville for his wonderful insights and for giving me a chance to learn under his mentorship.

A great thank you! goes to Dr Shrikant Bhoware, Dr Ahmed Shaikjee, Dr Belina Terfasa and Ms Manoko Maubane for their showing me around the lab and their great inputs.

I am also grateful to Basil "Ecurie" Chaussoulas for helping set-up the Fischer-Trospch rig and some of the technical stuff in the labs.

The catalysis group together with Dr Linda Jewell for their valuable suggestions during the meetings.

I am grateful to the MMU (microscopy and microanalysis unit) and the XRD unit led by Prof. Alexander Ziegler and Prof. Dave Billing respectively for allowing some valuable instrument time. Dr. Rudolph Erasmus for Raman spectroscopy measurements.

I would like to thank NRF innovation scholarship, Bradlow, Ernst & Ethel Eriksen Trust and the University of the Witwatersrand post graduate merit award for financial support.

To the School of Chemistry and CATOMMAT members for being great colleagues and friends.

And finally thanks to the **Triune God**, in whom we all live, move and have our being

PRESENTATIONS

Tumelo Phaahlamohlaka, Manoko Maubane, Ahmed Shaikjee, Shrikant Bhoware, Neil Coville, *FTIR and RAMAN spectroscopy studies of carbon nanofibers produced by Cu catalyst – information to support a new carbon growth mechanism* (**Oral presentation**), SANI Nanosciences Young Symposium- Johannesburg, September 2012.

Tumelo Phaahlamohlaka, Manoko Maubane, Ahmed Shaikjee, Shrikant Bhoware, Neil Coville, *FTIR spectroscopy study of carbon nanofibers produced by Cu catalyst – information to support a new carbon growth mechanism* (**Poster presentation**), CATSA conference - Langebaan, November 2012.

Tumelo Phaahlamohlaka, Neil Coville, *Coiled carbon nanofibers as potential catalyst supports for Fischer-Tropsch Synthesis* (**Oral presentation**), DST center of excellence in catalysis (cchange) meeting , Wits and UCT- Johannesburg, March 2013.

Tumelo Phaahlamohlaka, Shrikant Bhoware, Neil Coville, *Raman spectroscopy Study of Carbon nanofibers: Structural evolution with annealing temperature* (**Poster presentation**), CoE-SM Annual Student Presentations, Johannesburg, May 2013.

Tumelo Phaahlamohlaka, Ahmed Shaikjee, Shrikant Bhoware, Neil Coville, *Synthesis and structural modification of carbon nanofibers for application as catalysts supports* (**Oral presentation**), Wits and UCT fuel cell meeting , Johannesburg, June 2013.

Tumelo Phaahlamohlaka, Neil Coville, *Application of carbon nanofibers as catalyst supports for Fischer-Tropsch synthesis* (**Poster presentation**), 5th annual Cross faculty symposium (at Wits), Johannesburg, August 2013.

PUBLICATIONS

1. Shrikant Bhoware, Manoko S. Maubane, **Tumelo Phaahlamohlaka**, Ahmed Shaikjee, Neil J. Coville: Cu grown carbon nanofibers – Variation of their chemical and physical properties, Chemical Physics Letters 577 (2013) 71–75
2. **Tumelo N. Phaahlamohlaka**, Neil J. Coville: Non graphitic carbon nanofibers application as catalysts supports in the Fischer-Tropsch synthesis (to be submitted)

TABLE OF CONTENTS

DECLARATION i

DEDICATION ii

ACKNOWLEDGEMENTS iii

PRESENTATIONS iv

PUBLICATIONS v

TABLE OF CONTENTS vi

ABSTRACT xii

LIST OF FIGURES xiv

LIST OF TABLES xviii

LIST OF ABBREVIATIONS xx

Chapter 1: Research question and hypothesis 1

1.1 Introduction 1

1.2 Aim 3

1.3 Objectives 3

1.4 Outline of dissertation 4

1.5 References 5

Chapter 2: Literature review 6

2.1 Growth of carbon nanomaterials using copper catalysts 6

2.1.1 Applications of copper metal 6

2.1.2 Theoretical studies on the capability of copper to act as a catalyst for carbon deposition. 7

2.1.3 Use of copper catalysts to synthesize carbon nanofibers 10

2.1.4 Use of copper catalysts to synthesize carbon nanotubes 14

2.1.5 Graphene growth on a Cu catalyst 17
2.1.6 Conclusion 21
2.1.7 References 22
2.2 Growth mechanism of carbon nanofibers/nanotubes: VLS versus VSS mechanism 30
2.2.1 Studies on the growth mechanism 30
2.2.2 Beyond the VLS mechanism paradigm 34
2.2.3 Proposed mechanism for low temperature (≤ 450 ℃) growth of carbon nanofibers 35
2.2.4 Proposed growth mechanism for high temperature (> 450 ℃) growth of carbon nanofibers 37
2.2.5 References 39
2.3 Overview of Fischer-Tropsch Synthesis (FTS) 42
2.3.1 FTS history 42
2.3.2 Fischer Tropsch synthesis and chemistry 43
2.3.3 Fischer-Tropsch synthesis mechanism 44
2.3.4 Fischer-Tropsch Synthesis catalysts 45
2.3.5 Supports for Fischer Tropsch Synthesis 45
2.3.6 Carbon nanofibers as supports in Fischer Tropsch Synthesis 46
2.3.7 References 46
Chapter 3: Experimental and characterization procedure for carbon synthesis and the Fischer-Tropsch process. 51
3.1 Method for synthesizing carbon nanofibers (CNFs) 51
3.2 Experimental procedure for Fischer-Tropsch synthesis 52
3.2.1 Gases 52

3.2.2 Catalytic reactor set-up 52
3.2.3 Measurements of the catalyst activity 55
3.2.4 Analysis of products 56
3.3 Mass balance and data analysis calculations 59
3.3.1 Equations employed for mass balance calculations 59
3.4 Characterization techniques 64
3.4.1 Transmission Electron Microscopy 64
3.4.2 Powder X-ray diffraction 65
3.4.3 Raman spectroscopy 65
3.4.4 Fourier Transform Infrared spectroscopy 65
3.4.5 Brunauer-Emmet and Teller surface area measurement 65
3.4.6 Temperature programmed reduction 65
3.5 References 66
4.1 Study and Characterization of Copper Oxide Nanoparticles 68
4.1.1 Introduction 68
4.1.2 Experimental 69
4.1.3.1 TEM, Transmission electron microscopy 71
4.1.3.2 XRD analysis of the four catalyst system 73
4.1.3.3 Temperature programmed analysis (TPR) 75
4.1.3.4 Calculating the surface area of Cu active sites under the reaction conditions. 77
4.1.3.5 Obtained surface areas of the different catalysts. 80
4.1.4 References 82
4.2 Synthesis of CNFs and purification by Soxhlet extraction 85

4.2.1 Synthesis of the carbon nanofibers 85
4.2.2 TEM analysis of the carbon nanofibers. 86
4.2.3 Effect of growth temperature on growth of carbon nanofibers. 90
4.2.4.2 IR spectroscopy 94
4.2.4.3 TGA and DTG analysis 95
4.2.4.4 Effect of preheating acetylene on the CNFS surface functional groups. 97
4.2.4.5 TGA analysis of the CNFs synthesized by preheating C_2H_2 98
4.2.5 References 100
4.3 Studies on the effect of annealing the CNFs 102
4.3.1 Introduction 102
4.3.3 FTIR spectroscopy of the CNFs annealed at different temperatures 104
4.3.4 Raman data of the annealed CNFs 106
4.3.5 Nitrogen adsorption-desorption results (BET) 108
4.3.6 XRD analysis 110
4.3.7 CNF mass loss during the annealing process 113
4.3.8 TEM images of the annealed carbon nanofibers 114
4.3.9 Concluding remarks 116
4.3.10 References 117
4.4 Functionalization of the carbon nanofibers 119
4.4.1 Introduction 119
4.4.2 Experimental 120
4.4.3 Results and discussion 120
4.4.3.1 BET surface area 120

4.4.3.2 Infrared spectroscopy of the CNFs 121
4.4.3.2 TEM analysis of the carbon nanofibers (CNFs) 124
4.4.3.3 Optimization of the functionalization process. 125
4.4.3.3.1 BET surface area 125
4.4.3.3.2 Infrared spectroscopy analysis 126
4.4.3.3.3 TEM analysis of the CNFs for functionalized using different acid solutions. 128
4.4.3.3.4 Raman spectroscopy analysis. 129
4.4.4 References 132
Chapter 5: Results and discussion: FT studies 134
5.1 Fischer-Tropsch catalytic studies using the helical and straight CNFs 134
5.1.1 Introduction 134
5.1.2 Experimental 135
5.1.2.1 Preparation of carbon nanofiber supported Fischer-Tropsch catalysts. 135
5.1.2.2 Catalysts preparation by urea deposition (HDP) 135
5.1.2.3 Catalysts preparation by hydrazine deposition (HDP). 135
5.1.2.4 Catalysts prepared by incipient wetness impregnation (IWI). 136
5.1.3 Results and discussion 136
5.1.3.1 TEM analysis 137
5.1.3.3 TPR analysis of the catalysts. 142
5.1.3.4 Fischer-Tropsch catalytic performance of the catalysts 143
5.1.4 Fischer Tropsch synthesis: Comparison of linear and helical CNFs as supports. 148
5.1.4.1 TEM analysis of the catalysts. 148

5.1.4.2 XRD studies. 150
5.1.4.3 Reduction profiles of the catalysts. 151
5.1.4.4 Fischer-Tropsch reactor studies. 153
5.1.4.5 Concluding remarks 156
5.1.5 References 156
Chapter 6: General conclussions and reccomendations 159
6.1 Conclusions 159
6.2 Recommendations 160

ABSTRACT

In this study the synthesis and use of carbon nanofibers (CNFs) as catalysts supports for Fischer Tropsch synthesis is reported. The synthesis of carbon nanofibers with two distinct morphologies was optimized based on the reports in the literature that the straight (SCNF) and helical (CCNF) carbon nanofibers grow on Cu catalysts with different particle sizes. To selectively grow CNFs with a single morphology Cu catalysts were designed using different synthesis procedures (by using unsupported, coated and silica supported catalysts). The prepared copper oxide (CuO) nanoparticles were characterized by techniques such as TEM, XRD and nitrous oxide chemisorption. These techniques showed that the unsupported and coated CuO catalyst precursors has large particle sizes (range 100-300 nm) and thus had low Cu atomic surface area, while the supported CuO catalysts displayed low particles sizes in the nanoscale regime (<20 nm) and hence had high atomic surface area. Preparation of CNFs was carried out 300 ℃ using acetylene (C_2H_2) gas as the carbon source. Cu catalysts with large particle sizes resulted in straight CNFs and the small supported Cu nanoparticles grew helical CNFs because of the change in the nanoparticle surface energy during adsorption of the acetylene gas and the silica (SiO_2) support effects that limited Cu nanoparticles from sintering (i.e. final particles size ~ 60 nm). Soxhlet extraction proved to be an invaluable step in removing adsorbed polycyclic aromatic hydrocarbons.

Because of the low thermal stability of these CNFs the materials were then annealed at higher temperatures ranging from 500-1400℃ in an inert environment (passing N_2 gas). The helical CNFs snapped under high temperature annealing (≥ 900 ℃) resulting in shorter lengths in comparison to the straight CNFs. BET analysis of the annealed CNFs indicated that the CNFs annealed at 500 and 900 ℃ have increased surface area and have a mesoporous pore structure with the surface area ranging from 200-350 m^2/g. Raman and Fourier transform IR spectroscopy indicated that the CNFs annealed at 500 and 900 ℃, (which were the main material of interest because of their high surface area and thermal stability) had different hybridized carbon content.

CNFs annealed at 500 ℃ contained both sp^2 and sp^3 hybridized carbon while annealing the CNFs at 900 ℃ resulted in a complete rehybridization of the carbon content to sp^2. The carbon sp^3 content in the CNFs annealed at 500 ℃ therefore implied that CNFs annealed at this temperature are more defective in comparison to the CNFs annealed at 900 ℃. Since it is well known that material functionalities are affected by the amount of defects present inside the different CNFs were then applied as catalyst supports for Fischer Tropsch synthesis (FTS) to compare the support effects on cobalt active sites.

The CNF surfaces were first modified by functionalization using concentrated HNO_3 solution. The preparation of the catalyst systems was performed by a simple HDP method using urea. The CNFs and the FT catalysts were characterized using different techniques such as XRD, TEM, BET, TPR and Raman spectroscopy. Reactor studies performed at 220 ℃ (P = 8 bar, GHSV= 1200 $mL.h^{-1}.g_{cat}^{-1}$) showed the catalysts had activities with CO conversion ranging from 25-45%. It was observed that catalysts supported on CNFs annealed at 500 ℃ displayed higher average activities of about $\pm$ 15% (based on the CO conversions) in relation to the catalysts supported on CNFs annealed at 900 ℃. Catalysts showed minimal water gas shift reaction and high methane selectivity (i.e. $\sim$ 20-30%) which can be attributed to the small Co crystallite sizes and low pressure reaction conditions.

LIST OF FIGURES

Figure 2. 1: Schematic of the VLS mechanism 7
Figure 2. 2: Turnover frequency vs. metal d orbital energy, scheme showing carbon atoms interaction on the surfaces across the transition metal series (A) [14], Three growth scenarios relative to the catalyst-CNT interaction, a for weak catalyst-CNT interactio n, a for weak catalyst-CNT interaction thus no growth scenarios d and e relevant for CNT growth (B) 8
Figure 2. 3: Copper–carbon binary phase diagram [12] 9
Figure 2. 4: Typical carbon nanofibers grown on copper catalysts at lower temperatures 11
Figure 2. 5: TEM images showing the evolution of the Cu NPs with acetylene exposure time, (a) 0 s, (b) 30 s, (c) 60 s, (d) 1 hour [30] 12
Figure 2. 6: Relationship between the gas-inducing, thermal and size effects on the carbon nanofiber morphology [34]. 13
Figure 2. 7: CNTs grown on Cu catalysts, aligned SWNTs with density of 2-6 nanotubes/µm- scale bar 10 µm (a), (b) [42], random SWNTs, scale bar SEM-200 nm, TEM-20 nm (c) [19], bamboo CNTs (d) [44]. 15
Figure 2. 8: Different synthesis methods for mass production of graphene (quality versus cost) [53] 17
Figure 2. 9: Graphic showing growth of graphene and is relationship to the amount of carbon on the Cu substrate [61]. 18
Figure 2.10: Raman spectra for graphene growth versus growth temperature (a). Average values of ID/IG and IG/I2D (b), Average values of linewidths of G and 2D graphene peaks from four different measurements (c). SEM images of graphene on Cu grown at different temperatures in 30 min (d–f) [64]. 20
Figure 2. 11: VLS growth mechanism showing both tip (a) and root (b) growth mechanisms 31
Figure 2. 12: ETEM image order showing a growing CNF at different time frames on the Ni catalyst (a-d) [8]. 32

Figure 2. 13: Moving from VLS (a, b and c) to a VSS (a, d and e) mechanism where surface chemistry of the nanoparticle plays an important role [1]..... 35
Figure 2.14: Energetically favourable adsorption sites for acetylene on Cu catalyst [17]..... 36
Figure 2. 15: Flow showing the polymerization of acetylene on Cu catalyst [17] 37
Figure 2. 16: Sketch showing the growth process (displaying both the extrusive and viscous force) [21] 38

Figure 3. 1: Horizontal CVD set up, (a) single and (b) double stage furnace..... 52
Figure 3. 2: Sketch of the fixed bed reactor employed in the FT reaction..... 53
Figure 3. 3: Schematic representation of the reactor and rig setup..... 55
Figure 3. 4: TCD of syngas trace using argon as carrier gas. 57
Figure 3. 5: TCD trace of calibration gas mixture using argon as carrier gas. 57
Figure 3. 6: FID trace of calibration gas mixture using nitrogen as carrier gas..... 58
Figure 3. 7: FID trace of the gaseous product stream. 58

Figure 4. 1: TEM images of CuOK..... 71
Figure 4. 2: TEM images of CuOK@SiO_2 72
Figure 4. 3: TEM images of CuONPs and CuONPs/SiO_2 72
Figure 4. 4: TEM images of CuO@LA/SiO_2..... 72
Figure 4. 5: (a) XRD patterns of the synthesized CuO catalysts and (b) the monoclinic CuO unit cell. 73
Figure 4. 6: TPR profiles of the CuO particles 76
Figure 4. 7: Typical gas trace during the nitrous oxide chemisorption process, nitrogen gas was eluted first followed by the unreacted nitrous oxide. Helium was used as the carrier gas. 80
Figure 4. 8: CVD setup used to grow the carbon nanofibers. 85
Figure 4. 9: Straight CNFs grown on the unsupported copper catalysts (CuOK) 86

Figure 4. 10: TEM images of CNFs(straight and helical) synthesised using (CuOK@SiO2)..... 86
Figure 4. 11: Faceted Cu nanoparticle and diameter distributions of the straight carbon nanofibers. 87
Figure 4. 12: Coiled CNFs grown on CuONPs/SiO_2 87
Figure 4. 13: Coiled CNFs grown by CuO@LA/SiO_2 87
Figure 4. 14: Faceted Cu nanoparticle and diameter distributions of the helical carbon nanofibers 88
Figure 4. 15: TEM images of SCNFs grown at 220 ℃ 91
Figure 4. 16: TEM images of SCNFs grown at 250 ℃. 91
Figure 4. 17: Possible PAHs in the carbon nanofibers samples [8] 92
Figure 4. 18: Soxhlet extraction set-up. 93
Figure 4. 19: IR spectra of the CNFs after different Soxhlet extraction times. 94
Figure 4. 20: TGA and DTG of the soxhlet extracted CNFs 96
Figure 4. 21: IR before and after Soxhlet extraction. 97
Figure 4. 22: TGA and DTG of CNFs obtained by pre-heating C2H2, before soxhlet (a) and (b), after soxhlet extraction (c) and (d) 99
Figure 4. 23: Relationship between Raman ID/IG and the correlation length (La) of sp2 clusters [4] 102
Figure 4. 24: CVD set-up used for annealing the CNFs 103
Figure 4. 25: FTIR spectra of the annealed carbon nanofibers SCNF post heated at 25 and 500 ℃ (a), 900 and 1400 (b). CCNF post heated at 25 and 500 ℃ (c), 900 and 1400 (d). 104
Figure 4. 26: Schematic displaying structural evolution of CNFs with annealing temperature 105
Figure 4. 27: Raman spectra of the carbon nanofibers, straight fibers (a), helical fibers (b), Typical spectrum of fibers annealed at 500 ℃ (c) and deconvoluted (using pseudo-Voigt function) Raman spectrum of CNFs annealed at 500 ℃ (d). 107
Figure 4. 28: Variation of surface area and pore diameter with temperature 109
Figure 4. 29: Variation of surface area and pore diameter with temperature 110

Figure 4. 30: XRD patterns of thermally treated carbon nanofibers, straight CNFs (a) and helical CNFs (b). 112
Figure 4. 31: possible defects and vacancies on the as synthesised CNFs (CCNFH25) (a-b), defects present after annealing (C4, C5 or C8 rings). 113
Figure 4. 32: TEM images of the straight annealed at different temperatures 25 ℃ (a), 500 ℃ (b), 900 ℃ (c) and 1400 ℃ (d). 115
Figure 4. 33: TEM images of the straight annealed at different temperatures 25 ℃ (a), 500 ℃ (b), 900 ℃ (c) and 1400 ℃ (d). 116
Figure 4. 34: IR spectra of the (a) CNFs functionalized at 80 ℃ using 55 % nitric acid and (b) Unfunctionalized CNFs. 123
Figure 4. 35: TEM images of functionalized CNFs, CNFH25 F80 (a), CNFH500 F80 (b), CNFH900 F80 (c), CNFH1400 F80 (d) and CNFH25 F80 magnified image (e and f). 124
Figure 4. 36: TEM images of the CNFs functionalized using different solution, CNFH900 F80 35%) (a), CNFH 900 F85 5hrs (b), CNFH900 NS 4:1 (c) and CNFH900 NS 1:1 (d) 128
Figure 4. 37: Raman spectra of annealed functionalized CNFs (annealed at 500, 900 and 1400 ℃), Functionalised using HNO_3 at 80 ℃ for 2 hours. 129
Figure 4. 38: Raman spectra of functionalized CNFs (optimization process) all annealed 900 ℃ 130

Figure 5. 1: Set up for hydrazine deposition reaction 136
Figure 5. 2: TEM images of 10% Co/SCNFH900 F80 2hrs IWI 138
Figure 5. 3: TEM images of 10% Co/SCNFH900 F80 2hrs HDP 138
Figure 5. 4: TEM images of 10% Co/SCNFH900 F80 2hrs N_2H_4 HDP 138
Figure 5. 5: TEM images of 10% Co/SCNFH900 F80 NS 4:1 HDP 139
Figure 5. 6: TEM images of 10% Co/SCNFH900 F85 4HRS HDP 139
Figure 5. 7: XRD patterns of the different FT catalysts. 140
Figure 5. 8: TPR profiles of the Cobalt oxide phase 142

Figure 5. 9: Catalytic activity over 120 hours on stream 145
Figure 5. 10: Column chart showing difference in activities and selectivities. 145
Figure 5.11: TEM images of Co supported on straight CNFs, (a) 10% Co/SCNFH500 and (b) 10% Co/SCNFH900 149
Figure 5. 12: TEM images of Co supported on helical CNFs, (a) 10% Co/CCNFH500 and (b) 10% Co/CCNFH900 149
Figure 5. 13: XRD patterns of the catalysts using S/CCNF supports 150
Figure 5. 14: TPR profiles Co catalysts supported on the annealed straight and helical CNFs 152
Figure 5. 15: Activity of the catalysts over 120 hours on stream (a)10% Co/SCNFH500 and 10% Co/SCNFH500, (b) 10% Co/CCNFH500 and 10% Co/CCNFH900 154
Figure 5. 16: Average activities and selectivities of the FT catalysts 155

LIST OF TABLES

Table 3. 1: Properties of the gas chromatographs employed 54
Table 3. 2: Molar response factors for hydrocarbon products 61

Table 4. 1: Crystallite size determination for CuOK using the Scherrer equation. 74
Table 4. 2: Reduction temperatures of the different CuO particles 76
Table 4. 3: Relationship of the atomic site densities and the maximum amount of nitrous oxide that can decompose assuming full monolayer coverage. 79
Table 4. 4: Calculated surface area of the Cu catalysts using N2O chemisorption determined from equation 4 and 5. 81
Table 4. 5: Carbon nanofiber yields. 89
Table 4. 6: Table illustrating the effect of growth temperature on the yield of the carbon nanofibers 91

Table 4. 7: Decomposition temperatures of the extracted straight carbon nanofibers. 96
Table 4. 8: Decomposition temperatures of the extracted straight carbon nanofibers 99
Table 4. 9: Raman D and G band peak position, intensity and area ratios of the CNFs 108
Table 4. 10: Surface area of the annealed SCNFs (straight carbon nanofibers) 109
Table 4. 11: Surface area of the annealed CCNFs (coiled carbon nanofibers) 110
Table 4. 12: Percentage mass loss during the annealing steps 114
Table 4. 13: BET results of functionalized CNFs at 80 ℃ using 55 % nitric acid. .. 121
Table 4.14: BET surface area and pore structure of the CNFs after functionalizing using the different acid solution. 126
Table 4. 16: Raman D and G band peak position, intensity and area ratios of the functionalized CNFs annealed at different temperatures. 130
Table 4. 17: Raman D and G band peak position, intensity and area ratios of the CNFs all annealed at 900 ℃ for functionalization optimization 131

Table 5. 1: Co metal loading and particle sizes of the catalysts. 141
Table 5. 2: Reduction peaks of the Cobalt oxide phases 143
Table 5. 3: Fischer-Tropsch synthesis performance on the cobalt catalysts. 147
Table 5. 4: Co metal loading and particle sizes of the catalysts. 151
Table 5. 5: Reduction peaks of the catalysts. 152
Table 5. 6: Catalytic performance of Co supported on the straight an helical CNFs 156

LIST OF ABBREVIATIONS

Abbreviation	Description
ASF	Anderson Schulz Flory
BET	Branauer Emmett Teller
CCNFs	Helical/coiled carbon nanofibers
CCVD	Catalytic chemical vapor deposition
CNFs	Carbon nanofibers
CNTs	Carbon nanotubes
CVD	Chemical vapor deposition
FID	Flame ionization detector
FTIR	Fourier Transform Infrared spectroscopy
FTS	Fischer-Tropsch synthesis
GC	Gas chromatography
GHSV	Gas hourly space velocity
HDP	Homogenous deposition precipitation
MWCNTs	Multi walled carbon nanotubes
PXRD	Powder X-ray diffraction
SCNFs	Straight carbon nanofibers
SWCNTs	Single walled carbon nanotubes
TCD	Thermal conductivity detector
TEM	Transmission Electron Microscopy
TGA	Thermo-Gravimetric Analysis
TPR	Temperature Programmed Reduction
WGS	Water gas shift
α	Alpha value

Chapter 1: Research question and hypothesis

1.1 Introduction

The explosive growth of the world population witnessed in the 20th and 21^{1st} century, has placed the finite supply of the planet's natural resources under an enormous strain. One of these resources is crude oil which has been the major source of energy over the past 100-200 years. However it is a non-renewable energy source and it is being depleted **[1]**. To counter this event it is of outmost importance that technologies that offer to produce crude oil alternatives are developed and enhanced to make use of every natural resource at our disposal **[2]**. One such technology that is known to offer great potential for the future energy security is Fischer-Tropsch synthesis (FTS) **[3]**. The FTS involves a reaction of syngas (mixture of H_2 and CO) over a supported catalyst to produce fuels and a wide range of chemicals. The syngas for the reaction can be obtained from different sources such as coal, natural gas and also renewable sources such as waste biomass **[3].** Fischer Tropsch synthesis is affected by the type of catalyst, support materials and promoter materials used together with the reaction conditions employed in the synthesis process **[4]**. The catalyst is at the core of the FTS reaction; however it requires an efficient support material to allow improved dispersion of the catalyst particles and to ensure efficient economic exploitation of the available metal.

In this study carbon nanofibers were used as catalyst supports for the FTS and evaluation of the carbonization (graphitization) and morphology of the CNFs on the activity and selectivity of catalysts in the reaction. Carbon nanofibers have previously been studied as catalyst supports for Fischer Tropsch synthesis **[5, 6]**. However the effect of the nanofiber morphology and the graphitic degree has not been reported. It is reasonable to suggest that if carbon nanofibers are to be efficient catalyst supports for highly dispersed active metals with longer lasting activity and constant selectivity, then the number of defects on the support surface has to be sufficient to immobilize

the metal nanocatalysts. This will avoid particle agglomeration. On the other hand the graphitic degree of the carbon nanofiber must also be high enough to avoid loss of the support material under the reaction conditions, The carbon nanomaterial defects have been observed by Graham et al. such that “docking stations” that were identified on the surface of the carbon nanomaterial were suggested to provide long term stability for Fe supported Fischer-Tropsch catalysts **[7]**.

In recent studies Cu catalysts have been shown to make carbon nanofibers (CNFs), and defects on the carbon materials synthesized using copper catalysts were introduced at the low temperatures used to make the CNFs. The defect content in the fibers can be modified by annealing the carbon materials at higher temperatures**.** The different carbon nanofiber morphologies also offer a variety of topological defects along the fiber axis.

Synthesis of CNFs with controlled morphology is still a challenge in the scientific community, partly due to the fact that many reaction variables influence the morphology of the CNFs **[8]**. Catalyst morphology has been observed to be the prime variable that determines how the synthesized carbon nanofibers are shaped **[9]**. Studies have shown that control of the carbon nanofiber morphology can be influenced to some degree provided that catalysts of narrow size and shape distribution are used under identical reaction conditions (temperature, suitable carbon precursor etc.). The different morphologies obtained for the carbon nanofibers can determine their influence on catalyst metal activity in the FTS reaction. A material’s functionality can be controlled by its defects which will define many of their physical properties and their operational lifetime. Carbon nanofibers with different morphologies and crystallinity may then be expected to offer different defects without the need of subjecting the support material to very harsh functionalization processes. A systematic study can show how these parameters can affect the active metal’s reducibility, selectivity and activity.

The degree of crystallinity and number of defects on a carbon material can easily be studied using suitable Raman active bands associated with the carbon. In particular, two important bands that can be observed are the Raman G-band at approximately 1590 cm^{-1}, A characteristic feature of the graphitic layers and a D-band at about 1350 cm^{-1}, A sign of the defective nature of the graphitic layers **[10]**. It has been well documented that the ratio of the band intensities associated with the bands (I_D, $I_{G)}$ give a measure of the defect structure of a carbon material.

The research questions that were posed in this project were:

1. How do sized and shaped metal nanoparticles control the morphology of the grown carbon nanofibers?
2. Does catalytic chemical vapour deposition method (CCVD) allow successful synthesis of carbon nanofibers with controlled morphology?
3. Do different carbon nanofiber morphologies and graphitization procedure affect the dispersion of the active metal particles?
4. How does the carbon nanofiber morphology and graphitization procedure affect the reducibility, selectivity and activity of the supported metal?

1.2 Aim

The aim of this project was to synthesis carbon nanofibers with distinct morphologies and to study the effect of CNF support morphology and defect content on the activity and selectivity of Co catalyst in Fischer Tropsch Synthesis.

1.3 Objectives

- Synthesize shape and size controlled metal copper nanoparticles for the synthesis of carbon nanofibers (CNFs).
- Synthesize CNFs using the prepared metal nanocatalysts by Catalytic Chemical Vapour Deposition (CCVD)

- Increase the structural stability of the CNFs by an annealing process at higher temperatures.
- Make cobalt catalysts supported on CNF for Fischer-Tropsch synthesis.
- Investigate the effect of carbon sp^2/sp^3 ratios on the metal-support interaction.
- Investigate the effect of the carbon nanofiber support on the particle size and reducibility of FT catalysts

1.4 Outline of dissertation

Chapter 1: Gives a research hypothesis, aim and objectives of the study.

Chapter 2: Gives a detailed review on the application of Cu for making CNFs, growth mechanism and a brief historical account of the Fischer-Tropsch synthesis.

Chapter 3: Shows the experimental procedure for synthesizing CNFs, the FT reactor setup and the calculations involved in the FT process.

Chapter 4: Reports on the synthesis and subsequent manipulation of the CNF properties to be applied as FT catalyst supports.

Chapter 5: Reports on the application of the treated CNFs as catalyst supports in the Fischer-Tropsch synthesis.

Chapter 6: The chapter provides conclusions and recommendations of this study.

1.5 References

1. Sorrell S, Speirs J, Bentley R, Brandt A, Miller R: **Global oil depletion: A review of the evidence**. *Energy Policy* 2010, **38**(9):5290-5295.
2. Kaufmann RK, Shiers LD: **Alternatives to conventional crude oil: When, how quickly, and market driven?** *Ecological Economics* 2008, **67**(3):405-411.
3. Khadzhiev SN, Krylova AY: **Fischer-tropsch synthesis in a three-phase system over nanocatalysts (review)**. *Pet Chem* 2011, **51**(2):74-85.
4. Jacobs G, Das TK, Zhang Y, Li J, Racoillet G, Davis BH: **Fischer–Tropsch synthesis: support, loading, and promoter effects on the reducibility of cobalt catalysts**. *Applied Catalysis A: General* 2002, **233**(1–2):263-281.
5. Keyser MM, Prinsloo FF: **Loading of cobalt on carbon nanofibers**. *Studies in surface science and catalysis* 2007, **163**:45-73.
6. Bezemer GL, Radstake PB, Koot V, van Dillen AJ, Geus JW, de Jong KP: **Preparation of Fischer–Tropsch cobalt catalysts supported on carbon nanofibers and silica using homogeneous deposition-precipitation**. *Journal of Catalysis* 2006, **237**(2):291-302.
7. Graham U, Dozier A, Khatri R, Bahome M, Jewell L, Mhlanga S, Coville N, Davis B: **Carbon nanotube docking stations: A new concept in catalysis**. *Catalysis letters* 2009, **129**(1-2):39-45.
8. Zhou J-H, Sui Z-J, Li P, Chen D, Dai Y-C, Yuan W-K: **Structural characterization of carbon nanofibers formed from different carbon-containing gases**. *Carbon* 2006, **44**(15):3255-3262.
9. Shaikjee A, Franklyn PJ, Coville NJ: **The use of transmission electron microscopy tomography to correlate copper catalyst particle morphology with carbon fiber morphology**. *Carbon* 2011, **49**(9):2950-2959.
10. Huang C-W, Wu H-C, Lin W-H, Li Y-Y: **Temperature effect on the formation of catalysts for growth of carbon nanofibers**. *Carbon* 2009, **47**(3):795-803.

Chapter 2: Literature review

2.1 Growth of carbon nanomaterials using copper catalysts

2.1.1 Applications of copper metal

Copper is a transition metal with an electron configuration of [Ar] $3d^{10}$ $4s^{1}$ in its zero oxidation state. It is also part of the coinage metal group of the Periodic Table and this gives it special physico-chemical properties as compared to other transition metals **[1]** . Copper metal has found many applications over the years in the electrical and construction industries, when applied as a bulk copper metal. The application of copper in many chemical and biological establishments requires that the copper metal be in the micro and nanoscale regime and this has opened up a new exciting field for nanotechnology applications using Cu metal. Copper nanoparticles attract interest in nanotechnology studies because Cu exhibits similar properties (such as a local surface plasmon resonance (LSPR) in the visible region) to those of silver and gold and importantly Cu is less costly than the silver and gold **[2, 3]**. Copper (I) based complexes also show some promise for application in dye-sensitized solar cells **[4]**. Copper metal nanoparticles have also found application in homogenous or heterogeneous catalysis for many organic chemistry reactions such as the Diels-Alder **[5]** and the so called click chemistry reactions **[6]**. Copper catalysts have also gained attention in other heterogeneous catalytic reactions such as the Water Gas Shift (WGS) **[7]** reaction to form hydrogen from the reaction of carbon monoxide and water vapor. In addition copper has also been used as a catalyst promoter for many catalytic reactions like the Fischer Tropsch synthesis **[8]** and in the synthesis of syngas (CO/H_2) by partial oxidation of methane **[9]**.

It is clear that copper has many potential applications based on its physico-chemical properties and these properties are affected by the size and shape of the metal particles. In this short review the use of copper as a catalyst for the synthesis of carbon (nano) materials will be examined. The effect of temperature and the particle

size together with the role of the carbon precursor in the carbon synthesis reaction is reviewed.

2.1.2 Theoretical studies on the capability of copper to act as a catalyst for carbon deposition.

Copper being a non-ferromagnetic metal was not traditionally considered for the growth of carbon nanomaterials in a mono-catalytic system. Metal such as Fe, Co and Ni were traditionally used to control the type of carbon material grown in a CVD process. Theoretical studies based on the ability of copper to catalyze carbon nanomaterial synthesis were based on the accepted growth mechanism. In this VLS (Vapor Liquid Solid) mechanism the carbon deposition is based on the dissolution of carbon into the bulk of a catalyst particle **[10, 11]**, and it is this mechanism that is/was mostly used to study the viability of copper as a catalyst to deposit carbon **[12, 13]**. The mechanism is described in Figure 2.1 below.

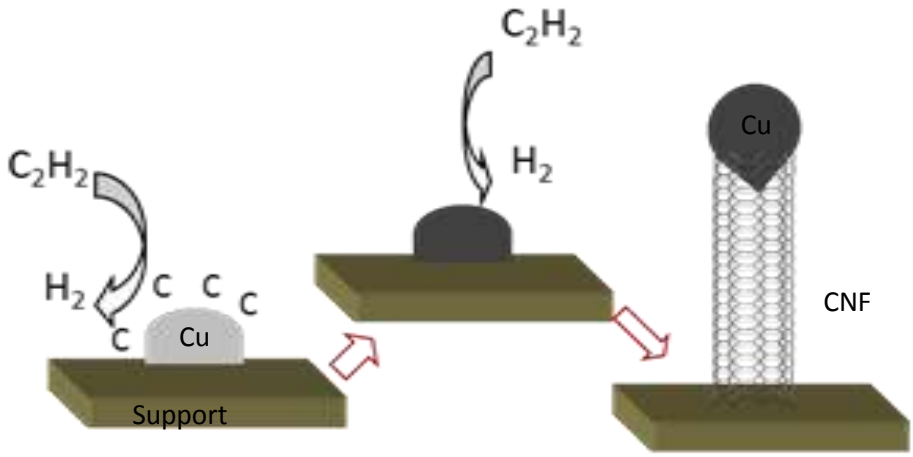


Figure 2. 1: Schematic of the VLS mechanism

Robertson studied the kinetics of the metal carbide bond for the first row transition metals. The study was based on the energy of the metal d orbital and the rate of interaction with carbon to form metal carbide. The calculated results gave a volcano plot (Figure 2.2 A) from which it can be inferred that Cu is not an ideal catalyst for

carbon nanomaterial synthesis since Cu forms weak metal-C bonds that do not rapidly dissociate the carbon source **[14]**. Molecular dynamics studies by Deng et al. were also used to examine a two stage growth model (nucleation and growth state) of carbon nanotubes on different metal catalysts. The calculations suggested that Cu is a poor catalyst for nucleation of C to form CNT because its electron configuration of [Ar] $4s^1 3d^{10}$ allows copper to form only a single carbon bond with a C_2 molecule resulting in the formation of an unstable carbon ring during nucleation. Copper energetics were also found to be less favourable in annealing CNT defects during growth as compared to a cobalt catalyst (energy barrier 2.22 eV for Cu vs. 0.065 eV of Co) **[15]**. Theoretical results by Ding et al. using molecular dynamics and DFT calculations indicated the inability of copper and some non-ferromagnetic metals to grow carbon nanotubes (SWNTs-both zigzag and armchair) was due to the poor adhesion energies (ranging from -3.7 to -1.8 eV for Cu) between the metal catalyst and carbon atoms of the growing filament. As a result there was a quick formation of a cap on the (base) nanotube which terminated the SWCNT growth prematurely (Figure 2.2 B) **[13]**.

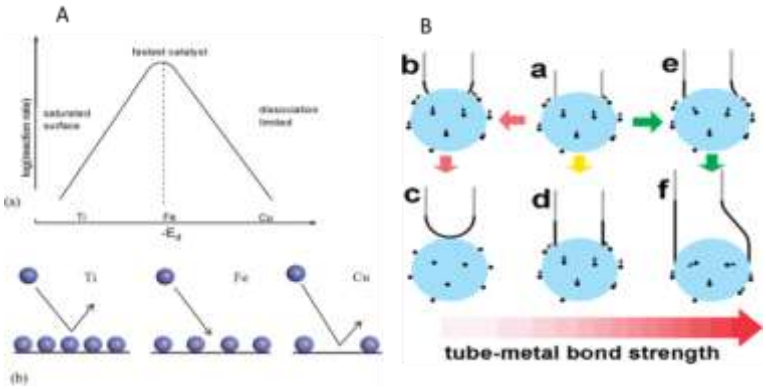


Figure 2. 2: Turnover frequency vs. metal d orbital energy, scheme showing carbon atoms interaction on the surfaces across the transition metal series (A) **[14]**,Three growth scenarios relative to the catalyst-CNT interaction, a for weak catalyst-CNT interaction, a for weak catalyst-CNT interaction thus no growth scenarios d and e relevant for CNT growth (B) **[13]**.

After observing that copper (and other non-ferromagnetic metals) was unsuccessful in catalyzing carbon nanomaterial growth at temperatures of 800-900 ℃. Deck et al. studied the metal-carbon binary phase diagram of Cu-C. It was observed that carbon displayed very low solubility in the Cu catalyst (< 0.0001%) even at high temperatures of 1100 ℃ **[12] (**Figure 2.3).

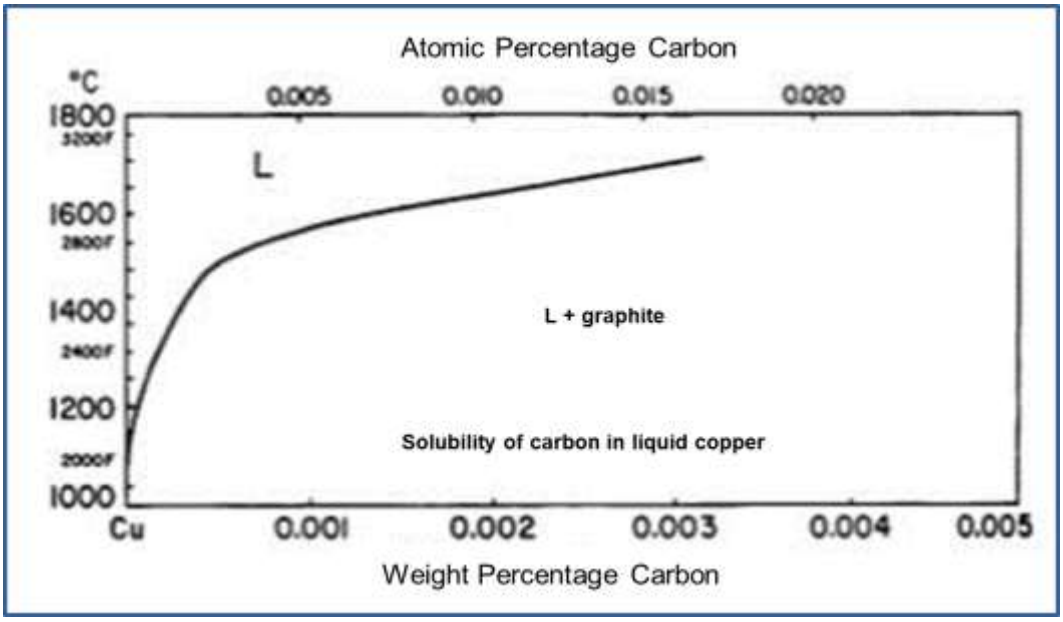


Figure 2. 3: Copper–carbon binary phase diagram **[12]**.

Although most of the theoretical studies on copper as a catalyst for carbon nanomaterial growth indicated that copper is not an ideal catalyst, studies done by Yazyev et al. gave results at odds to the majority of the other studies. In their studies DFT energy calculations were done on a Cu (111) surface, considering a three layer slab p (3×3) unit cells and (311) micro-faceted surface steps. The energy barrier for monoatomic carbon diffusion over copper catalysts when compared to nickel was found to be lower (0.07 eV vs. 0.39 eV). This implied that the use of a monoatomic carbon precursor (i.e. methane) can speed up carbon deposition on copper catalysts and that lower temperatures can be used to decompose CH_4 because of the very low diffusion barrier **[16].**

It is clear that from most theoretical work on the synthesis of carbon nanomaterials, copper is not expected to be an excellent catalyst for carbon growth. However the results differ from experimental results as it has been observed that copper can be used as a catalyst over a large temperature range (190-1000 ℃) to synthesise a myriad of carbon nanomaterials such as nanofibers, nanotubes (SWCNTs and MWCNTs) and graphene **[17-20]**.

2.1.3 Use of copper catalysts to synthesize carbon nanofibers.

Some of the earliest reports on the synthesis of carbon nanomaterials using copper generated carbon nanofibers (Figure 2.4). Different copper catalysts systems have been reported in the literature for the synthesis of carbon nanofibers ranging from Cu foils **[21, 22]**, unsupported Cu catalysts **[17, 23]**, as well as supported **[24]** and coated (encapsulated) **[25]** copper nanoparticles. Preparation of the catalyst particles has involved many techniques such as incipient wetness impregnation **[24]** for supported catalysts, while unsupported catalysts have been prepared by reduction **[18, 26]**, hydroxide precipitation **[27]** and high vacuum thermal decomposition **[28, 29]** of the Cu precursors. The methods have all been used in an effort to control the nanoparticle morphology which in turn would control the type (i.e. morphology) of carbon material deposited **[30, 31]**. Size and shape effects of the nanoparticles is have been observed when CNFs have been produced at lower synthesis temperatures **[30]**. The behaviour of the copper catalyst particles during growth of the carbon nanofibers is of great interest because unlike most of the other transition metal catalysts Cu gives symmetric growth of two carbon filaments from one catalyst nanoparticle **[22, 32]**. Most other metals give fibre growth in one direction only and the growth can be explained by a root or tip growth mechanism **[33].**

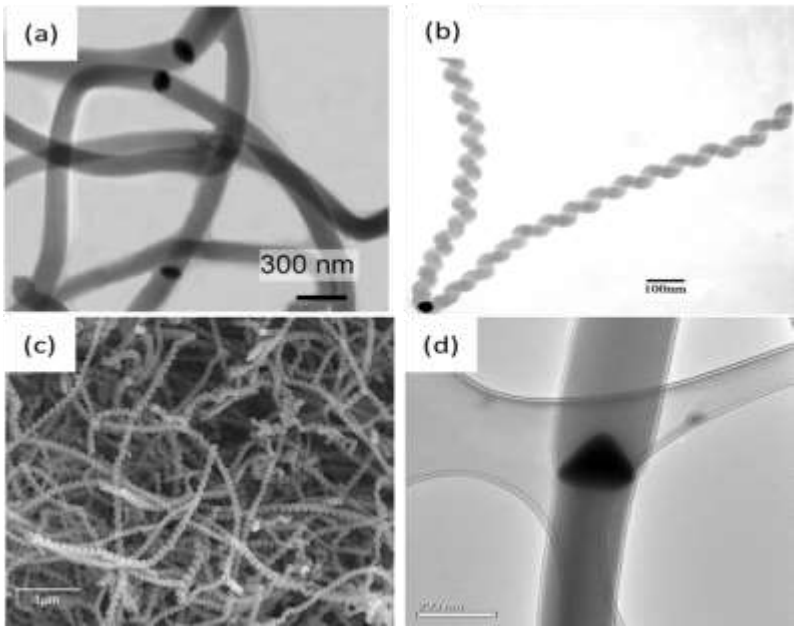


Figure 2. 4: Typical carbon nanofibers grown on copper catalysts at lower temperatures

The nanoparticle size affects the CNF morphology. It has been observed that small copper particles give highly faceted nanoparticles embedded in a coiled fiber **[18]** while larger particles, although also faceted, generally result in a growth of straight fibers **[26]**. The shape of the catalyst particles has an influence on the fiber morphology, Shaikjee et al. showed, using transmission electron microscopy tomography imaging, that pentagonal bypiramidal nanoparticles were imbedded in helical CNFs while straight CNFs had triangular plates imbedded in them **[30]**.

The crystallographic nature of the nanoparticles giving different CNFs also give contrasting results, Using selected area electron diffraction (SAED) Qin et al **[32]** presented evidence that the nanoparticles imbedded in the helical fiber are single crystals with {111} planes while straight fibers appear to form on polycrystalline Cu particles **[28]**. Although metal nanoparticles evolve from irregularly shaped particles before exposure to a carbon source, exposure generates new metal particle shapes. These new faceted nanoparticles formed during carbon deposition suggest that the

carbon source also has an important influence on the resulting carbon nanofiber properties **[30, 34]**,It is suggested that the reshaping of the catalyst nanoparticles happens during the chemisorption of the carbon source (Figure 2.5).

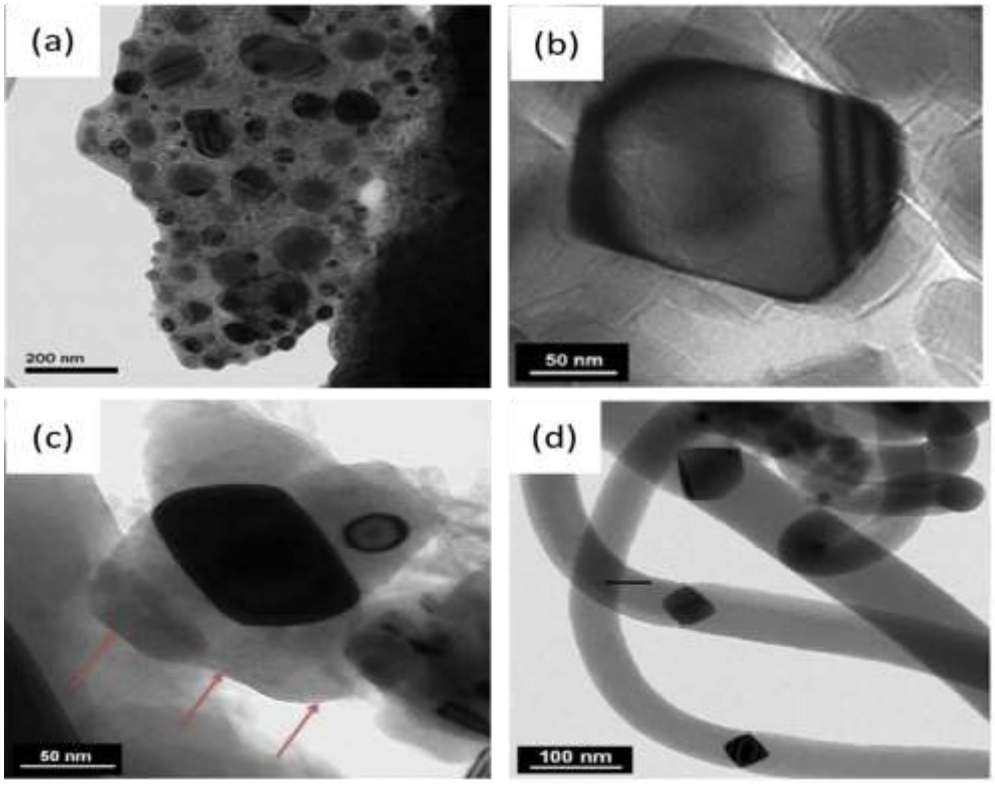


Figure 2. 5: TEM images showing the evolution of the Cu NPs with acetylene exposure time, (a) 0 s, (b) 30 s, (c) 60 s, (d) 1 hour **[30]**

Qin et al **[32]** concluded that catalyst reshaping is due to the change in surface energy of the exposed crystallographic planes which then results in the preferential formation of the low index {111} planes, which as mentioned above, are responsible for the growth of helical CNFs.

The role of the carbon source e.g. acetylene **[31, 34, 35]** or ethylene, which decompose easily on copper catalysts, also impacts on the shape of the Cu particles. Carbon sources such as methane and carbon monoxide do not give any substantial yields CNFs on copper catalysts at high and low temperatures **[36]**. The use of secondary gases together with the carbon source have also been noted to affect the carbon nanofiber morphology. Thus Li et al. showed that an ammonia/acetylene gas mixture increased the diffusion ability of copper nanoparticles (from the copper foil) on carbon materials and this resulted in the growth of vertically aligned CNFs while growth in the absence of ammonia gas yielded graphene films at reactor temperature of 350 ℃ **[22]**. In another case Jian et al. **[34]** studied the gas inducing effect of different secondary gases (H_2, N_2 and Ar) using DFT calculations. They observed that Ar and N_2 gas have very weak interactions with the copper nanocatalysts. Thus the inability to reshape the nanocatalysts resulted only in the formation of straight CNFs (Figure 2.6). The same studies were perfomed using H_2 as the secondary gas. H_2 displayed stronger interactions with the copper catalyst surface and this aided in the growth of helical CNFs.

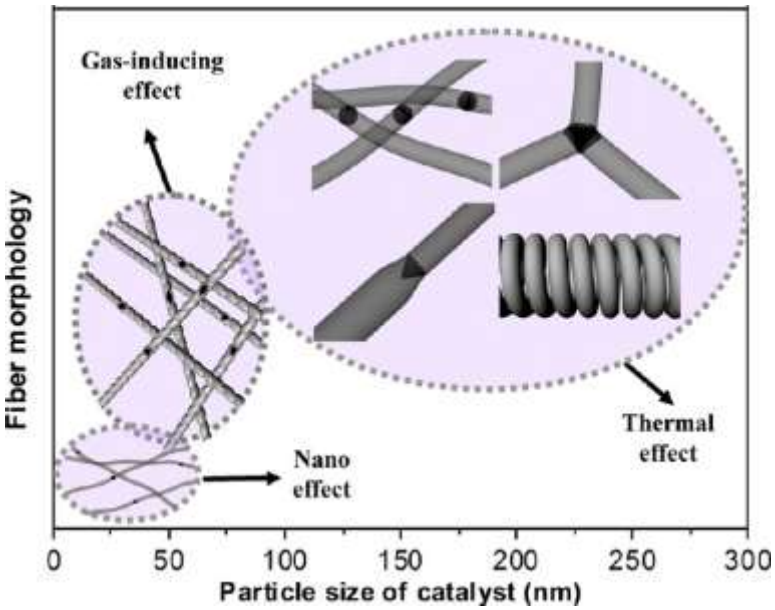


Figure 2. 6: Relationship between the gas-inducing, thermal and size effects on the carbon nanofiber morphology **[34]**.

The CNFs have been obtained with different morphological and graphitic nature dependent on the copper catalyst morphology (shape and size), the precursor gas and the reaction temperature **[21, 31, 37].** This is shown in Figure 2.6. The use of copper in the synthesis of the carbon nanofibers has been mostly centred in the low temperature regime of ≤ 450 ℃ **[38, 39]**. In this temperature region the catalysts give high carbon yields **[29]**, However there have been reports in which CNFs were grown on Cu catalyst at temperatures ≥ 500 ℃ **[36, 40]**. High temperature synthesis procedures result in the growth of mostly straight carbon nanofibers. Li et al. **[37]** observed that the synthesis of CNFs on a copper catalyst prepared by thermal decomposition gave coiled CNFs at 350 ℃ and straight fibres at 550 ℃, this may be attributed to catalyst particle sintering.

2.1.4 Use of copper catalysts to synthesize carbon nanotubes

The ability of copper metal/nanoparticles to serve as catalysts for the synthesis of carbon nanotubes has been reported in the literature (Figure 2.7). Most of the earlier reports were centred on the synthesis of single walled carbon nanotubes **[19, 41, 42]** although reports for the synthesis of multiwalled carbon nanotubes **[43]** have been noted. Studies have shown that copper catalysts provide an ideal template for the synthesis of SWCNTs since Cu grows much longer, cleaner and more aligned SWCNTs when compared to an Fe catalyst. This suitability of copper to outperform Fe in growing high quality SWCNTs is attributed to the inability of Cu to decompose the carbon precursor at a fast rate and consequently this improves the carbon feed rate resulting in the growth of high quality tubes **[41]**.

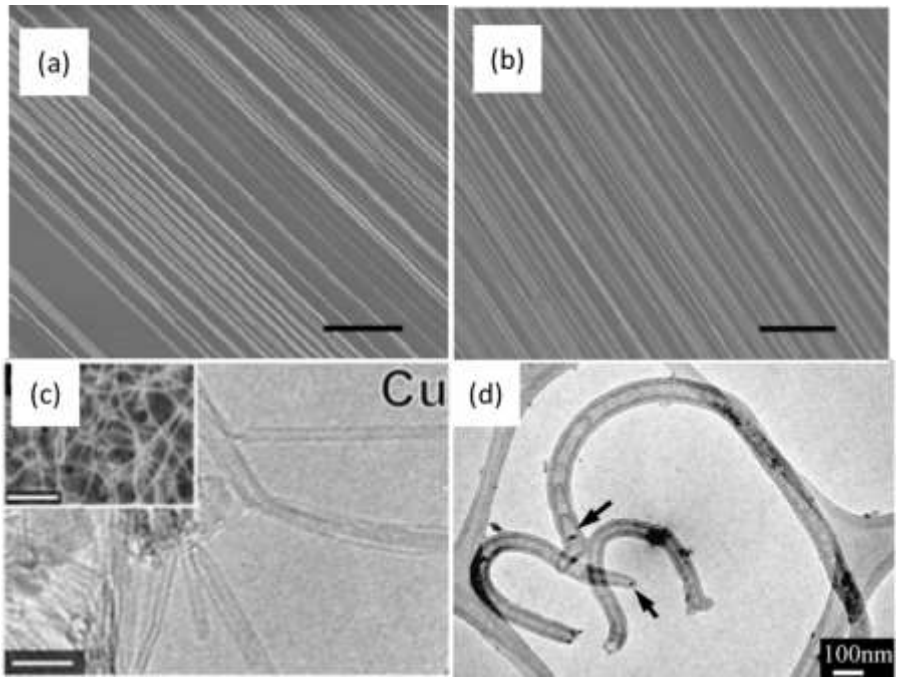


Figure 2. 7: CNTs grown on Cu catalysts, aligned SWNTs with density of 2-6 nanotubes/µm- scale bar 10 µm (a), (b) **[42]**, random SWNTs, scale bar SEM-200 nm, TEM-20 nm (c) **[19]**,bamboo CNTs (d) **[44]**.

Computational studies using first principle calculations by Yazyev et al, on Au, Pd, Ag and Cu nanoparticles, suggested that Cu as a catalyst for CNT growth is a good candidate for controlling the chirality of the carbon nanotube **[16]**. Growing carbon nanomaterials directly on the Cu metal gives a good electron transfer pathway which is advantageous in terms of electronic applications of the carbon nanotubes **[45].** Copper catalysts mostly employed in the synthesis of the carbon nanotubes typically involve the supported catalysts prepared by impregnation **[42, 43, 46, 47]** or copper foils **[19, 48].** The copper foils are sometimes loaded with a buffer layer (i.e. Cr or Ni) to promote the growth of aligned carbon nanotubes **[45, 49].** These Cu supported catalyst systems favour the growth of single walled carbon nanotubes **[41, 42, 46, 50, 51],** and other morphologies. Xue et al. **[43]** was able to grow bamboo like MWCNTs on a Cu supported on alumina catalyst prepared by impregnation**.** The synthesis temperature influences both the type of carbon nanotubes obtained and the activity of

the catalysts particles. Zhu et al. noted that the density of CNTs made on a Cu foil increased with increasing temperature (700-1000 ℃). However no growth of carbon nanotubes occured below 600 ℃. The carbon nanotube diameter also varied from 40-120 nm with changing temperature **[48].** Xue et al. found that the percentage yield of bamboo like carbon nanotubes increased with growth temperature (700, 750, 800) and then decreased at T> 800 (40%, 85% 95% and 90%) **[43]**.The increased yield of the carbon nanomaterials at higher temperature was credited to the rapid dissolution of the carbon precursor on the catalysts surface **[48].** Lin et al. were able to make carbon nanotubes at temperatures as low as 500 ℃ using a sulphate assisted copper catalyst supported on silica. Their results similarly indicated the usual trend of an increase in carbon yield with deposition temperature(500-900 ℃) **[47]**. Although it is evident that the growth of carbon nanotubes is possible at temperatures less than 600 ℃, the optimal deposition temperature for growing high yield and high quality CNTs is in the range of 700-1000 ℃. Growth temperatures below 700 ℃ give very low yields and might potentially result in the formation of carbon nanotubes mixed with a high content of amorphous carbon **[47, 48].** There are no reports of note on the growth of carbon nanotubes at temperatures above 1000 ℃ using copper catalyst**.**

Precursors that have been predominantly used to make CNTs over Cu catalysts include methane **[20, 41, 50, 51],** ethylene **[44, 47]**, acetylene **[52]** ethanol **[19, 20, 42, 43, 46, 48]** and methanol **[42]**. The reason that the different carbon precursors give high yields at high temperatures relates to the decomposition of the carbon at the high temperature. Catalyst pre-treatment procedures prior to the synthesis of carbon nanotubes are diverse. It is clear that both copper oxide and metallic copper are both able to grow CNTs when they come in to contact with the carbon precursors. Tagaki et al. **[19]** were able to grow SWCNTs on a copper catalyst activated by heat pre-treatment at 800 ℃ in air. Ding et al. treated copper catalysts with an oxygen plasma prior the growth of SWCNTs using an ethanol/H_2/Ar mixture **[46]**. There are numerous reports showing that pre-treatment of the copper catalyst with an inert gas (e.g. N_2) has no negative effects on the catalyst active site, as documented by Tao et

al. **[52]**, and Liu et al **[51]** who used Ar at 975 ℃. While this may suggest that the oxide catalyst particles catalyse the growth of nanotubes, the particles are reduced in-situ by the carbon source that generates the CNTs. Thus,Tao et al. observed by SAED that the catalyst particles inside the CNTs were metallic copper although the synthesis was initiated with an oxide catalysts without any pre-reduction **[51]**. For this reason synthesis procedures that involve prior activation of the catalyst by hydrogen reduction have been developed **[20, 42]**.

2.1.5 Graphene growth on a Cu catalyst

Graphene is a two dimensional single layer of carbon atoms with a honeycomb structure composed of sp^2-bonded carbon and this material has revolutionized thoughts about the future of many nano-electronic devices. This is because of the superior electron transport (≥15000 cm^2/Vs) of graphene compared to any other known material **[53]**. It is for this reason that methods have been devised to grow high quality and large area graphene **[54]** Although the initial report for obtaining monolayer graphene was based on mechanical exfoliation of graphite **[55],** chemical vapour deposition (CVD) of graphene on transition metals substrates (i.e Cu, Ni, Co and Fe) **[56]** has emerged as the most viable process to synthesize large area graphene (Figure 2.8).

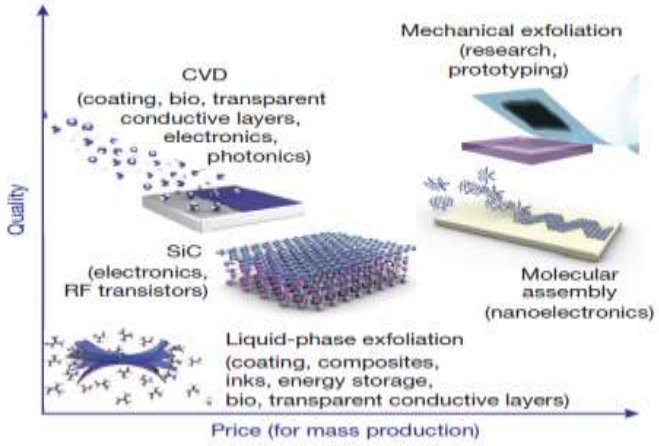


Figure 2. 8: Different synthesis methods for mass production of graphene (quality versus cost) **[53]**

Studies have shown that Cu foil is the metal of choice to grow lager monolayer graphene sheets. Graphene growth is a surface mediated process **[57]** and thus copper metal is an ideal catalyst because of the low solubility of carbon in copper and its inability to decompose hydrocarbons at a fast rate **[58]**. This renders the graphene growth on the copper metal to be a self-limiting process which is favorable for growth of a large area monolayer or few layer graphene **[56, 59, 60].**

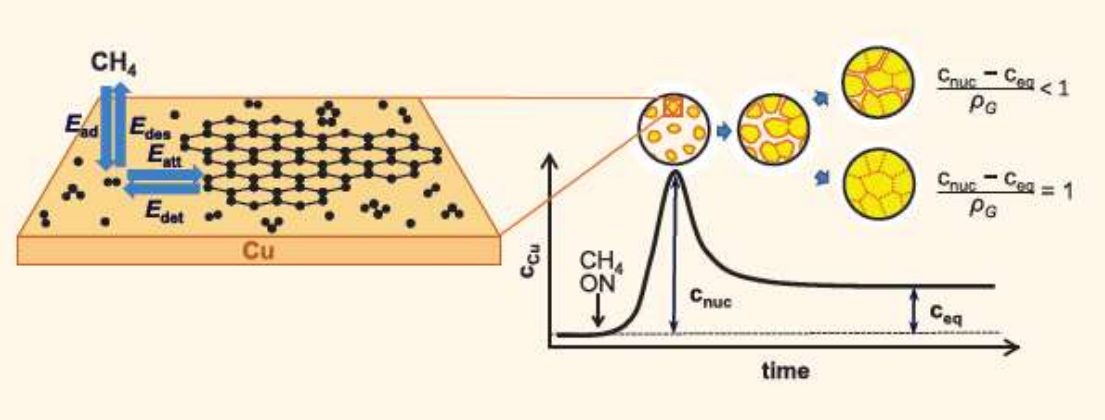


Figure 2. 9: Graphic showing growth of graphene and is relationship to the amount of carbon on the Cu substrate **[61]**.

Losurdo et al **[62]** observed that the reaction kinetics for the growth of graphene plays a very important role in controlling the number of the graphene layers. Kinetics studies of CVD growth of graphene have been performed on the hydrocarbon-hydrogen (CH_4-H_2) interaction with polycrystalline Cu and Ni foils using spectroscopic ellipsometry. The Cu foil showed different responses when interacting with hydrogen as compared to methane gas. An increased diffusion of hydrogen relative to methane on the Cu foil was noted. Thus an increased amount of H_2 in a CH_4-H_2 gas mixture impeded the chemisorption capability of the methane on a copper surface which resulted in the growth of graphene with a high defect density. The defect density was observed by IR reflection spectra (C-H, sp^3 defects) and Raman spectroscopy. Bhaviripudi et al. **[63]** suggested that one of the factors affecting the kinetics of graphene deposition on a Cu foil was the pressure in the

reaction chamber. They observed that the quality of the graphene grown at atmospheric pressure CVD (APCVD) varied with the methane concentration such that at low methane concentrations (≤100 ppm) single layer graphene (SLG) was formed while at high methane concentrations (5-10 %) multilayer non-uniform graphene was produced. The authors also noted that graphene growth is not a self-limiting process at high methane concentrations in an APCVD reaction chamber. However synthesis at low pressure CVD (P = 10 mTorr) resulted in a graphene sheet with a uniform thickness across large areas of the Cu foil. The obtained results showed that low pressure CVD is a useful way for synthesizing high quality graphene on low carbon solubility metal catalysts such as copper. Low pressure pre-treatment of the Cu foil also improved the regularity of the surface making the foil smoother with very small amounts of terraces and steps, thus allowing the growth of single layer graphene **[58]**. Cu metal is only able to grow graphene in a given temperature range by thermal chemical vapour deposition and the reaction temperature has also been recognized to be an influential parameter in the synthesis of single layer graphene on Cu **[61, 64, 65]**. Regmi et al. **[64]** studied the growth of graphene at different temperatures from 600-1000 ℃ at a pressure of 500 mTorr. They were able to determine by Raman spectroscopy (Figure 2.10) that no graphene was grown at growth temperatures below 850 ℃. The graphene grown at 850 ℃ is highly defective signaling the presence of multilayer graphene while only complete coverage of the Cu substrate is observed at temperatures above 950 ℃.

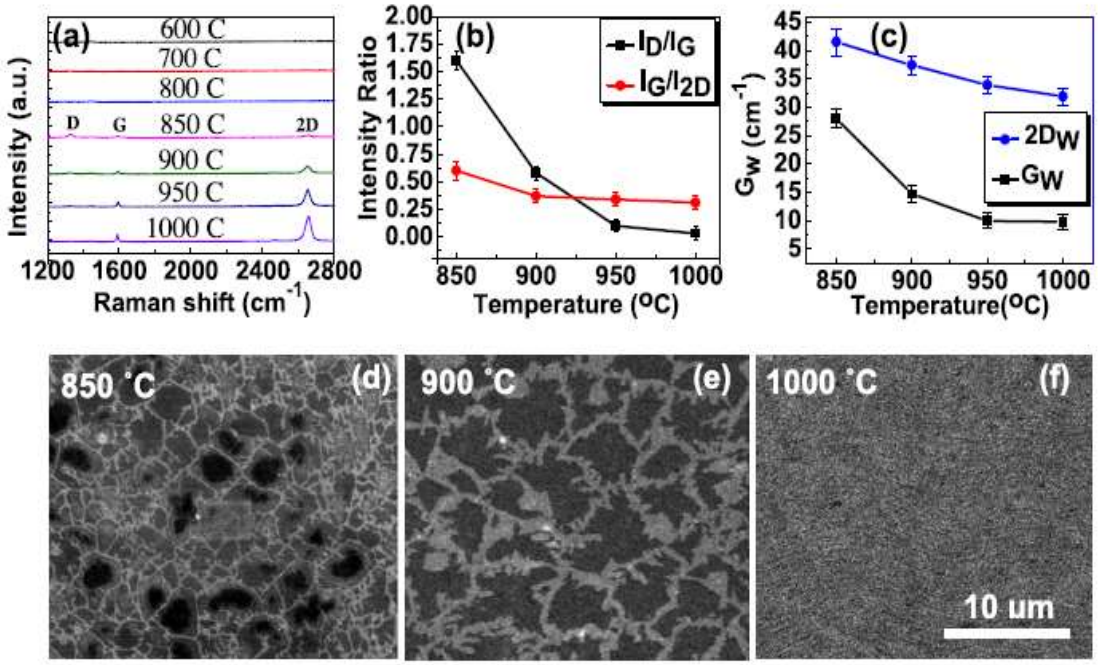


Figure 2.10: Raman spectra for graphene growth versus growth temperature (a). Average values of ID/IG and IG/I2D (b), Average values of linewidths of G and 2D graphene peaks from four different measurements (c). SEM images of graphene on Cu grown at different temperatures in 30 min (d–f) **[64]**.

Kim et al. **[61]** grew graphene on Cu in the temperature range of 720-1050 ℃. The Cu substrate displayed various degrees of surface roughness while annealing at 1000 ℃ smoothed the substrate. It was concluded using a nucleation model (Robinson and Robins model) that the energetics for graphene formation is dependent on temperature such that nucleation is controlled by carbon adatom capture at low temperatures < 870 ℃ and controlled by carbon desorption at higher temperatures > 870 ℃. The model is described by the equation $A_{sat} = |C_{nu} - C_{eq}|/ \rho_G$, (where; A_{sat}=saturated area, C_{nu}=number of nucleating carbon, C_{eq}=equilibrium carbon, ρ_G=graphene density and $C_{nu} - C_{eq}$=supersaturated fraction of carbon adatom

concentration. At temperatures above 870 ℃ , $A_{sat} \gg 1$ and at temperatures less than 870℃, $A_{sat} > 1$.

The most commonly used carbon source for synthesizing graphene on a Cu foil is methane **[62, 65-67]**. This is due to the fact that methane is not a highly reactive gas and consequently allows self-limiting growth of graphene on the substrate without forming many carbon intermediates (C_2, C_3, etc.) that can increase the amount of defects in the synthesized graphene. Other carbon precursors have been used and these include alcohols (i.e. methanol, ethanol and 1-propanol) **[68]** which gave monolayer growth of graphene at temperatures above 850 ℃. Hexane has also been used to fabricate single and few layer graphene on a polycrystalline Cu foil **[56, 69]**.The quality of the Cu foil substrate plays a significant role in the growth of low defect graphene. This is because defects on the substrate decompose a carbon source at a faster rate resulting in multilayer graphene. Liu et al. **[65]** studied graphene grown on Cu substrates with different purities (99.8 % and 99.999%) using LPCVD, By using Raman spectroscopy they observed that the 99.8% Cu substrate deposited bilayer graphene while a 99.999% Cu substrate yielded single layer graphene.

2.1.6 Conclusion

Copper metal was originally thought to be an inactive metal for the synthesis of carbon nanomaterials. Today it is known to have good catalytic activity for their growth. There is clear evidence from the studies mentioned that carbon nanofibers, nanotubes and graphene sheets are can be formed on a copper catalyst. The synthesis temperature plays an important role and determines the type of carbon material produced. The growth mechanism of the different carbon materials varies with the interaction of carbon sources with the catalysts. This disparity is brought about because of the different types of precursor gases that are used for the synthesis of morphologically different carbon nanomaterials. Copper is able to grow different carbon nanomaterials at different temperatures, (1) 200-400 ℃, growth of amorphous

carbon nanofibers (2) 500-800 ℃ growth of graphitic carbon nanofibers and carbon nanotubes (3) 750-1000 ℃ range for growth of graphene.

2.1.7 References

1. The transition metals [http://www.ucc.ie/academic/chem/dolchem/html/comp/transmet.html]
2. Dang TMD, Le TTT, Fribourg-Blanc E, Dang MC: **Synthesis and optical properties of copper nanoparticles prepared by a chemical reduction method**. *Advances in Natural Sciences: Nanoscience and Nanotechnology* 2011, **2**(1):015009.
3. Jin M, He G, Zhang H, Zeng J, Xie Z, Xia Y: **Shape-Controlled Synthesis of Copper Nanocrystals in an Aqueous Solution with Glucose as a Reducing Agent and Hexadecylamine as a Capping Agent**. *Angewandte Chemie International Edition* 2011, **50**(45):10560-10564.
4. Bozic-Weber B, Chaurin V, Constable EC, Housecroft CE, Meuwly M, Neuburger M, Rudd JA, Schonhofer E, Siegfried L: **Exploring copper(i)-based dye-sensitized solar cells: a complementary experimental and TD-DFT investigation**. *Dalton Transactions* 2012, **41**(46):14157-14169.
5. Reymond Sb, Cossy J: **Copper-Catalyzed Diels−Alder Reactions**. *Chemical Reviews* 2008, **108**(12):5359-5406.
6. Yamada YMA, Sarkar SM, Uozumi Y: **Amphiphilic Self-Assembled Polymeric Copper Catalyst to Parts per Million Levels: Click Chemistry**. *Journal of the American Chemical Society* 2012, **134**(22):9285-9290.
7. Gunawardana PVDS, Lee HC, Kim DH: **Performance of copper–ceria catalysts for water gas shift reaction in medium temperature range**. *International Journal of Hydrogen Energy* 2009, **34**(3):1336-1341.
8. Pansanga K, Lohitharn N, Chien ACY, Lotero E, Panpranot J, Praserthdam P, Goodwin Jr JG: **Copper-modified alumina as a support for iron Fischer–Tropsch synthesis catalysts**. *Applied Catalysis A: General* 2007, **332**(1):130-137.

9. Habimana F, Li X, Ji S, Lang B, Sun D, Li C: **Effect of Cu promoter on Ni-based SBA-15 catalysts for partial oxidation of methane to syngas**. *Journal of Natural Gas Chemistry* 2009, **18**(4):392-398.
10. Saito Y: **Nanoparticles and filled nanocapsules**. *Carbon* 1995, **33**(7):979-988.
11. Tessonnier J-P, Su DS: **Recent Progress on the Growth Mechanism of Carbon Nanotubes: A Review**. *ChemSusChem* 2011, **4**(7):824-847.
12. Deck CP, Vecchio K: **Prediction of carbon nanotube growth success by the analysis of carbon–catalyst binary phase diagrams**. *Carbon* 2006, **44**(2):267-275.
13. Ding F, Larsson P, Larsson JA, Ahuja R, Duan H, Rosen A, Bolton K: **The Importance of Strong Carbon−Metal Adhesion for Catalytic Nucleation of Single-Walled Carbon Nanotubes**. *Nano Letters* 2007, **8**(2):463-468.
14. Robertson J: **Heterogeneous catalysis model of growth mechanisms of carbon nanotubes, graphene and silicon nanowires**. *Journal of Materials Chemistry* 2012, **22**(37):19858-19862.
15. Deng W-Q, Xu X, Goddard WA: **A Two-Stage Mechanism of Bimetallic Catalyzed Growth of Single-Walled Carbon Nanotubes**. *Nano Letters* 2004, **4**(12):2331-2335.
16. Yazyev OV, Pasquarello A: **Effect of Metal Elements in Catalytic Growth of Carbon Nanotubes**. *Physical review letters* 2008, **100**(15):156102.
17. Qin Y, Jiang X, Cui Z: **Low-Temperature Synthesis of Amorphous Carbon Nanocoils via Acetylene Coupling on Copper Nanocrystal Surfaces at 468 K: A Reaction Mechanism Analysis**. *The Journal of Physical Chemistry B* 2005, **109**(46):21749-21754.
18. Qin Y, Zhang Q, Cui Z: **Effect of synthesis method of nanocopper catalysts on the morphologies of carbon nanofibers prepared by catalytic decomposition of acetylene**. *Journal of Catalysis* 2004, **223**(2):389-394.

19. Takagi D, Homma Y, Hibino H, Suzuki S, Kobayashi Y: **Single-Walled Carbon Nanotube Growth from Highly Activated Metal Nanoparticles**. *Nano Letters* 2006, **6**(12):2642-2645.
20. Zhou W, Han Z, Wang J, Zhang Y, Jin Z, Sun X, Zhang Y, Yan C, Li Y: **Copper Catalyzing Growth of Single-Walled Carbon Nanotubes on Substrates**. *Nano Letters* 2006, **6**(12):2987-2990.
21. Mata D, Amaral M, Fernandes AJS, Oliveira FJ, Costa PMFJ, Silva RF: **Self-assembled cones of aligned carbon nanofibers grown on wet-etched Cu foils**. *Carbon* 2011, **49**(7):2181-2196.
22. Li X, Xu Z: **One-step catalytic growth of carbon nanofiber arrays vertically aligned on carbon substrate**. *Materials Research Bulletin* 2012, **47**(6):1557-1561.
23. Zhang Q, Du F, Dong L, Hao C: **Formation of carbon fiber florets using copper tartrate catalyst precursors**. *Materials Letters* 2011, **65**(17–18):2779-2782.
24. Shaikjee A, Coville NJ: **The effect of copper catalyst reducibility on low temperature carbon fiber synthesis**. *Materials Chemistry and Physics* 2011, **125**(3):899-907.
25. Li X, Hao C, Lei Q: **Growth of carbon nanofibers catalyzed by silica-coated copper nanoparticles**. *Materials Research Bulletin* 2012, **47**(2):352-355.
26. Zhang H, Ren X, Cui Z: **Shape-controlled synthesis of Cu2O nanocrystals assisted by PVP and application as catalyst for synthesis of carbon nanofibers**. *Journal of Crystal Growth* 2007, **304**(1):206-210.
27. Bhoware SS, Maubane MS, Shaikjee A, Beas I, Ziegler A, Coville NJ: **Control of carbon helix fiber formation and fiber composition over Cu/SrO catalyst mixtures**. *Materials Research Bulletin* 2013, **48**(6):2347-2350.
28. Zhang Q, Cui Z: **Synthesis of coiled carbon nanofibers and Y-shaped carbon fibers**. *Journal of Physics: Conference Series* 2009, **152**(1):012069.

29. Qin Y, Zhang Z, Cui Z: **Helical carbon nanofibers prepared by pyrolysis of acetylene with a catalyst derived from the decomposition of copper tartrate**. 2003.
30. Shaikjee A, Franklyn PJ, Coville NJ: **The use of transmission electron microscopy tomography to correlate copper catalyst particle morphology with carbon fiber morphology**. *Carbon* 2011, **49**(9):2950-2959.
31. Zhang Q, Yu L, Cui Z: **Effects of the size of nano-copper catalysts and reaction temperature on the morphology of carbon fibers**. *Materials Research Bulletin* 2008, **43**(3):735-742.
32. Qin Y, Zhang Z, Cui Z: **Helical carbon nanofibers with a symmetric growth mode**. *Carbon* 2004, **42**(10):1917-1922.
33. Coville NJ, Mhlanga SD, Nxumalo EN, Shaikjee A: **A review of shaped carbon nanomaterials**. *South African Journal of Science* 2011, **107**:01-15.
34. Jian X, Jiang M, Zhou Z, Zeng Q, Lu J, Wang D, Zhu J, Gou J, Wang Y, Hui D *et al*: **Gas-Induced Formation of Cu Nanoparticle as Catalyst for High-Purity Straight and Helical Carbon Nanofibers**. *ACS Nano* 2012, **6**(10):8611-8619.
35. Yu L, Sui L, Qin Y, Cui Z: **Low-temperature synthesis of carbon nanofibers by decomposition of acetylene with a catalyst derived from cupric nitrate**. *Chemical Engineering Journal* 2008, **144**(3):514-517.
36. Nasibulina LI, Koltsova TS, Joentakanen T, Nasibulin AG, Tolochko OV, Malm JEM, Karppinen MJ, Kauppinen EI: **Direct synthesis of carbon nanofibers on the surface of copper powder**. *Carbon* 2010, **48**(15):4559-4562.
37. Li X, Xu Z: **Controllable synthesis of helical, straight, hollow and nitrogen-doped carbon nanofibers and their magnetic properties**. *Materials Research Bulletin* 2012, **47**(12):4383-4391.
38. Yu L, Qin Y, Cui Z: **Synthesis of coiled carbon nanofibers by Cu–Ni alloy nanoparticles catalyzed decomposition of acetylene at the low temperature of 241 °C**. *Materials Letters* 2005, **59**(4):459-462.

39. Ren X, Zhang H, Cui Z: **Acetylene decomposition to helical carbon nanofibers over supported copper catalysts**. *Materials Research Bulletin* 2007, **42**(12):2202-2210.

40. Borowiak-Palen E, Steplewska A, Rümmeli MH: **On the use of Cu catalysts for tailoring carbon nanostructures in alcohol-CVD**. *physica status solidi (b)* 2009, **246**(11-12):2448-2452.

41. Cui R, Zhang Y, Wang J, Zhou W, Li Y: **Comparison between Copper and Iron as Catalyst for Chemical Vapor Deposition of Horizontally Aligned Ultralong Single-Walled Carbon Nanotubes on Silicon Substrates**. *The Journal of Physical Chemistry C* 2010, **114**(37):15547-15552.

42. McNicholas TP, Ding L, Yuan D, Liu J: **Density Enhancement of Aligned Single-Walled Carbon Nanotube Thin Films on Quartz Substrates by Sulfur-Assisted Synthesis**. *Nano Letters* 2009, **9**(10):3646-3650.

43. Xue B, Liu R, Huang W-Z, Zheng Y-F, Xu Z-D: **Growth and characterization of bamboo-like multiwalled carbon nanotubes over Cu/Al2O3 catalyst**. *J Mater Sci* 2009, **44**(15):4040-4046.

44. Lin J-H, Chen C-S, Zeng Z-Y, Chang C-W, Chen H-W: **Sulphate-activated growth of bamboo-like carbon nanotubes over copper catalysts**. *Nanoscale* 2012, **4**(15):4757-4764.

45. Pan D, Ombaba M, Zhou Z-Y, Liu Y, Chen S, Lu J: **Direct Growth of Carbon Nanofibers to Generate a 3D Porous Platform on a Metal Contact to Enable an Oxygen Reduction Reaction**. *ACS Nano* 2012, **6**(12):10720-10726.

46. Ding L, Yuan D, Liu J: **Growth of High-Density Parallel Arrays of Long Single-Walled Carbon Nanotubes on Quartz Substrates**. *Journal of the American Chemical Society* 2008, **130**(16):5428-5429.

47. Lin J-H, Zeng Z-Y, Lai Y-T, Chen C-S: **Low-temperature growth of bamboo-like multi-walled carbon nanotubes over an atomic layer epitaxy-Cu/SiO2 catalyst via metal-support interaction**. *RSC Advances* 2013, **3**(6):1808-1817.

48. Zhu J, Jia J, Kwong F-l, Ng DHL: **Synthesis of bamboo-like carbon nanotubes on a copper foil by catalytic chemical vapor deposition from ethanol**. *Carbon* 2012, **50**(7):2504-2512.

49. Neupane S, Lastres M, Chiarella M, Li W, Su Q, Du G: **Synthesis and field emission properties of vertically aligned carbon nanotube arrays on copper**. *Carbon* 2012, **50**(7):2641-2650.

50. Yuan D, Ding L, Chu H, Feng Y, McNicholas TP, Liu J: **Horizontally Aligned Single-Walled Carbon Nanotube on Quartz from a Large Variety of Metal Catalysts**. *Nano Letters* 2008, **8**(8):2576-2579.

51. Liu Y, Hong J, Zhang Y, Cui R, Wang J, Tan W, Li Y: **Flexible orientation control of ultralong single-walled carbon nanotubes by gas flow**. *Nanotechnology* 2009, **20**(18):185601.

52. Tao X, Zhang X, Cheng J, Liu F, Luo J, Luo Z: **Morphology-Controllable CVD Synthesis of Carbon Nanomaterials on an Alkali-Element-Doped Cu Catalyst**. *Chemical Vapor Deposition* 2006, **12**(6):353-356.

53. Geim AK, Novoselov KS: **The rise of graphene**. *Nature materials* 2007, **6**(3):183-191.

54. Soldano C, Mahmood A, Dujardin E: **Production, properties and potential of graphene**. *Carbon* 2010, **48**(8):2127-2150.

55. Novoselov K, Geim AK, Morozov S, Jiang D, Zhang Y, Dubonos S, Grigorieva I, Firsov A: **Electric field effect in atomically thin carbon films**. *Science* 2004, **306**(5696):666-669.

56. Yao Y, Wong C-p: **Monolayer graphene growth using additional etching process in atmospheric pressure chemical vapor deposition**. *Carbon* 2012, **50**(14):5203-5209.

57. Li X, Magnuson CW, Venugopal A, An J, Suk JW, Han B, Borysiak M, Cai W, Velamakanni A, Zhu Y *et al*: **Graphene Films with Large Domain Size by a Two-Step Chemical Vapor Deposition Process**. *Nano Letters* 2010, **10**(11):4328-4334.

58. Liu W, Li H, Xu C, Khatami Y, Banerjee K: **Synthesis of high-quality monolayer and bilayer graphene on copper using chemical vapor deposition**. *Carbon* 2011, **49**(13):4122-4130.

59. Bae S, Kim H, Lee Y, Xu X, Park J-S, Zheng Y, Balakrishnan J, Lei T, Kim HR, Song YI: **Roll-to-roll production of 30-inch graphene films for transparent electrodes**. *Nature nanotechnology* 2010, **5**(8):574-578.

60. Li X, Cai W, An J, Kim S, Nah J, Yang D, Piner R, Velamakanni A, Jung I, Tutuc E: **Large-area synthesis of high-quality and uniform graphene films on copper foils**. *Science* 2009, **324**(5932):1312-1314.

61. Kim H, Mattevi C, Calvo MR, Oberg JC, Artiglia L, Agnoli S, Hirjibehedin CF, Chhowalla M, Saiz E: **Activation energy paths for graphene nucleation and growth on Cu**. *ACS Nano* 2012, **6**(4):3614-3623.

62. Losurdo M, Giangregorio MM, Capezzuto P, Bruno G: **Graphene CVD growth on copper and nickel: role of hydrogen in kinetics and structure**. *Physical Chemistry Chemical Physics* 2011, **13**(46):20836-20843.

63. Bhaviripudi S, Jia X, Dresselhaus MS, Kong J: **Role of kinetic factors in chemical vapor deposition synthesis of uniform large area graphene using copper catalyst**. *Nano Letters* 2010, **10**(10):4128-4133.

64. Regmi M, Chisholm MF, Eres G: **The effect of growth parameters on the intrinsic properties of large-area single layer graphene grown by chemical vapor deposition on Cu**. *Carbon* 2012, **50**(1):134-141.

65. Liu L, Zhou H, Cheng R, Chen Y, Lin Y-C, Qu Y, Bai J, Ivanov IA, Liu G, Huang Y: **A systematic study of atmospheric pressure chemical vapor deposition growth of large-area monolayer graphene**. *Journal of Materials Chemistry* 2012, **22**(4):1498-1503.

66. Ci L, Song L, Jin C, Jariwala D, Wu D, Li Y, Srivastava A, Wang Z, Storr K, Balicas L: **Atomic layers of hybridized boron nitride and graphene domains**. *Nature materials* 2010, **9**(5):430-435.

67. Terasawa T-o, Saiki K: **Growth of graphene on Cu by plasma enhanced chemical vapor deposition**. *Carbon* 2012, **50**(3):869-874.

68. Guermoune A, Chari T, Popescu F, Sabri SS, Guillemette J, Skulason HS, Szkopek T, Siaj M: **Chemical vapor deposition synthesis of graphene on copper with methanol, ethanol, and propanol precursors**. *Carbon* 2011, **49**(13):4204-4210.

69. Srivastava A, Galande C, Ci L, Song L, Rai C, Jariwala D, Kelly KF, Ajayan PM: **Novel liquid precursor-based facile synthesis of large-area continuous, single, and few-layer graphene films**. *Chemistry of Materials* 2010, **22**(11):3457-3461.

2.2 Growth mechanism of carbon nanofibers/nanotubes: VLS versus VSS mechanism

2.2.1 Studies on the growth mechanism

Over the past 20 years, efforts to understand the growth mechanism of shaped carbon nanomaterials (SCNMs) such as CNTs and CNFs have greatly advanced. In-situ and ex-situ techniques have been equally useful in producing reliable information about the carbon growth mechanism.

Components that influence the growth mechanism of carbon nanomaterials are **[1, 2]**

- Role of the hydrocarbon and its decomposition
- Chemical state of the metal catalyst before, during and after synthesis
- Chemical composition of the CNMs during the synthesis process

VLS mechanism

The vapour liquid solid (VLS) mechanism was first proposed for the growth of silicon whiskers **[3]**, The mechanism was then adapted by Baker et al. for growth of filamentous CNMs in the 1970s. It was observed that the synthesised filaments all have a metal particle at one end of the filament and the particle was distorted (pear shaped when observed under high magnification TEM). The distortion of the particle was attributed to the liquid phase characteristics of the catalyst nanoparticles under reaction conditions **[4, 5]**. It was proposed that a tip growth or a root growth process could account for the particle shapes (Figure 2.11)

The four fundamental steps in the VLS mechanism can be summarised as **[6]**:

- Adsorption of the carbon precursor on the catalyst surface
- Decomposition of the carbon source
- Diffusion of the growth species in or on the catalyst particle
- Nucleation and incorporation of carbon into the growing fibre.

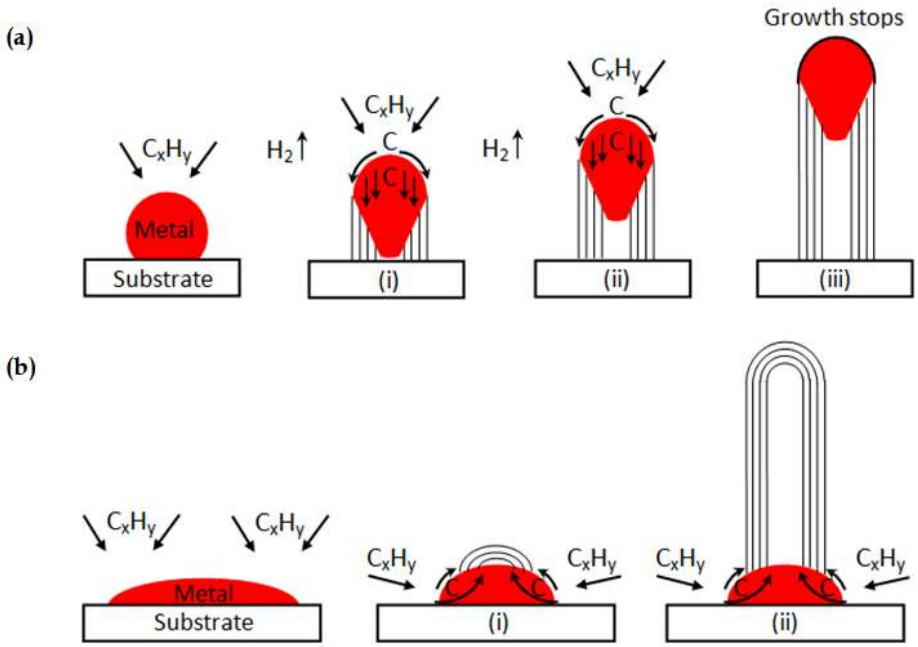


Figure 2. 11: VLS growth mechanism showing both tip (a) and root (b) growth mechanisms

When the activation energies of the individual steps are compared it is found that the third step which is the carbon diffusion through the metal catalysts is the rate determining step **[5]**. To explain how the diffusing carbon units move through the catalyst particle, Baker proposed that the driving force to explain the mobility of the diffusing carbon was the temperature gradient within the catalyst particle. The carbon source decomposed on the hotter faces of the catalyst and deposited on the cooler trailing facets of the catalyst **[4, 5]**. Another possible driving force for the diffusion of carbon in the bulk catalyst was proposed by Tibbets et al. **[7]**. The author proposed a model based on the decomposition of methane on an iron catalyst. In the model it was proposed that the active catalyst phase was austenite (Fe-C solid solution) which is at equilibrium with the precipitating carbon. The carbon that adsorbs on the surface is at higher chemical potential and this result in carbon diffusion through the catalyst particle. The change in enthalpy calculations, assuming that the methane decomposed only to graphite and hydrogen, revealed that (1) the energy flux on the catalyst

particle is not enough to induce a temperature gradient that will allow the carbon diffusion to be consistent with the observed fibre growth rate and (2) the concentration gradient was the primary cause of the carbon diffusion. Tibbets et al. **[7]** also maintained that bulk diffusion rather than surface diffusion of the carbon units is the most plausible route to the deposition of the extruding fibre.

In-situ studies using XPS and TEM have been used to verify the VLS mechanism. These techniques are used because post synthesis characterization can be unreliable because of the changes during cooling and sample transfer. Hoffman et al **[8]** reported using in-situ time resolved XPS during the growth of the CNFs on an iron catalyst at 580 ℃ that after exposure to acetylene three carbon XPS peaks were generated. The peak at 282.6 eV corresponding to chemisorbed carbon, an intermediate at 283.2 eV to carbidic carbon and third carbon peak at 284.5 eV to sp^2 carbon.

Further studies using ETEM (Environmental Transmission Electron Microscopy) Figure 2.12 showed that the catalyst (Ni) remained crystalline during the pre-treatment step, during the exothermic decomposition of the carbon and during the formation of the carbon fibre.

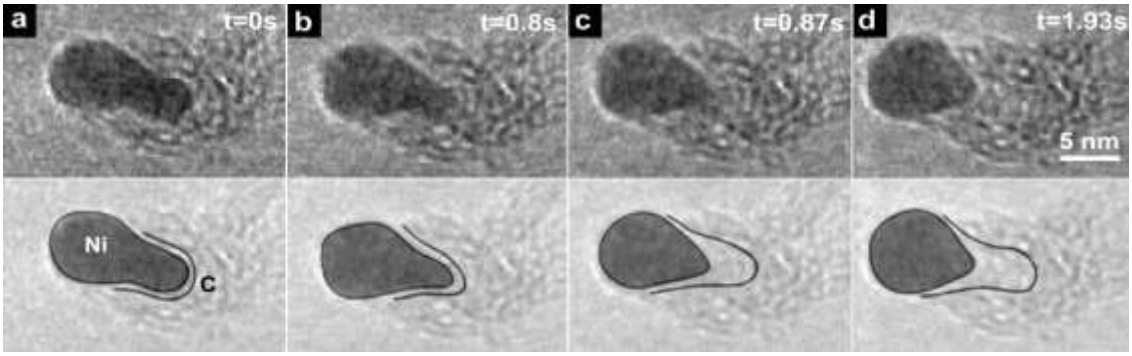


Figure 2. 12: ETEM image order showing a growing CNF at different time frames on the Ni catalyst (a-d) **[8]**.

The catalyst particle became elongated and then contracted to a round shape under reaction conditions. It was observed that the Ni NP behaved as a liquid but still

exhibited long range crystallinity **[8]**. An XPS study done by Hoffman et al. **[9]** on the evolution of C 1s peak and Ni/Fe $2p_{3/2}$ peak under C_2H_2 exposure were monitored. The C 1s main peak at 284.3 eV appeared within 50 s of exposure and saturated within 3 minutes for the Ni catalyst. Hoffman et al. observed that for an Fe catalyst the C 1s main peak appeared at 284.65 eV which then shifted to 284.45 eV after 6.5 minutes. This C 1s peak did not fully saturate in 20 minutes of growth time. It was concluded that the two peaks (at 284.45 eV for Fe and 284.3 eV Ni) can be attributed to CNT growth. The Ni/Fe $2p_{3/2}$ core level energy peak remained unchanged showing no phase transition (i.e. no formation of a solid solution between carbon and the catalyst nanoparticles). Furthermore, studies by Helveg et al. **[10]** based on in-situ HR-TEM on the growth of carbon nanotubes at a temperature range of 500-540 ℃ indicated that the nucleating and growing graphene layers helped to restructure step edges on the Ni surface with the Ni being in a liquid like-phase, The DFT studies indicated that the observations were consistent with a growth mechanism involving surface diffusion of carbon on the nickel atoms. It was thus observed that the VLS mechanism although quite feasible is unable to completely explain the discussed experimental results.

Results based on the Bronsted-Evans-Polany volcano plot showed that the most efficient catalyst systems for the growth of carbon nanofibers/tubes are the ones which are able to form slightly-stable carbides and that allow sufficient carbon dissolution into the bulk at reaction conditions. Using this plot, early transition metals are proposed to be poor catalysts since they form strongly bound carbides and late transition metal are poor catalysts because the carbon precursor is very weakly adsorbed on the catalyst particle and the precursor is likely to desorb before decomposition **[11]**. A recent in-situ XRD study by Podyacheva et al **[12]** on a Ni-Cu (0.85:0.15) alloy for the growth of CNFs at 550 ℃ suggested that carbon does dissolve into the bulk catalyst. This is because of the observed linear increase in the alloy parameter from 3.561-3.575 Å in the first few minutes of reaction. The lattice parameter then stabilises between 3.573-3.575 Å after 7 minutes with the appearance

of the carbon phase. Catalyst particles remain solid throughout the experiment as recorded using the in-situ XRD.

From these mentioned results it can be deduced that there is sufficient evidence that carbon dissolution in the metal catalysts is a possible pathway during carbon deposition. The latest studies on the VLS mechanism show that the idea that the metal catalyst is liquid at reaction temperatures is not supported by in-situ studies. It was also shown than surface diffusion on metal nanoparticles is more favoured that bulk diffusion thus supporting a surface diffusion mechanism called the vapour solid solid (VSS) mechanisms **[1, 10]**. In the VLS and VSS mechanism the third step which is the diffusion pathway of the carbon species is an important step and all the other steps are not rate determining steps. This premise can only hold true at higher reaction temperatures (≥ 500 ℃). At lower temperatures the gas phase composition of the nucleating carbon species plays an important role in the shaping of the catalyst and the morphology of the carbon nanomaterials. Thus steps 1 and 2 in the VLS or VSS mechanisms are important **[2]**.

It has been observed that the synthesis of carbon nanomaterials can be attained at lower temperatures (≤ 450 ℃) on transition metals **[13-15].** This indicates the inadequacy of the traditional VLS mechanism to explain the growth of carbon at lower temperatures.

Carbon nanofibers synthesised at lower temperatures especially using copper catalysts have been shown to contain large amounts of hydrogen and alkyl groups making the carbon materials amorphous with distorted lattice arrangements and the VLS mechanism is not able to account for this growth **[16, 17]**.

2.2.2 Beyond the VLS mechanism paradigm

In a recent review, Tessonier et al. **[1]** proposed that the vapour solid solid (VSS) mechanism is the most viable growth mechanism for the deposition of filamentous carbon nanomaterials (Figure 2.13). This is because the mechanism does not require

bulk diffusion through metal nanoparticles by carbon units to be the driving force in growing carbon materials.

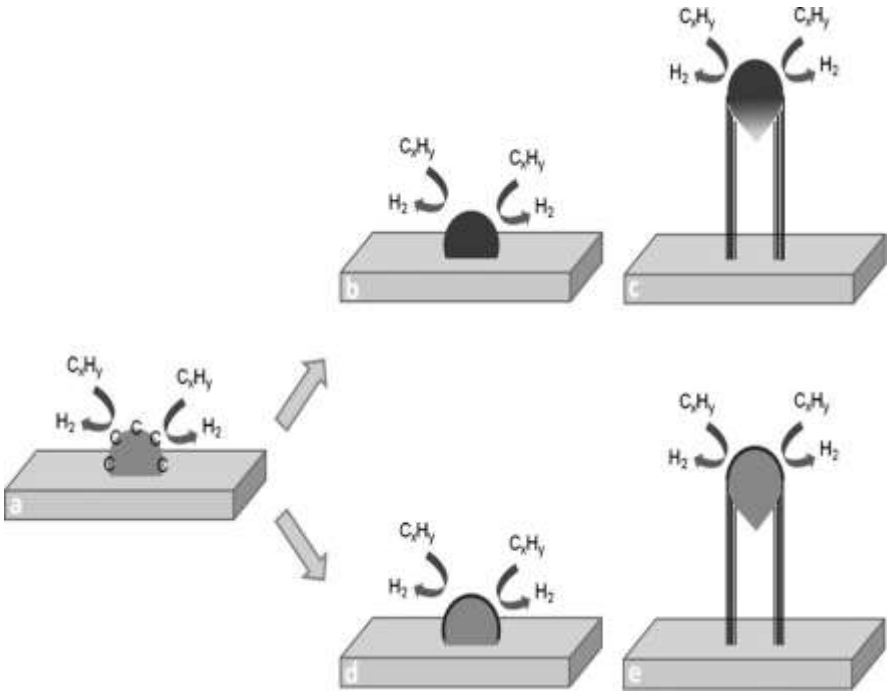


Figure 2. 13: Moving from VLS (a, b and c) to a VSS (a, d and e) mechanism where surface chemistry of the nanoparticle plays an important role **[1]**.

2.2.3 Proposed mechanism for low temperature (≤ 450 ℃) growth of carbon nanofibers

Copper is the most common catalyst that has been used to grow carbon nanomaterials at low temperatures and thus it is not surprising that the growth mechanism for carbon nanofibers at low temperatures have been modelled on a copper catalyst. Since Cu and other noble metals do not dissolve carbon **[18]** their growth mechanism have been modelled based on the surface interaction of the precursor carbon and the catalyst particle. Jian et al. **[14, 16]** studied the chemisorption of acetylene on the low index Cu planes (111), (110), (100) using DFT calculations (Figure 2.14). It was observed that adsorbates have different preferences towards the exposed planes. The

acetylene is observed to bond more favourably with the (111) and (110) plane based on the calculated Cu-C lengths and adsorption energies.

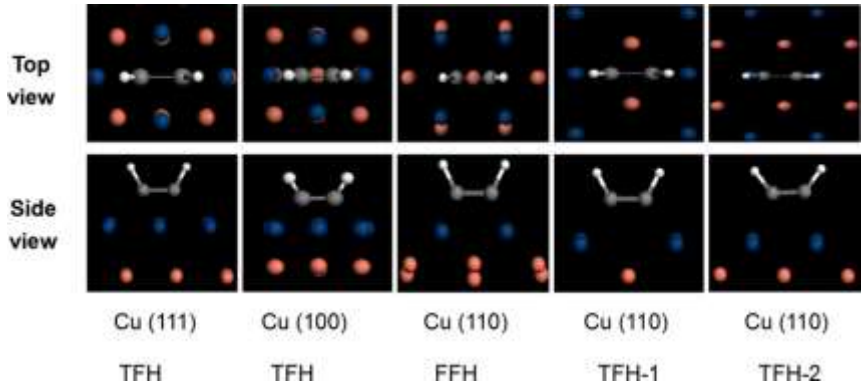


Figure 2.14: Energetically favorable adsorption sites for acetylene on Cu catalyst **[17].**

The growth of the carbon nanofibers on these planes is suggested to follow a decomposition polymerization process in which the acetylene molecules partially decompose and couple simultaneously on the surface of the metal nanoparticle. This mechanism therefore implies that the growth of carbon nanomaterials at low temperatures does not result in the full decomposition of the carbon precursor to C and H units. This is consistent with experimental studies since the grown carbon nanofibers are amorphous with a high content of hydrogen atoms (Figure 2.15).

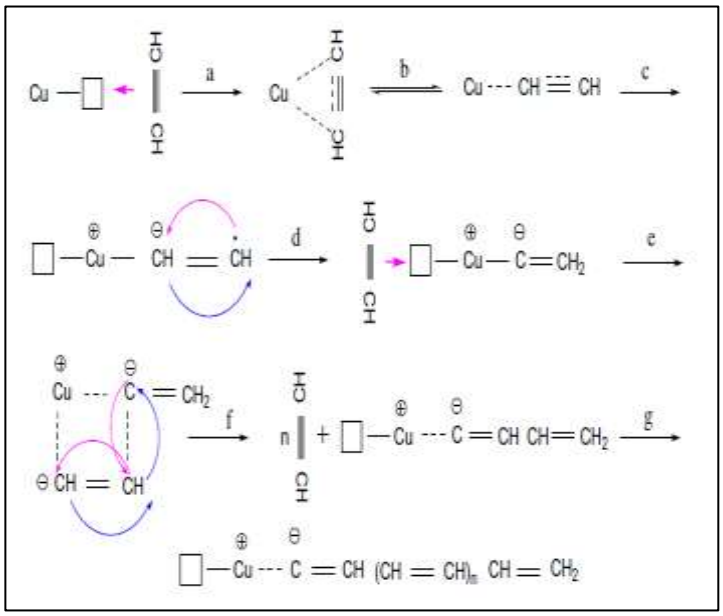


Figure 2. 15: Flow showing the polymerization of acetylene on Cu catalyst **[17]**

2.2.4 Proposed growth mechanism for high temperature (> 450 ℃) growth of carbon nanofibers

Growth of the carbon nanomaterials at high temperatures has been modelled on the complete decomposition of the carbon precursor on the catalyst templates. It is at high temperatures that the surface diffusion of the carbon units (sp^2/sp hybridized C_2 and C units) on the catalyst is observed to be highly activated as compared to bulk diffusion **[10, 19]**. Vinciguerra et al. **[20]** presented a growth model of carbon nanofibrils which suggests that the growth happens in the presence of two opposing forces. These are (1) a viscous force, from the hot gas, and (2) an extrusive force that causes the growth. This model states the importance of the carbon fragments and catalyst particle interface interaction. It is observed that bulk diffusion in the metal nanoparticle is not required for growth and the C_2 carbon fragment are the ones that are energetically favored for chemisorption on the metal NPs because they have the correct π orbitals for overlap with the orbitals of 3d symmetry (Figure 2.16).

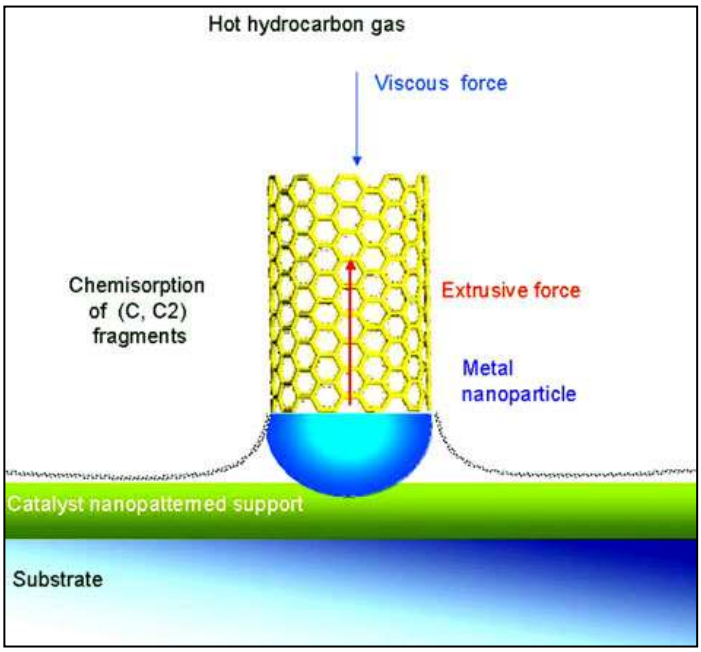


Figure 2. 16: Sketch showing the growth process (displaying both the extrusive and viscous force) **[21]**.

The kinetic model for the growth of the carbon nanomaterials on Cu a catalyst is described as follows **[21]**:

1. Adsorption of carbon precursor is followed by dissociation of the carbon source to carbon units and the liberation of hydrogen gas:

C_xH_y gas $\leftrightarrow$ $C_xH_y$ads, $C_xH_y$ads $\leftrightarrow$ xCads +yH_2 1

Lin et al **[21]** proposed that this reaction has two rate constants

$R_1 = k_1[C_XH_y]$ 2

$R_{-1} = k_{-1}[Cads]^X[H_2]^Y$ 3

2. The adsorbed carbon is then assembled to form the carbon nanomaterial by surface diffusion on the metal nanoparticle (equation 4). This process is proposed to be a rate determining step.

$C_{ads} \rightarrow C_{CNT/CNF}$ 4

$R_{CNT/CNF} = k_2 [C_{ads}]$ - Rate determining step

It is therefore suggested that the growth rate of the carbon nanomaterials is proportional to the amount of adsorbed carbon on the catalyst nanoparticle surface, thus making the VSS mechanism plausible since Cu has very low solubility for carbon and the surface kinetics yields the most favored reaction pathway.

2.2.5 References

1. Tessonnier JP, Su DS: **Recent progress on the growth mechanism of carbon nanotubes: a review**. *ChemSusChem* 2011, **4**(7):824-847.
2. Shaikjee A, Coville NJ: **The role of the hydrocarbon source on the growth of carbon materials**. *Carbon* 2012.
3. Wagner R, Ellis W: **Vapor-liquid-solid mechanism of single crystal growth**. *Applied Physics Letters* 1964, **4**(5):89-90.
4. Baker RTK, Barber MA, Harris PS, Feates FS, Waite RJ: **Nucleation and growth of carbon deposits from the nickel catalyzed decomposition of acetylene**. *Journal of Catalysis* 1972, **26**(1):51-62.
5. Baker RTK, Harris PS, Thomas RB, Waite RJ: **Formation of filamentous carbon from iron, cobalt and chromium catalyzed decomposition of acetylene**. *Journal of Catalysis* 1973, **30**(1):86-95.
6. Hofmann S, Csanyi G, Ferrari A, Payne M, Robertson J: **Surface diffusion: the low activation energy path for nanotube growth**. *Physical review letters* 2005, **95**(3):036101.
7. Tibbetts G, Devour M, Rodda E: **An adsorption-diffusion isotherm and its application to the growth of carbon filaments on iron catalyst particles**. *Carbon* 1987, **25**(3):367-375.
8. Hofmann S, Sharma R, Ducati C, Du G, Mattevi C, Cepek C, Cantoro M, Pisana S, Parvez A, Cervantes-Sodi F: **In situ observations of catalyst**

dynamics during surface-bound carbon nanotube nucleation. *Nano letters* 2007, **7**(3):602-608.

9. Hofmann S, Blume R, Wirth CT, Cantoro M, Sharma R, Ducati C, Hävecker M, Zafeiratos S, Schnoerch P, Oestereich A: **State of transition metal catalysts during carbon nanotube growth**. *The Journal of Physical Chemistry C* 2009, **113**(5):1648-1656.
10. Helveg S, Lopez-Cartes C, Sehested J, Hansen PL, Clausen BS, Rostrup-Nielsen JR, Abild-Pedersen F, Nørskov JK: **Atomic-scale imaging of carbon nanofibre growth**. *Nature* 2004, **427**(6973):426-429.
11. Robertson J: **Heterogeneous catalysis model of growth mechanisms of carbon nanotubes, graphene and silicon nanowires**. *J Mater Chem* 2012, **22**(37):19858-19862.
12. Podyacheva OY, Shmakov A, Ismagilov Z: **In situ X-ray diffraction study of the growth of nitrogen-doped carbon nanofibers by the decomposition of ethylene-ammonia mixtures on a Ni-Cu catalyst**. *Carbon* 2012.
13. Bhoware S, Maubane MS, Phaahlamohlaka T, Shaikjee A, Coville NJ: **Cu grown carbon nanofibers–variation of their chemical and physical properties**. *Chemical Physics Letters* 2013.
14. Jian X, Jiang M, Zhou Z, Zeng Q, Lu J, Wang D, Zhu J, Gou J, Wang Y, Hui D *et al*: **Gas-Induced Formation of Cu Nanoparticle as Catalyst for High-Purity Straight and Helical Carbon Nanofibers**. *ACS Nano* 2012, **6**(10):8611-8619.
15. Shaikjee A, Coville NJ: **Catalyst restructuring studies: The facile synthesis of tripod-like carbon fibers by the decomposition of trichloroethylene**. *Materials Letters* 2012, **68**:273-276.
16. Jian X, Jiang M, Zhou Z, Yang M, Lu J, Hu S, Wang Y, Hui D: **Preparation of high purity helical carbon nanofibers by the catalytic decomposition of acetylene and their growth mechanism**. *Carbon* 2010, **48**(15):4535-4541.

17. Shaikjee A, Franklyn PJ, Coville NJ: **The use of transmission electron microscopy tomography to correlate copper catalyst particle morphology with carbon fiber morphology**. *Carbon* 2011, **49**(9):2950-2959.
18. Ayre GN, Uchino T, Mazumder B, Hector AL, Hutchison JL, Smith DC, Ashburn P, Groot CHd: **On the mechanism of carbon nanotube formation: the role of the catalyst**. *Journal of Physics: Condensed Matter* 2011, **23**(39):394201.
19. Yazyev OV, Pasquarello A: **Effect of Metal Elements in Catalytic Growth of Carbon Nanotubes**. *Physical Review Letters* 2008, **100**(15):156102.
20. Vinciguerra V, Buonocore F, Panzera G, Occhipinti L: **Growth mechanisms in chemical vapour deposited carbon nanotubes**. *Nanotechnology* 2003, **14**(6):655.
21. Lin J-H, Zeng Z-Y, Lai Y-T, Chen C-S: **Low-temperature growth of bamboo-like multi-walled carbon nanotubes over an atomic layer epitaxy-Cu/SiO2 catalyst via metal-support interaction**. *RSC Advances* 2013, **3**(6):1808-1817.

2.3 Overview of Fischer-Tropsch Synthesis (FTS)

2.3.1 FTS history

The discovery of carbon monoxide hydrogenation to form methane in 1902 by Sabatier and Senderens over a transition metal catalyst laid the groundwork for the first chemistry involved in an XTL (X= coal, gas, biomass, T= to, L= liquid) technology **[1]**. Fischer-Tropsch (FT) synthesis (as practised today) is known to have started in Germany in 1913 when the German company BASF (Badishe Anilin und Soda Fabrik) obtained patents on the cobalt catalyzed preparation of hydrocarbons from synthesis gas (H_2/CO) **[2, 3]**. In 1923, at the Kaiser Wilhelm Institute, Franz Fischer and Hans Tropsch developed a method for carbon monoxide hydrogenation by reacting syngas over an iron or cobalt catalyst to yield a wide spectrum of hydrocarbon products (e.g petrol, diesel and heavy oils, etc.) **[4, 5]**.

By the 1920s petroleum had become essential to the economies of industrialized nations. The mass production of automobiles, the introduction of airplanes and petroleum-powered ships, and the recognition of petroleum's high energy content compared to wood and coal, required a shift from solid to liquid fuels as a major energy source **[6]**.

The work done by Fischer and Tropsch enabled IG Farben, Ruhrchemie, and other German chemical companies to develop a technologically-successful synthetic fuel industry that grew from a single commercial-size coal liquefaction plant in 1927 to twelve coal liquefaction and nine F-T commercial-size plants that in 1944 reached a highest production of 23 million barrels of synthetic fuel **[6, 7]**.

Because of World War 2 the Fischer-Tropsch process moved from the laboratory into full scale multiple plant operations, and this led to new production technologies and formation of a better performing catalyst. After the was a commercial scale Fischer-Tropsch plant built in Brownsville, Texas between 1945-1950. This plant utilized fluidized bed reactors. In 1951 South Africa began construction on South Africa's

first coal to synthetic fuels plant using F-T technology under the company name Sasol. By 1955 Sasol was marketing petrol as well as a full range of specialty chemicals using the FT technology **[8, 9]**.

In the early 1950's the discovery of large oil reserves in the Middle East led to a slow growth of the F-T technology **[9]**. The oil embargo by OPEC (organization of oil producing countries) in the late 1970s led to renewed interest on the Fischer-Tropsch and other alternative fuels. It led to intensive research and development programs in the Fischer-Tropsch process **[10]**. At this point many oil companies invested in research and development in Fischer-Tropsch synthetic fuel technology. The companies included Mobil, Texaco, Statoil, Sasol etc. Worldwide environmental legislation requiring ultra-low sulphur and aromatic levels in fuel will cost billions in oil refinery upgrading. The FTS offers a better and a cheaper technology in the synthesis of low sulphur and aromatic free fuels which is in line with environmental legislations in many countries. These have increased a number of FTS projects; some completed or under construction **[11, 12]**.

2.3.2 Fischer Tropsch synthesis and chemistry

Fischer Tropsch Synthesis is defined to be the surface-catalyzed polymerization process that uses CH_x monomers, formed by hydrogenation of adsorbed CO, in order to produce hydrocarbons products with varying chain length and functionality **[13]**. In the FTS reaction small starting materials (H_2 and CO) are used to synthesize larger molecular weight hydrocarbons: this has prompted many researchers to deduce that the reaction follows a polymerization mechanism. All the proposed Fischer Tropsch synthesis mechanism assumes a step by step polymerization process for the growth of the hydrocarbons. Even though there has been a great effort in studying FTS for the past 80 years its mechanism is not yet established **[14-16]**. The FT reaction is summarized by the equation: $2H_2 + CO \rightarrow -(CH_2)- + H_2O$. The FT product distribution is modelled using the Anderson-Schulz- Flory distribution (ASF). Using the following equation:

$$W/n = (1-\alpha)^2 \times \alpha^{n-1}$$

where, W_n = weight fraction of hydrocarbon comprising n carbon atoms,α = chain length growth probability and n = number of carbon atoms in the hydrocarbon **[17]**

2.3.3 Fischer-Tropsch synthesis mechanism

Several FTS mechanisms have been proposed based on the product distribution observed during the synthesis process. The actual FTS mechanism is not conclusive and several mechanism have been proposed for this process. The plausible mechanisms that have been proposed include the vinyl/alkenyl, the CO insertion, the oxygenate (enol) and the carbide (alkyl) mechanism **[15, 18, 19]**.

vinyl/alkenyl mechanism

This mechanism describe coupling of surface methyne and methylene monomers forming vinyl (-CH=CH2) groups which serve as the chain initiators on the active phase surface. The vinyl and the alkyl mechanism are a nearly similar because they both describe and can be used to explain synthesis of branched hydrocarbons. **[20, 21]**.

The oxygenate mechanism

The enol mechanism involves the chemisorption of carbon monoxide resulting in a reaction with the adsorbed hydrogen forming forming enolic surface monomers [30-31]. The chain propagation is suggested to occur via condensation. Chain termination can either form α-olefins or oxygenated products. Hydrogenation of α-olefins yields n-paraffins. termination occurring by hydrogenation. **[15, 22]**.

The CO insertion mechanism

In this growth mechanism emphasis is placed on the chemisorbed carbon monoxide as the building block. The chain propagation occurs via insertion of carbon monoxide

between a metal alkyl bond, followed by hydrogenation to form the products (oxygenates or alkenes), methylene groups are also involved in the chain propagation step **[15, 23]**.

Carbide mechanism

Carbon monoxide and Hydrogen are adsorbed dissociatively on the active metal surface, forming metal carbide which is hydrogenated by the dissociated hydrogen resulting in the formation of carbene and other alkyl groups. The hydrogen splits the carbon monoxide double bond forming aldehyde groups bonded to the metal surface, chain growth then follows by condensation and hydrogenation. **[15, 24]**.

2.3.4 Fischer-Tropsch Synthesis catalysts

Catalysts are very important components in the Fischer Tropsch process because the syngas has to be adsorbed on the catalytic surface for any polymerization process to take place. In the FTS the most commonly used catalysts are the group 8-10 metals of the Periodic Table as they are able to effectively adsorb CO and H_2 dissociatively **[7]**. All these metals exhibit varying Fischer Tropsch activity, the order in which the activity decreases as reported is as follows Ru > Fe > Co > Ni > Rh > Pd > Pt > Ir. Metals that are known to have economic Fischer Tropsch activity are Ru, Fe and Co **[25]**.

2.3.5 Supports for Fischer Tropsch Synthesis

Almost all industrial heterogeneous catalysts are based on metal particles being dispersed on a support. The support allows dispersion and stabilization of small metallic particles. Catalyst supports enhance the reducibility of the active metal and also enhance the attrition resistance of the metal particle **[26]**. Many catalyst supports have been studied and utilized for the FTS and include Al_2O_3, SiO_2, TiO_2, MgO and carbon materials **[27, 28]**, Mesoporous materials have also been investigated for FTS. Support properties of importance are: inertness; stability under reaction conditions; adequate mechanical strength, high surface area and porosity **[29]**. The effects on the

Fischer Tropsch activity of the active metals has been studied for different supports and the differences in the activity of the catalyst observed for each support has been attributed to differences in the degree of metal-support interaction which results in changes in reducibility and also pore diffusion and blocking effects **[30]**.

2.3.6 Carbon nanofibers as supports in Fischer Tropsch Synthesis

The use of carbon and carbon nanostructures as catalyst supports for the Fischer Tropsch synthesis has been extensively reported in literature ranging from the studies made on activated carbon **[31]**, carbon nanospheres **[32]** to carbon nanotubes and carbon nanofibers **[33, 34]**. Like carbon nanotubes, carbon nanofibers have high mechanical strength with a high degree of graphitic carbon and are very suitable for use as supports in heterogeneous catalysis **[35]**. Carbon nanofiber supported heterogeneous catalysts outperform activated carbon with regard to reproducibility, filterability and stability under oxidizing and reducing conditions **[35]**.The metal support interaction between the catalysts and the carbon nanofiber support is low as compared to the FTS catalysts supported on oxidic supports. Metals form mixed compounds with oxidic supports which are only reducible at high temperature **[36, 37]**. Work done by Bezemer et al. **[38]** has shown that CNF support materials combined with the high-pH deposition-precipitation technique hold considerable potential for cobalt-based Fischer–Tropsch catalysis as compared to use of a silica support, whereby silica reacts with Co to give cobalt hydrosilicates which require a reduction temperature of about 600 ℃, resulting in low cobalt dispersion caused by the agglomeration of the metal active sites **[38]**.

2.3.7 References

1. Sabatier P, Senderens JB: **New synthesis of methane**. *C R Acad Sci Paris* 1902, **134**:514-516.
2. BASF: **German Patent 293**. In. Germany; 1913: 787.

3. King DL, de Klerk A: **Overview of Feed-to-Liquid (XTL) Conversion**. In: *Synthetic Liquids Production and Refining*. vol. 1084: American Chemical Society; 2011: 1-24.
4. Fischer F, Tropsch H: **German Patent 484**. In. Germany; 1925: 337.
5. Fischer F, Tropsch H: *Brennst Chem* 1923, **4**:276.
6. Stranges AN: **A history of the fischer-tropsch synthesis in Germany 1926–45**. *Studies in surface science and catalysis* 2007, **163**:1-27.
7. Anderson RB, Kölbel H, Rálek M: **The Fischer-Tropsch Synthesis**, vol. 16: Academic Press New York; 1984.
8. Schulz H: **Short history and present trends of Fischer–Tropsch synthesis**. *Applied Catalysis A: General* 1999, **186**(1–2):3-12.
9. Dry ME: **The Fischer–Tropsch process: 1950–2000**. *Catalysis Today* 2002, **71**(3–4):227-241.
10. **Historical Development of Cobalt-slurry Fischer-Tropsch Reactor Systems** [http://www.fischer-tropsch.org/primary_documents/presentations/Co_Slurry_FT_Dev/Co_Slurry_FT_Dev_ref.htm]
11. Babich IV, Moulijn JA: **Science and technology of novel processes for deep desulfurization of oil refinery streams: a review☆**. *Fuel* 2003, **82**(6):607-631.
12. Pawelec B, Navarro RM, Campos-Martin JM, Fierro JLG: **Retracted article: Towards near zero-sulfur liquid fuels: a perspective review**. *Catalysis Science & Technology* 2011, **1**(1):23-42.
13. Iglesia E: **Design, synthesis, and use of cobalt-based Fischer-Tropsch synthesis catalysts**. *Applied Catalysis A: General* 1997, **161**(1–2):59-78.
14. Gaube J, Klein HF: **Studies on the reaction mechanism of the Fischer–Tropsch synthesis on iron and cobalt**. *Journal of Molecular Catalysis A: Chemical* 2008, **283**(1–2):60-68.
15. Davis BH: **Fischer–Tropsch synthesis: current mechanism and futuristic needs**. *Fuel Processing Technology* 2001, **71**(1–3):157-166.

16. Blekkan EAB, Ø.; Frøseth, V.; Holmen, A. : **Royal Society of Chemistry**. *Catalysis* 2007, **20**.
17. Bartholomew C: **Recent technological developments in Fischer-Tropsch catalysis**. *Catal Lett* 1990, **7**(1-4):303-315.
18. Traa Y: **Is a renaissance of coal imminent?—challenges for catalysis**. *Chemical Communications* 2010, **46**(13):2175-2187.
19. Davis BH: **Fischer–Tropsch Synthesis: Reaction mechanisms for iron catalysts**. *Catalysis Today* 2009, **141**(1–2):25-33.
20. Long HC, Turner ML, Fornasiero P, Kašpar J, Graziani M, Maitlis PM: **Vinylic Initiation of the Fischer–Tropsch Reaction over Ruthenium on Silica Catalysts**. *Journal of Catalysis* 1997, **167**(1):172-179.
21. Schulz H, Erich E, Gorre H, Steen E: **Regularities of selectivity as a key for discriminating FT-surface reactions and formation of the dynamic system**. *Catal Lett* 1990, **7**(1-4):157-167.
22. Linganiso LZ: **Microwave induced solid-state interactions for the synthesis of Fischer-Tropsch catalysts**. faculty of Science, University of the Witwatersrand; 2008.
23. Hindermann J, Hutchings G, Kiennemann A: **Mechanistic aspects of the formation of hydrocarbons and alcohols from CO hydrogenation**. *Catalysis Reviews—Science and Engineering* 1993, **35**(1):1-127.
24. Chen H, Adesina AA: **Kinetic modelling of methanation reaction over a Co□Mo/SiO2 catalyst**. *Journal of Chemical Technology & Biotechnology* 1994, **60**(1):103-113.
25. Vannice MA: **The catalytic synthesis of hydrocarbons from H2CO mixtures over the group VIII metals: I. The specific activities and product distributions of supported metals**. *Journal of Catalysis* 1975, **37**(3):449-461.
26. Jacobs G, Das TK, Zhang Y, Li J, Racoillet G, Davis BH: **Fischer–Tropsch synthesis: support, loading, and promoter effects on the reducibility of cobalt catalysts**. *Applied Catalysis A: General* 2002, **233**(1–2):263-281.

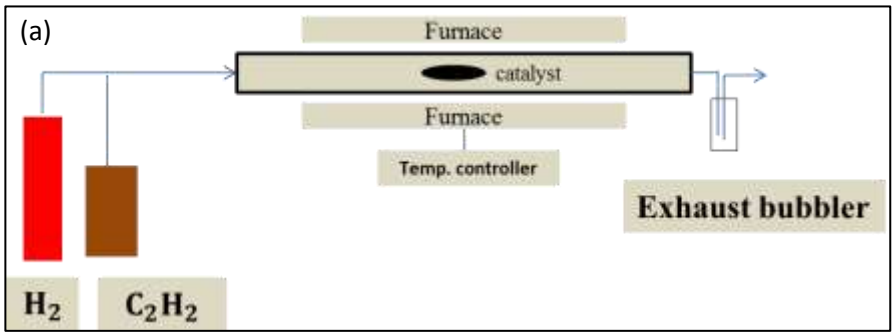
27. Storsæter S, Tøtdal B, Walmsley JC, Tanem BS, Holmen A: **Characterization of alumina-, silica-, and titania-supported cobalt Fischer–Tropsch catalysts**. *Journal of Catalysis* 2005, **236**(1):139-152.
28. Iglesia E, Soled SL, Fiato RA: **Fischer-Tropsch synthesis on cobalt and ruthenium. Metal dispersion and support effects on reaction rate and selectivity**. *Journal of Catalysis* 1992, **137**(1):212-224.
29. Martínez An, López C, Márquez F, Díaz I: **Fischer–Tropsch synthesis of hydrocarbons over mesoporous Co/SBA-15 catalysts: the influence of metal loading, cobalt precursor, and promoters**. *Journal of Catalysis* 2003, **220**(2):486-499.
30. Bessell S: **Support effects in cobalt-based fischer-tropsch catalysis**. *Applied Catalysis A: General* 1993, **96**(2):253-268.
31. Zaman M, Khodadi A, Mortazavi Y: **Fischer–Tropsch synthesis over cobalt dispersed on carbon nanotubes-based supports and activated carbon**. *Fuel Processing Technology* 2009, **90**(10):1214-1219.
32. Moyo M, Motchelaho MAM, Xiong H, Jewell LL, Coville NJ: **Promotion of Co/carbon sphere Fischer–Tropsch catalysts by residual K and Mn from carbon oxidation by KMnO4**. *Applied Catalysis A: General* 2012, **413–414**(0):223-229.
33. Trépanier M, Tavasoli A, Dalai AK, Abatzoglou N: **Fischer–Tropsch synthesis over carbon nanotubes supported cobalt catalysts in a fixed bed reactor: Influence of acid treatment**. *Fuel Processing Technology* 2009, **90**(3):367-374.
34. Motchelaho MAM, Xiong H, Moyo M, Jewell LL, Coville NJ: **Effect of acid treatment on the surface of multiwalled carbon nanotubes prepared from Fe–Co supported on CaCO3: Correlation with Fischer–Tropsch catalyst activity**. *Journal of Molecular Catalysis A: Chemical* 2011, **335**(1–2):189-198.
35. Serp P, Corrias M, Kalck P: **Carbon nanotubes and nanofibers in catalysis**. *Applied Catalysis A: General* 2003, **253**(2):337-358.

36. Xiong H, Motchelaho MAM, Moyo M, Jewell LL, Coville NJ: **Correlating the preparation and performance of cobalt catalysts supported on carbon nanotubes and carbon spheres in the Fischer–Tropsch synthesis**. *Journal of Catalysis* 2011, **278**(1):26-40.
37. Keyser MM, Prinsloo FF: **Loading of cobalt on carbon nanofibers**. *Studies in surface science and catalysis* 2007, **163**:45-73.
38. Bezemer GL, Radstake PB, Koot V, van Dillen AJ, Geus JW, de Jong KP: **Preparation of Fischer–Tropsch cobalt catalysts supported on carbon nanofibers and silica using homogeneous deposition-precipitation**. *Journal of Catalysis* 2006, **237**(2):291-302.

Chapter 3: Experimental and characterization procedure for carbon synthesis and the Fischer-Tropsch process.

3.1 Method for synthesizing carbon nanofibers (CNFs)

The methods of synthesizing carbon nanostructures include catalytic chemical vapor deposition (CCVD) **[1]**, arc discharge **[2, 3]** catalytic plasma enhanced chemical-vapor deposition (C-PECVD) **[4]**, and laser vaporization **[5]**. Only CCVD allows controlled synthesis of carbon nanotubes and nanofibers while C-PECVD allows synthesis in which the location, alignment, size, shape, and structure of each individual nanofiber can be controlled during synthesis **[6, 7]**. The reactions are normally done in horizontal reactors which are the most common configurations for the production of carbon nanofibers. The reactor consists of a heated quartz tube through which gases are passed using appropriate gas carriers. Vertical furnace configurations have also been used where the carbon source is injected either at the top or bottom of the quartz tube **[8]**. The synthetic reaction is commonly achieved in the presence of catalysts. Either a supported or unsupported catalyst is used **[1, 9]** or the floating catalyst method is used which includes the use of volatile organometallic compounds as precursors (such as ferrocene) **[10]**. In this study a horizontal CVD set up (both single and double stage furnaces, Figure 3.1) was employed for the synthesis of the carbon nanofibers using different copper catalysts.



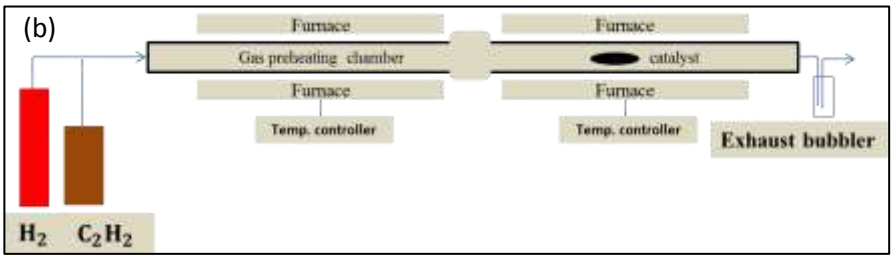


Figure 3. 1: Horizontal CVD set up, (a) single and (b) double stage furnace.

3.2 Experimental procedure for Fischer-Tropsch synthesis

The gas to liquid process employed in the Fischer-Tropsch synthesis is a very special process which requires special set parameters for the reaction to be feasible and to yield desired results. In this section the reaction conditions that were employed in the FT reaction together with the conversion and mass balance calculations that were used to obtain the product distribution of the reaction are discussed.

3.2.1 Gases

The synthesis gas used in the FT reaction was a gas mixture composed of 60% hydrogen, 30% carbon monoxide and 10% nitrogen gas, this was done to ensure that the H_2: CO ratio is always approximately 2:1 in the feed gas. N_2 is used as an internal standard since it is not reactive under the FT reactor conditions. The internal standard guarantees accurate mass balance calculations. Hydrogen gas (99.99%) was employed for the pre-reduction of the FT catalyst. The gases used in the FT synthesis were obtained from AFROX (African Oxygen) Ltd.

3.2.2 Catalytic reactor set-up

A stainless steel tube with and internal diameter of 16.00 mm was employed as the catalyst reactor for the FT reactions (Figure 3.2). The reactor is a fixed bed reactor with a frit inserted in the middle to serve as a support for the catalyst bed. Quartz wool is placed on the frit and the catalyst rests on the wool. After the catalyst powder (sieved by 150 µm sieve) is placed inside the reactor then reactor is the filled with

steel balls so as to serve as a heat conductor to allow homogenous heat distribution in the reactor and to pre-heat the syngas as it enters the reactor before it interacts with the catalyst bed. The tube reactor is then placed in a heating jacket which is long enough to keep a constant temperature profile across the reactor.

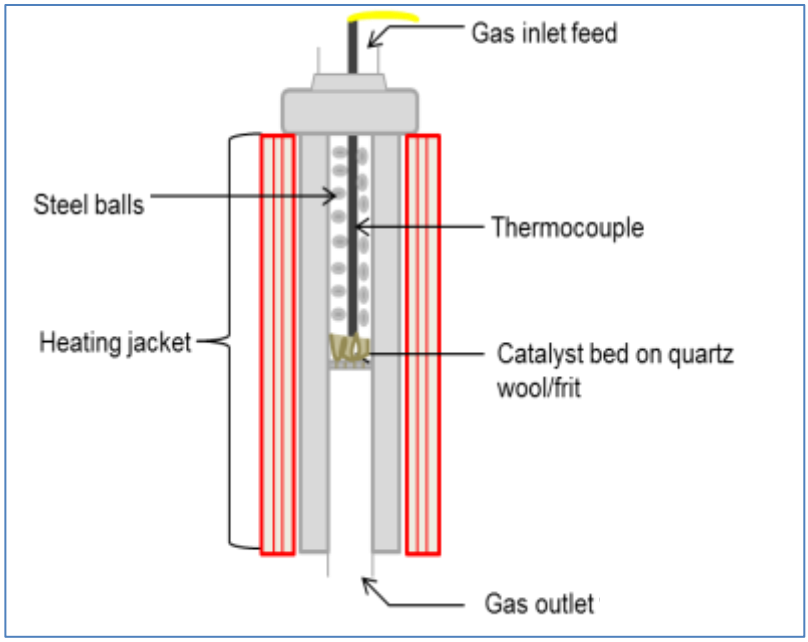


Figure 3. 2: Sketch of the fixed bed reactor employed in the FT reaction

The first knockout pot (KP) is placed directly below the catalyst reactor and maintained at 150℃, this knock pot is employed as a wax trap. A second knockout pot at room temperature is connected next to the wax trap. This KP serves as a cold trap and thus it is used to trap water and high molecular weight hydrocarbons (i.e. heavy oil). All the flow lines from the knockout pots to the online gas chromatogram were kept at 100 ℃ to avoid any potential condensation of some of the products that managed to pass through the knock out pots. The flow rate through the rig was controlled using a needle valve. The gas phase stream that was not condensed inside the two knockout pots was then analyzed on stream using the online two gas chromatographs equipped with thermal conductivity and flame ionization detectors respectively. Wax and liquid hydrocarbons collected inside the two traps (Figure 3.3)

were analyzed using an offline gas chromatograph equipped with a flame ionization detector. Detector details are shown in Table 3.1.

Table 3. 1: Specifications of the gas chromatographs employed

Online gas chromatograph	
Detector	Thermal conductivity detector (TCD)
Column type	Packed, stainless steel, 2m x 2.2mm, O.D = 1/8"
Stationary phase	Carboxen-1000, 60-80 mesh
Model type	PYE Unicam (Series 204)
Online gas chromatograph	
Detector	Flame ionization detector (FID)
Column type	Packed, stainless steel, 1.5 m x 2.2 mm, O.D = 1/8"
Stationary phase	Porapack q, 80/100 mesh
Model type	Hewlett Packard 5890
Offline gas chromatograph	
Detector	Flame ionization detector (FID)
Column type	30 m x 5 μFT, O.D.= 0.53 mm
Stationary phase	ZB-1
Model type	Varian 3700

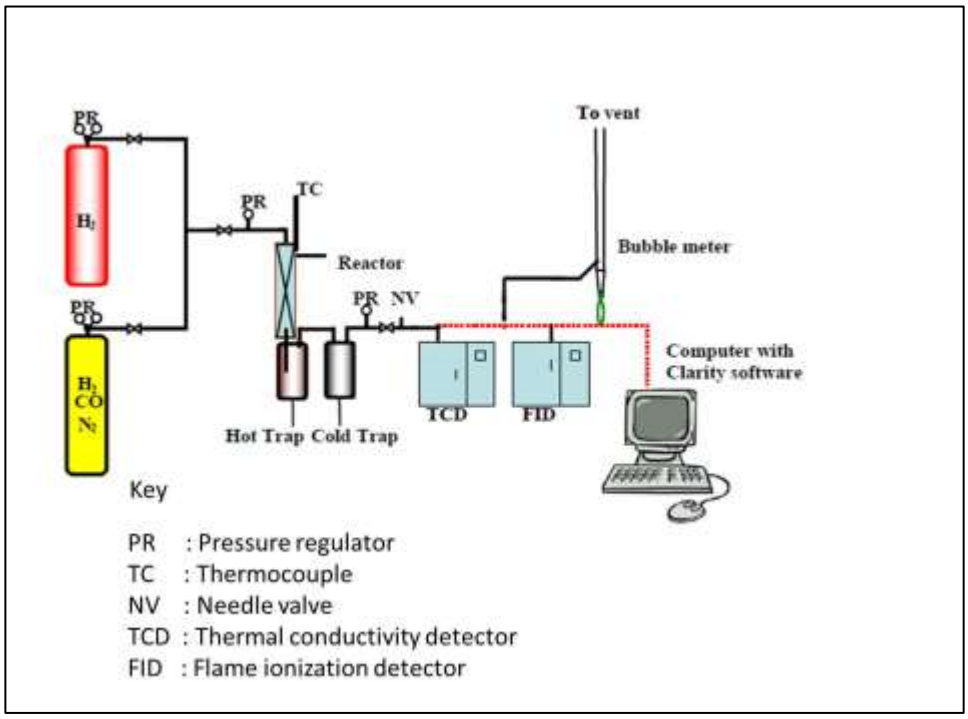


Figure 3. 3: Schematic representation of the reactor and rig setup

3.2.3 Measurements of the catalyst activity

The supported catalyst (~0.5 g) was added into the steel reactor. The catalyst is then reduced in-situ used UHP hydrogen. The reduction step was performed using: H_2 gas flow rate of 30 $mL.min^{-1}$. The temperature ramping of the heating jacket was achieved in a controlled manner to 350 ℃. The temperature was raised to 250 ℃ in a 2 hour interval and then further raised to 350 ℃ in 1 hour. After the temperature reached 350 ℃ it was then held constant for 16 hours at the set temperature to completely reduce the catalyst component (Co_3O_4 or CoO to Co). When the reduction process was completed the temperature was decreased to room temperature. This was followed by the FT synthesis step. In this process pressure inside the reactor is set at 8 bar by the gradual introduction of syngas (29.2% CO, 10.3% N_2 and hydrogen balance). The reactor was heated to the synthesis temperature of 220 ℃ by ramping up the temperature as follows. The heating jacket was heated to 200 ℃ in an hour in

the first step, in the second step the temperature was ramped to 220 ℃ in an hour to reach the desired synthesis temperature. The Fischer Tropsch synthesis was carried at steady state for 120 hours (i.e. 5 days) at 220 ℃. With the GSHV in the range of 1000-1200 $mL.h^{-1}.g_{cat}^{-1}$.

3.2.4 Analysis of products

The resulting products analysis was divided in two parts. The gaseous products were analyzed using the online gas chromatographs, while the heavy oil and wax were analyzed using the offline GC. The thermal conductivity detector was applied for analyzing CH_4, H_2, N_2 CO and CO_2, while the flame ionization detector was used for detection of the hydrocarbons (C_1 - C_x). Before the start of reaction and analysis of the products the online GCs were calibrated using a gas mixture with components of known concentrations. The gas mixture used contained CO (10%), CO_2 (5%), CH_4 (2.5%), C_2H_4 (0.2%) and C_2H_6 (0.5%) in an argon balance. Synthesis gas (29.2% CO, 10.3% N_2 and H_2 balance) was also applied as a calibrant to calculate the number of moles of the reactants entering the reactor via the gas inlet feed stream. Gas traces produced from the calibration gases were recorded and plotted using a DataApex Chromatograph software package known as Clarity (v. 2.5) (Figures (3.4-3.7)).

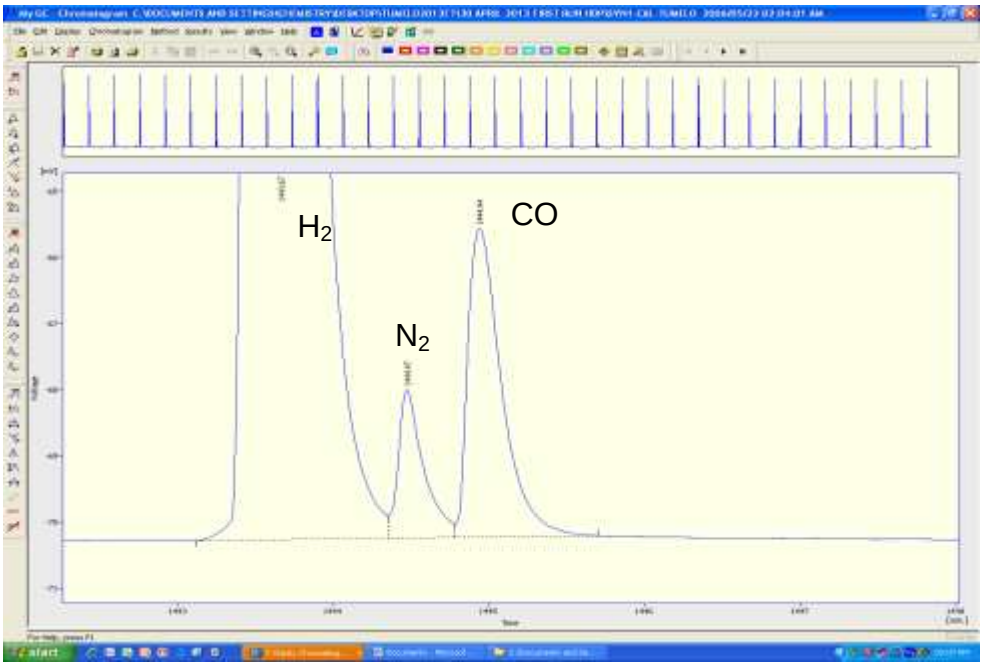


Figure 3. 4: TCD of syngas trace using argon as carrier gas.

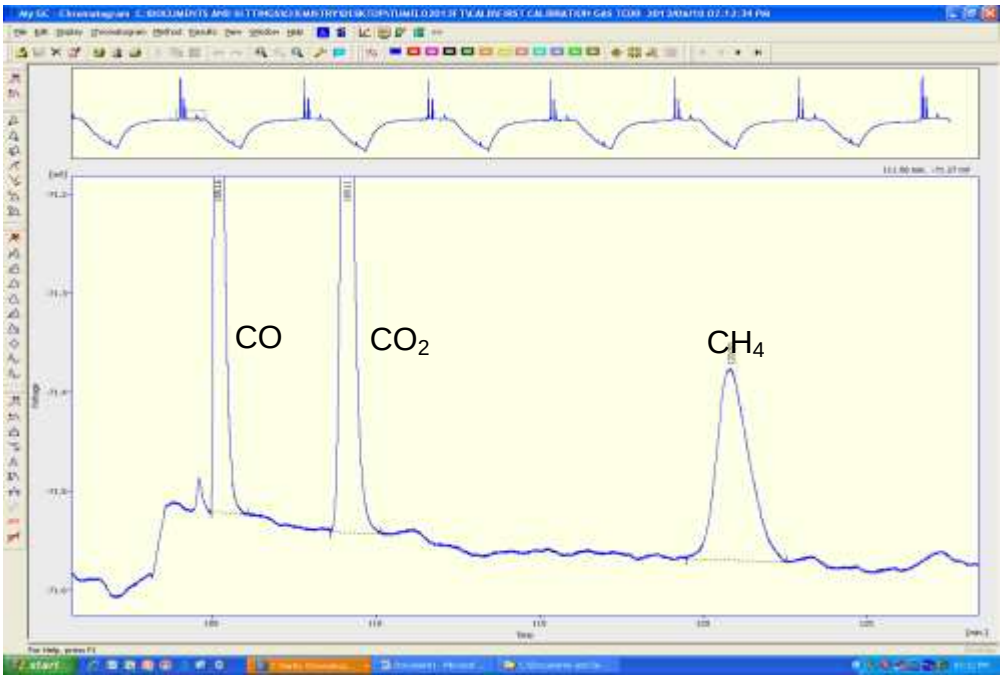


Figure 3. 5: TCD trace of calibration gas mixture using argon as carrier gas.

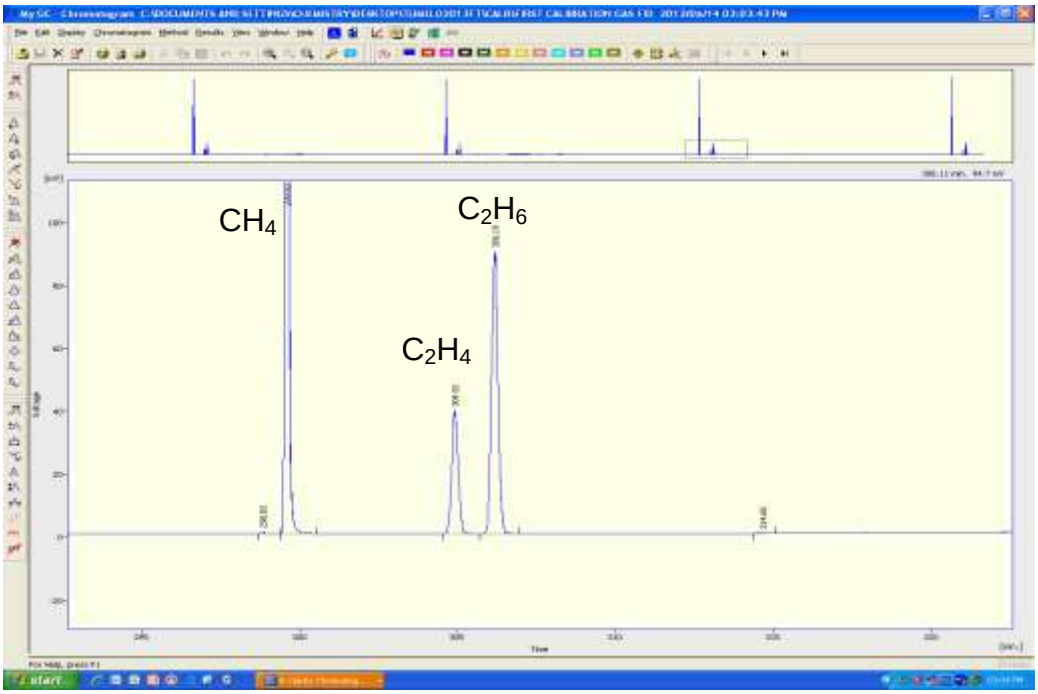


Figure 3. 6: FID trace of calibration gas mixture using nitrogen as carrier gas.

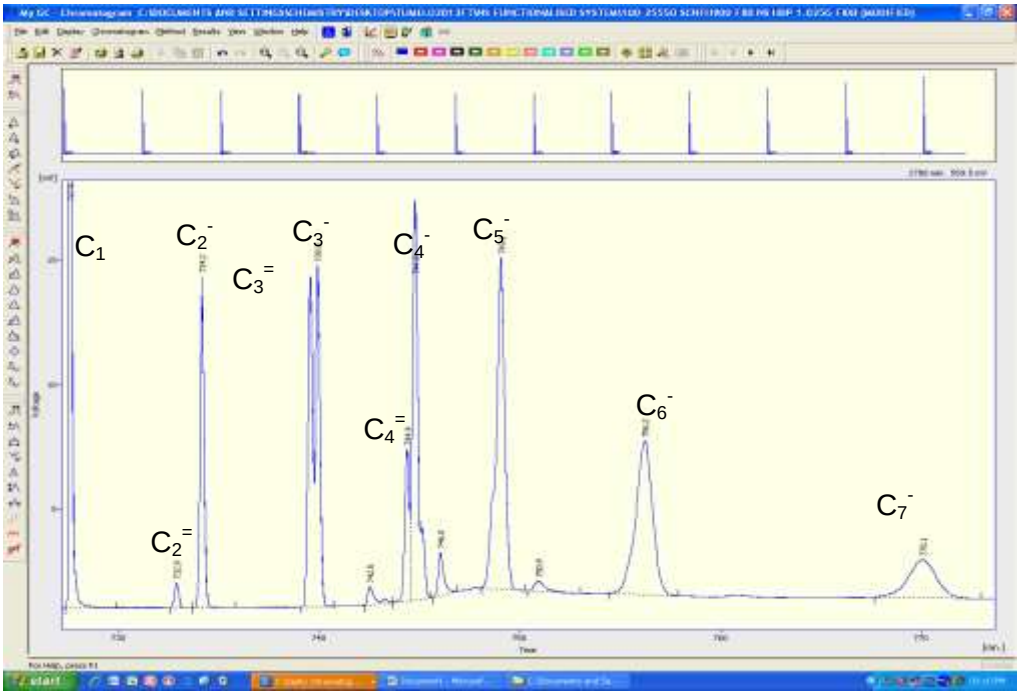


Figure 3. 7: FID trace of the gaseous product stream.

3.3 Mass balance and data analysis calculations

The mass balance calculations performed were similar to those performed by Motchelaho, Hexana, Bahome and Price **[11-14]**. The mass balance calculation was performed on the carbon content under steady state conditions for about 120 hours. The reaction reached steady state activity after about 20 hours. The products in the knockout pots were collected separately then weighed and analyzed using the offline GC. The analysis was performed by injecting 0.02 μL into the offline gas chromatograph.

3.3.1 Equations employed for mass balance calculations

The outlet gas flow rate (F_{out}) of the gas stream was measured everyday using a bubble meter. From this the calculation of the inlet gas flow (F_{in}) was determined. Since the total mass flow in and out of the reactor is equal, nitrogen as an internal standard was used as an inert tracer during the FT reaction. The total molar inlet gas flow was expressed in relation to the total molar outlet gas flow as follows:

$$F_{in} \times X_{N_2 in} = F_{out} \times X_{N_2 out} \quad \text{..... 1}$$

$$\text{Therefore } F_{in} = \frac{Fout \times X_{N_2 out}}{X_{N_2 in}} \quad \text{..... 2}$$

Where:

F_{in} = Total molar flow rate entering the reactor.

F_{out} = Total molar flow rate exiting the reactor (calculated at P = 1 bar and 298 K).

$N_2 in$ = Mole fraction of N_2 in the stream entering the reactor.

$N_2 out$ = Mole fraction of N_2 in the stream exiting the reactor.

To calculate the percentage conversion of CO the amount of CO in the outlet stream has to be first known.

The molar percentage of any component gas Φ in the outlet stream was calculated based on the peak areas of the component gases obtained using the Clarity software peak integration Clarity (v. 2.5) package.

Thus:

$$\% \Phi_{gas} = \left[\frac{A_{\Phi,gas}}{A_{\Phi,cal}}\right] \times \% \Phi_{cal} \quad \text{..... 3}$$

Where:

$\% \Phi_{gas}$ = Mol percentage of compound Φ in the sampled gas.

$\% \Phi_{cal}$ = Mol percentage of compound Φ in the calibration gas.

$A_{\Phi,gas}$ = Integrated area of compound Φ obtained from the GC peak using the Clarity software.

$A_{\Phi,cal}$ = Integrated area of compound Φ in the calibration gas obtained from the GC peak using Clarity software.To calculate the mol percentage of other compounds when the calibration data was not obtained from the calibration gas mixture, response factors relative to the calibration data of reference compounds present in the calibration gas were used. The response factors were obtained from molar response factors for hydrocarbon products references **[11, 12]** (Table 3.2).

Table 3. 2: Molar response factors for hydrocarbon products [**11, 14]**

Carbon number	Paraffin	Olefin
1	1.00	-
2	1.00	1.00
3	0.74	0.70
4	0.55	0.78
5	0.47	0.47
6	0.40	0.40
7	0.35	0.35
8	0.32	0.32
9	0.28	0.28
10	0.24	0.24
11	0.21	0.21
12	0.19	0.19
13	0.18	0.18
14	0.17	0.17
15	0.15	0.15

* High molecular weight hydrocarbons response factors were assumed to be 1.00

Therefore the mol percentages in the analyzed gas samples were calculated using the following equation:

$$\% \Phi_{gas} = \left[\frac{A_{\Phi,gas}}{A_{\theta,cal}}\right] \times \% \theta_{cal} \times RF_{\Phi,\theta} \quad \text{..... 4}$$

Where:

$RF_{\Phi,\theta}$ = Response factor of compound Φ relative to reference compound θ.

$\% \theta_{cal}$ = Integrated area of reference compound θ in the calibration gas obtained from the GC peak using Clarity software.

The percentage CO conversion was calculated using the following equation:

$$\%CO_{conversion} = \left[\frac{X_{CO_{in}} - X_{CO_{out}} \times \left(\frac{X_{N_2 in}}{X_{N_2 out}}\right)}{X_{CO_{in}}}\right] \times 100 \quad \text{..... 5}$$

Where:

$X_{CO_{in}}$ = Mol fraction of CO entering the reactor.

$X_{CO_{out}}$ = Mol fraction of CO exiting then reactor.

$\left(\frac{X_{N_2 in}}{X_{N_2 out}}\right)$ = contraction factor. 6

From equation (1) the molar flow rates of CO in and out of the reactor were calculated using these equations:

$$F_{CO,in} = F_{in} \times X_{COin} \quad \text{..... 7}$$

$$F_{CO,out} = F_{out} \times X_{COout} \quad \text{..... 8}$$

Where:

$F_{CO,in}$ = Molar flow rate of CO entering the reactor.

$F_{CO,out}$ = Molar flow rate of CO exiting the reactor.

The rate of CO conversion during the steady state period was computed using the following equation:

$$r_{CO} = \left[\frac{F_{CO,in} - F_{CO,out}}{m_{cat}}\right] \quad \text{..... 9}$$

r_{CO} = rate of CO conversion (mol.min^{-1}.g$_{catalyst}^{-1}$).

m_{cat} = mass of catalyst sample.

The rate of water gas shift reaction was experimentally calculated based on the rate of carbon dioxide formation ($r_{CO_2} = r_{WGS}$) and therefore the Fischer-Tropsch synthesis rate is obtained by the following equation: $r_{FTS} = r_{CO} - r_{WGS}$

The number of moles of carbon entering and exiting the reactor during the total mass balance period was calculated by using equation x and y:

$$N_{C,in} = F_{CO,in} \times t \quad \text{..... 10}$$

$$N_{C,out} = F_{CO,out} \times t + N_{C,gas} + N_{C,oil} + N_{C,wax} + N_{CO_2} \quad \text{..... 11}$$

$N_{C,in}$ = Total mol of C in the feed stream during the total mass balance period.

$N_{C,out}$ = Total mol of C in the outlet stream during the total mass balance period.

t= mass balance time

$N_{C,gas} + N_{C,oil} + N_{C,wax}$ = Total mol of C in the hydrocarbon products. .. 12

Therefore the mass balance percentage accepted with $\pm$5% error bar was calculated using the equation:

$$\%\ \text{carbon balance} = \left[\frac{N_{C,out}}{N_{C,in}}\right] \times 100 \quad \text{..... 13}$$

For the mass balance to be correct, N_C,in should be equal or approximately equal to $N_{C,\ out}$.

From the carbon balance calculations, the product selectivities of individual hydrocarbons (i.e. Φ_i) were calculated using the following equation:

$$\text{sel}\,(\Phi_i) = \left[\frac{nC_{\Phi_i}}{\sum nC_{\Phi_i}}\right] \times 100 \quad \text{..... 14}$$

nC_{Φ_i} = Total moles of carbon in compound Φ_i in the product stream.

sel (Φ_i) = selectivity of product Φ_i.

The olefin to paraffin ratio was calculated from equation 15:

$$\text{Olefin paraffin ratio}\,(\Phi_x) = \left[\frac{nC\Phi_x^{=}}{nC\Phi_x^{-}}\right] \quad \text{..... 15}$$

$nC\Phi_x^{=}$ = Number of carbon moles for the olefin containing x carbon atoms.

$nC\Phi_x^{-}$ = Number of carbon moles for a paraffin containing x carbon atom

3.4 Characterization techniques

Different techniques were used to characterize the materials to obtain the physical and chemical relationships, and to determine how they would affect their phsico-chemical properties for the application in the Fischer-Tropsch synthesis. The techniques employed in this study were chosen to probe the bulk and surface properties of the materials.

3.4.1 Transmission Electron Microscopy

A FEI Tecnai G^2 Spirit operating at 120 kV electron microscope was used to take TEM images. The sample was suspended in a methanol solvent and then a drop was added on to a copper grid, dried and analyzed.

3.4.2 Powder X-ray diffraction

The bulk composition of catalysts was analyzed using a Bruker D2 phaser equipped with a Lynxeye detector. The radiation used is the Co-Kα at 30 kV. The scan ranged from $5^0 \leq 2\theta \leq 100^0$ in 0.026^0 steps. The catalyst was ground to powder and sieved using 150 µm sieve and flatly packed on a sample holder before analysis.

3.4.3 Raman spectroscopy

Raman spectroscopy analysis was performed using a micro-Raman of a Jobin-Yvon T64000 Raman spectrometer. The spot size on the sample was approximately 1.5 µm in diameter and a wavelength of 514.5 nm from an argon ion laser watt, a charge coupled detector (CCD) was used.

3.4.4 Fourier Transform Infrared spectroscopy

A Brüker Tensor 27 Fourier Transform Infrared spectrometer was used to analyze the surface functionalities and the type of functional groups present on the carbon nanofibers. All the samples analysed were in powder form. The spectra were recorded in the range of 550-4000 cm^{-1}.

3.4.5 Brunauer-Emmet and Teller surface area measurement

A Micromeritics Tristar-Surface area and Porosity analyzer was used, to determine the surface areas of the materials. Sample with mass of ~0.2 g was degassed in nitrogen at 150 ℃ for 4 h prior to analysis using a Micromeritics flow Prep 060, sample degas system.

3.4.6 Temperature programmed reduction

A Micromeritics AutoChem II instrument was used for the determination of the degree of reduction and reducibility of the catalysts. The sample of ~90-100 mg was degassed at 150 ℃ for 30 minutes using a helium gas flowrate of 50 mL/min. TPR

analysis was performed using 5 % hydrogen gas in Argon (50 mL/min) at 1 bar pressure while the temperature was raised to 900 ℃ at a heating rate of 10 ℃/min.

3.4.7 Thermo-gravimetric analysis

A Perkin Elmer TGA 4000 Thermo-gravimetric analyzer was used for thermal analysis of all samples in air or nitrogen, at a constant heating rate of 10 ℃/min in the temperature range of 30 - 900 ℃. An approximate sample mass of 10 mg was used for the analysis with 20 mL/min flow rate of air.

3.5 References

1. Nitze F, Abou-Hamad E, Wågberg T: **Carbon nanotubes and helical carbon nanofibers grown by chemical vapour deposition on C60 fullerene supported Pd nanoparticles**. *Carbon* 2011, **49**(4):1101-1107.
2. Kajiura H, Huang H, Tsutsui S, Murakami Y, Miyakoshi M: **High-purity fibrous carbon deposit on the anode surface in hydrogen DC arc-discharge**. *Carbon* 2002, **40**(13):2423-2428.
3. Huang L, Wu B, Chen J, Xue Y, Liu Y, Kajiura H, Li Y: **Synthesis of single-walled carbon nanotubes by an arc-discharge method using selenium as a promoter**. *Carbon* 2011, **49**(14):4792-4800.
4. Wang H, Moore JJ: **Low temperature growth mechanisms of vertically aligned carbon nanofibers and nanotubes by radio frequency-plasma enhanced chemical vapor deposition**. *Carbon* 2012, **50**(3):1235-1242.
5. Kokai F, Nozaki I, Okada T, Koshio A, Kuzumaki T: **Efficient growth of multi-walled carbon nanotubes by continuous-wave laser vaporization of graphite containing B4C**. *Carbon* 2011, **49**(4):1173-1181.
6. Ghavanini FA, Lopez-Damian M, Rafieian D, Svensson K, Lundgren P, Enoksson P: **Controlling the initial phase of PECVD growth of vertically aligned carbon nanofibers on TiN**. *Sensors and Actuators A: Physical* 2011, **172**(1):347-358.

7. Choi YC, Shin YM, Lee YH, Lee BS, Park G-S, Choi WB, Lee NS, Kim JM: **Controlling the diameter, growth rate, and density of vertically aligned carbon nanotubes synthesized by microwave plasma-enhanced chemical vapor deposition**. *Applied physics letters* 2000, **76**(17):2367-2369.
8. Mondal K, Coville NJ: **Floating catalyst synthesis of carbon nanotubes**. *Encyclopedia of Nanoscience and Nanotechnology* 2011, **14**:161-203.
9. Shaikjee A, Coville NJ: **Catalyst restructuring studies: The facile synthesis of tripod-like carbon fibers by the decomposition of trichloroethylene**. *Materials Letters* 2012, **68**(0):273-276.
10. Mohlala MS, Liu X-Y, Witcomb MJ, Coville NJ: **Carbon nanotube synthesis using ferrocene and ferrocenyl sulfide. The effect of sulfur**. *Applied Organometallic Chemistry* 2007, **21**(4):275-280.
11. Motchelaho AMM: **Iron and cobalt catalysts supported on carbon nanotubes for use in the Fischer-Tropsch synthesis**. Faculty of Engineering and the Built Environment, University of the Witwatersrand; 2011.
12. Price JG: **An investigation into novel bimetallic catalysts for use in the Fischer-Tropsch reaction**. Johannesburg: Faculty of Science, University of the Witwatersrand; 1994.
13. Bahome MC: **Synthesis and use of carbon nanotubes as a support for the Fischer-Tropsch Synthesis**. Faculty of Engineering and the Built Environment, University of the Witwatersrand; 2008.
14. Hexana WM: **A systematic study of the effect of chemical promoters on the precipitated Fe-based Fischer-Tropsch Synthesis catalyst**. Faculty of Science, University of the Witwatersrand; 2009.

Chapter 4: Results and discussion: CNF synthesis and characterization.

4.1 Study and Characterization of Copper Oxide Nanoparticles

4.1.1 Introduction

Copper(II) oxide nanoparticles show properties that are very important for the advancement of nanoscience and nanotechnology, Copper oxide NPs are p-type semiconductors with a narrow energy band gap (~ 1.2-1.6 eV). The CuO nanoparticles have been used in applications such as sensors **[1]**, catalysts **[2]**, in antimicrobial activity **[3]**, solar cells **[4]** and as semiconducting materials **[5]**.

CuO nanoparticles have a monoclinic crystallographic phase and are more stable than Cu^{0} and Cu^{+1}(cuprite) nanoparticles because of its higher oxidation state of (II) which allows the nanoparticles to have a lower surface energy that are less prone to sintering and agglomeration **[6, 7]**.

It is well known that the chemical and physical properties of nanomaterials are greatly affected by their morphologies and physical constraints, and this is also true for CuO nanoparticles. Many methods for the synthesis of the nanoparticles have been devised to control the morphology of the CuO.

Different techniques such as thermal (UHV or high pressure) decomposition, laser ablation **[8-10]** and wet chemical procedures have been employed for the synthesis of morphologically different copper oxide nanoparticles **[11-13]**. The CuO particles are obtained in different sizes, ranges and shapes (mostly spherical). It has been shown that the smaller CuO particle favor growth of helical CNFs while large particles favor deposition of straight CNFs (more details in the literature review, section 2.1).

In this study two methods were used to produce copper oxide nanoparticles: (1) decomposition of a copper precursor in the presence of a capping agent and (2) use of

a precipitating agent such as potassium hydroxide as sodium hydroxide. SiO_2 spheres were used as supports for the copper nanoparticles that were produced. The different methods were employed in order to control the average size of CuO particles synthesized in the nanoscale regime and above the nanoscale regime.

4.1.2 Experimental

A variety of methods were used to make a range of CuO nanoparticles. The different methods were expected to produce CuO particles with different particle sizes and possibly different shapes.

Four catalyst systems where prepared for synthesizing carbon nanofibers

Preparation of CuO particles by precipitation. (CuOK, CuONPs)

(a) 1. 5 mmol of $Cu(NO_3)_2.3H_2O$ was dissolved in 100 ml deionized water, 10 mmol of KOH pellets were added these solution to serve as the precipitating agent. The solution was stirred overnight at room temperature to allow complete precipitation of $Cu(OH)_2$. The precipitate was then filtered and dried in an oven at 100 ℃ for 12 hours. The dry precipitate was then calcined at 500 ℃ for 3 hours. (**CuOK**)

(b) 10 mmol of $Cu(CH_3COO)_2.H_2O$ was dissolved in 500 ml ethanol solvent to which was added acetic acid (1.1 mL, 18 mmol). The solution was then heated to 78 ℃ and when the desired temperature was reached 40 mmol of NaOH was added to the solution which was then stirred for an hour. After the completion of the reaction the colloidal solution was then separated by centrifugation (3000 RPM, 1 hour) and washed with ethanol solvent to harvest the the CuO nanoparticles (**CuONPs).** These were then left to dry in air at ambient pressure and temperature.

Preparation of lauric acid capped CuO by thermal decomposition.

Synthesis of the copper oxide nanoparticles was carried out as follows. Copper acetate monohydrate (1 g) was mixed with lauric acid (n-dodecanoic acid which served as a capping agent*)* in a mol ratio of 8:1. The mixture was then dissolved in 20

mL ethanol followed by the evaporation of the ethanol using a rotary vapour. The resulting homogenous mixture was then subjected to thermal decomposition at 120 ℃ for 12 hours to form copper oxide nanoparticles which were then collected without any further treatment (**CuO@LA**).

Preparation of silica coated copper oxide using one pot synthesis (CuOK@SiO_2)

Copper oxide micro particles (0.2 g) synthesised in part a (CuOK particles) were dispersed in 100 mL ethanol (1g PVP, MW=10 k solution). The solution was stirred for 12 hours following the procedure used by Li et al **[14]**. To the solution was added 10 mL of 25% ammonia solution and the solution was sonicated for 30 minutes. To this solution was added 5 ml of 20% TEOS in ethanol to act as the silica precursor for coating the CuO particles. The solution was subsequently stirred for 1 hour, then filtered dried at 100 ℃ and calcined at 350 ℃ for 3 hours.

Preparation of copper oxide (CuO) supported on silica spheres (CuO@LA/ SiO_2 or CuONPs/ SiO_2)

Supported copper catalysts were prepared by first dispersing 0.25 g of the copper oxide (**CuO@LA or CuONPs**) nanoparticles in 100 mL of ethanol (1g PVP, MW=10 k) solution. To this 10 mL of 25% ammonia solution of was added and the solution was sonicated for 30 minutes. A theoretical amount of TEOS solution (1.5 mL TEOS to give approximately 0.406 g SiO_2) was then hydrolysed in-situ to make ~50 % (or even higher loading) of Cu/SiO_2. The solution was stirred for 2 hours to completely precipitate the TEOS solution, The precipitate was filtered dried at 100 ℃ and then calcined at 350 ℃ for 3 hours.

Characterization techniques.

TEM, XRD and TPR were used as characterization techniques to evaluate the synthesized materials. Chemisorption of nitrous oxide on Cu was used to determine the atomic surface area of the metal.

4.1.3 Results and discussion

4.1.3.1 TEM, Transmission electron microscopy

The TEM images display the morphology of the copper oxide nanoparticles synthesiszed by the four different methods; all of the observed NPs appear to be predominantly spherical in nature. The CuOK and CuOK@SiO_2 (Figure 4.1 and 4.2) catalysts display large CuO aggregates with an average diameter of about 250 nm, the CuOK@SiO_2 particles display a thin silica layer (of $\pm$ 9 nm, Figure 4.2b) surrounding the metal oxide particles. The particles size of CuONPs and CuO@LA catalyst systems respectively are in the nano regime and are well dispersed on the spherical silica supports as shown in Figure 4.3 and 4.4. It also observed that it was possible to load the particles homogenously on the silica spheres using the one pot synthesis method. This is because the metal oxide nanoparticles are able to bind on the silica spheres while the support is still in the solvent. The presence of a large amount of functional groups (i.e. Si-OH groups) on the surface facilitated in loading the nanoparticles.

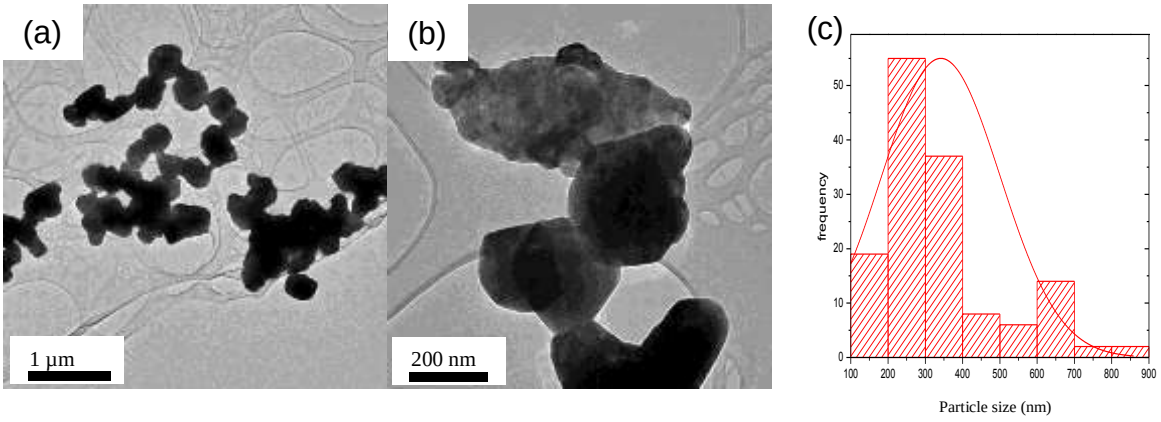


Figure 4. 1: TEM images of CuOK

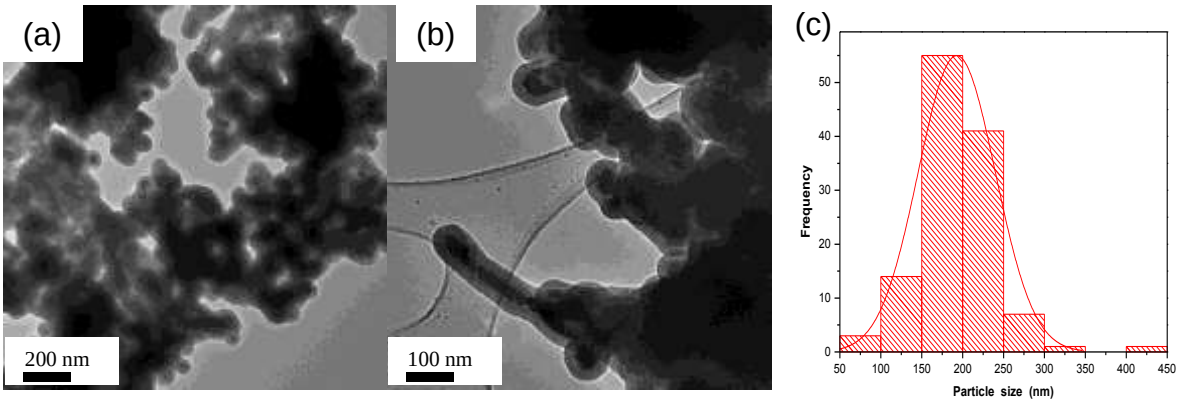


Figure 4. 2: TEM images of $CuOK@SiO_2$

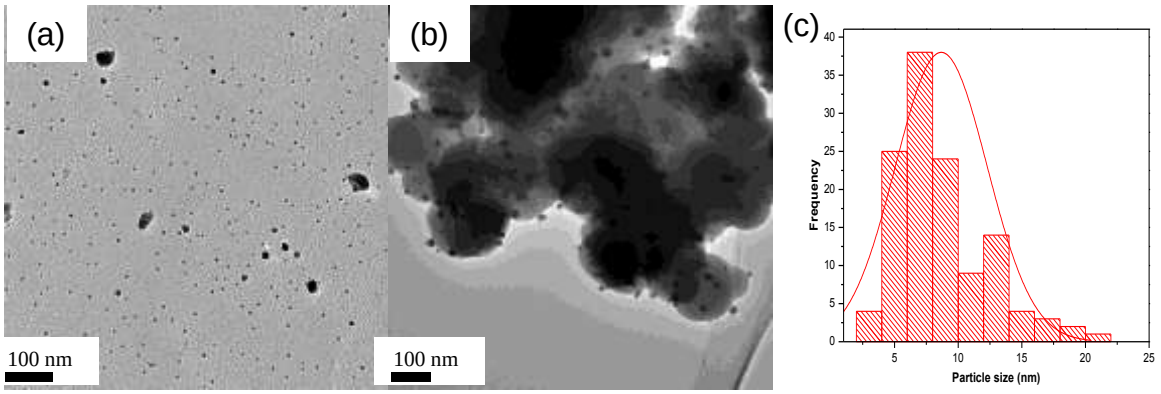


Figure 4. 3: TEM images of CuONPs and $CuONPs/SiO_2$

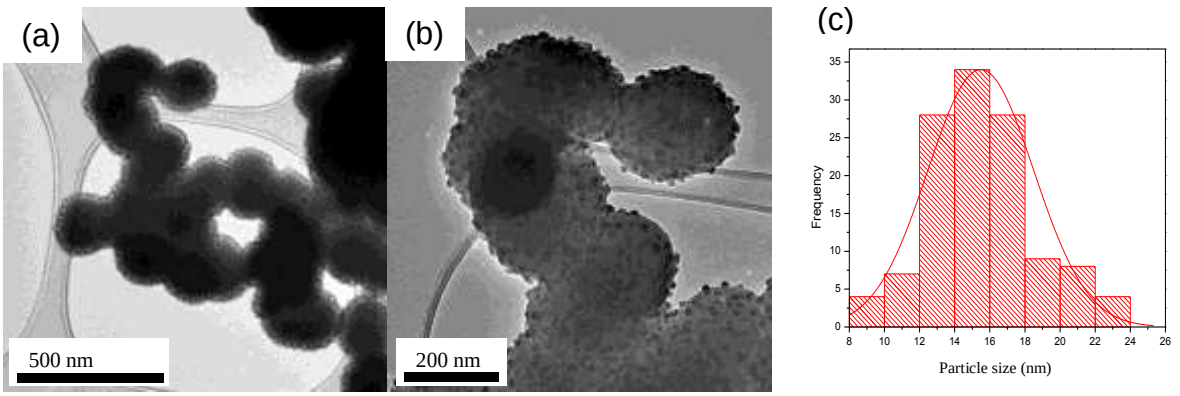


Figure 4. 4: TEM images of $CuO@LA/SiO_2$

4.1.3.2 XRD analysis of the four catalyst system

XRD data shows that nanoparticles are formed with a monoclinic copper oxide phase (Figure 4.5(b). The peaks of the CuOK particles are very well resolved and narrow when compared to the other copper oxide samples as seen in Figure 4.5(a). The amorphous silica peaks found on the supported catalysts is observed at the Bragg angle range of 20-30^{o}.

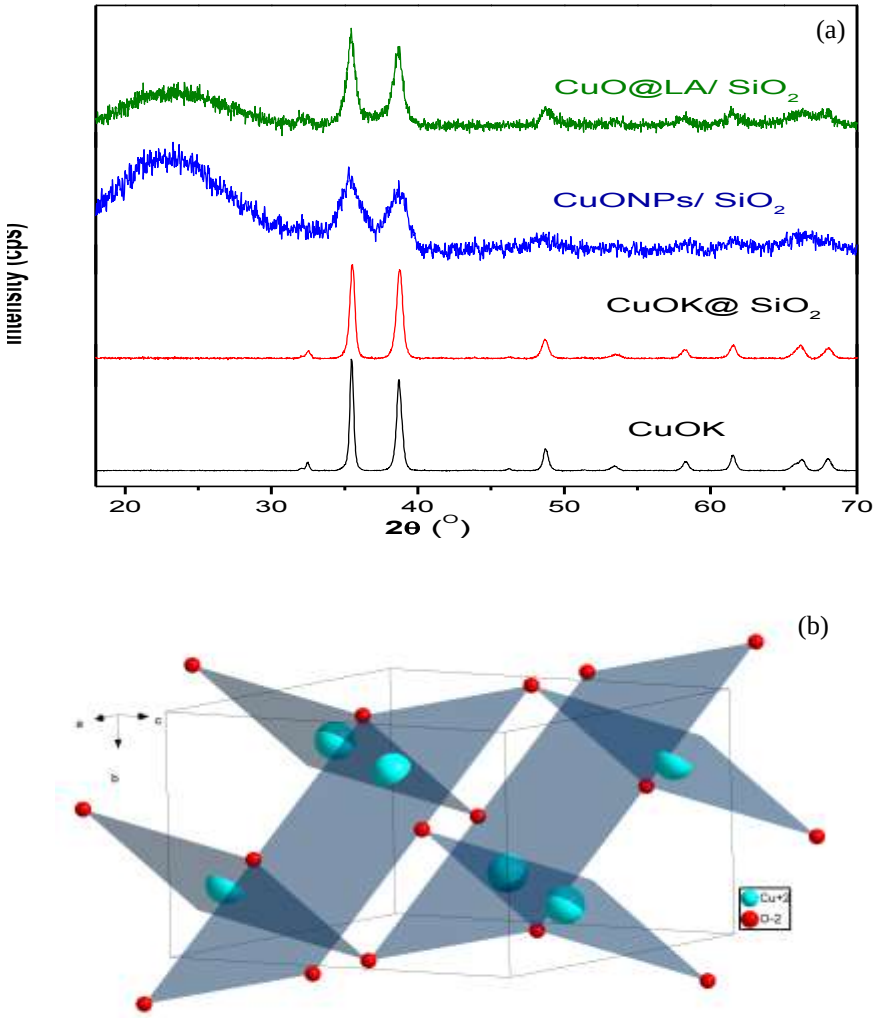


Figure 4. 5: (a) XRD patterns of the synthesized CuO catalysts and (b) the monoclinic CuO unit cell.

Calculation of particle size was performed using the Scherrer equation [15]

$$D_{hkl} = \frac{K \times \lambda}{\beta \times \cos\theta} \quad \text{..... 1}$$

Where D_{hkl} - crystallite size, β- full width half maximum in radians, λ- X-ray wavelength and θ- Bragg angle.

A K factor of 0.9 was used and the instrument line broadening was assumed to be negligible. The two most intense peaks of the diffraction patterns corresponding to the (110) and (111) planes were used to calculate the average crystallite size of the nanoparticles.

Table 4. 1: Crystallite size determination for CuOK using the Scherrer equation.

Sample	Peak number	Peak position (°), Bragg angle (2θ)	FWHM(^{o})	Crystallite size (nm)
CuOK	1	35.48	0.356	23
	2	38.71	0.487	17
CuOK@SiO_2	1	35.13	0.403	20
	2	38.76	0.515	16
CuONPs/SiO_2	1	35.29	1.330	6
	2	38.82	1.583	5
CuO@LA/SiO2	1	35.44	0.713	11
	2	38.76	0.838	10

The particle/crystallite sizes obtained using the Scherrer equation are presented in the Table 4.1. It is observed that the CuOK (and CuOK@SiO_2), crystallite size (~16-30

nm) relative to the average particle size calculated from the TEM images (100-300 nm) are very different this can be due to the fact that the Scherrer equation can only be applied with high degree of certainty to particles with size ranges of up to 100-200 nm which may be made up of a cluster of small CuO NPs **[15]**. Another reason is that is because the calculations only considered the (110) and (111) planes although many large particles are polycrystalline with high index planes exposed on the surface. The application of the Scherrer equation to calculate crystallite sizes of the supported catalysts system gave results consistent with the TEM images (Figure 4.3(c) and 4.4 (c)). The particles on the support are small in the (nano-region) and since many crystalline nanoparticles surface energetics favor the exposure of low index planes {(111), (110), (100)} on the surface **[16, 17]**, therefore the determination of the crystallite size assuming the (111) and (110) planes will in most cases give the particle sizes that are consistent with the ones observed in the TEM images.

4.1.3.3 Temperature programmed analysis (TPR)

TPR analysis was employed to study the reduction temperature of the copper oxide catalysts systems. From the TPR profiles in Figure 4.6 and Table 4.2 it is observed that the reduction temperatures of the four different copper oxide catalyst precursors varied greatly, ranging from 180-350 ℃. The reduction temperatures are greatly dependent on the particle size of the copper oxide particles. The reduction process is rationalized on the basis of the equation below, whereby copper ions are converted to copper zero in one step.

$Cu^{2+} \rightarrow Cu^{0}$ 2

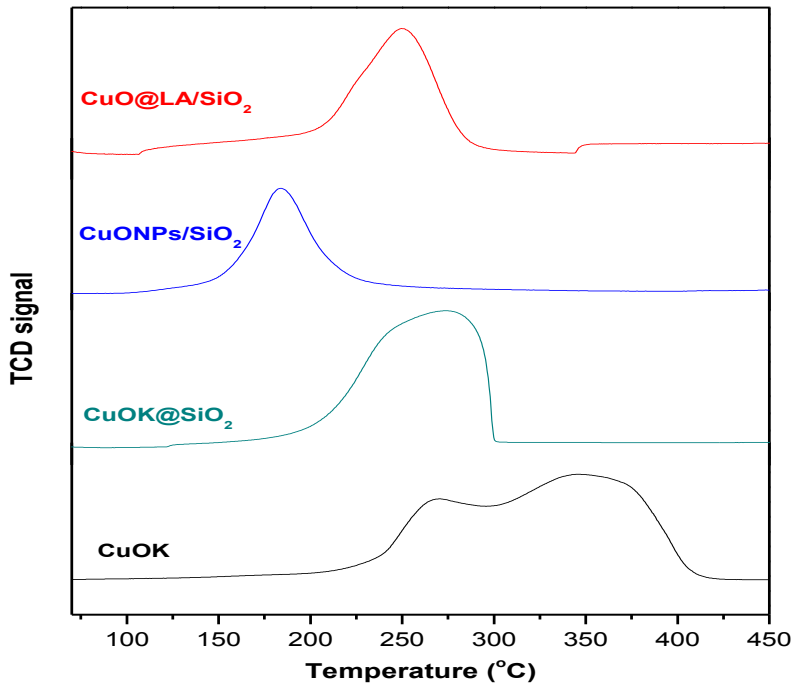


Figure 4. 6: TPR profiles of the CuO particles

Table 4. 2: Reduction temperatures of the different CuO particles

Sample name	First reduction peak (℃)	Second reduction peak (℃)
CuOK	270	346
$CuOK@SiO_2$	273	-
$CuONPs/SiO_2$	185	-
$CuO@LA/SiO_2$	249	-

The small copper oxide nanoparticles are reduced at lower temperatures because most of their copper oxide atoms are easily exposed on the surface due to the inherent high surface to bulk atomic ratios of the nanoparticles. The lower reduction temperatures

are observed on the two supported catalysts systems CuONPs/SiO_2 (reduced at 183 ℃) and CuO@LA/SiO_2 (reduced at 249 ℃). These catalysts have approximate average copper oxide particles sizes of 8 and 15 nm respectively as determined using TEM analysis (see Figure 4.3 and 4.4). However large copper oxide particles (i.e. CuOK and CuOK@SiO_2) with particle sizes ranging from 100-200m are reduced at relatively high temperatures since a significant amount of kinetic energy is needed for the hydrogen gas to penetrate in to the bulk atoms of the micro particles and therefore the reduction peaks are shifted to higher temperatures.

4.1.3.4 Calculating the surface area of Cu active sites under the reaction conditions.

Metal surface areas and metal dispersions are commonly determined using chemisorption techniques by employing appropriate adsorbate gases such a carbon monoxide, hydrogen and nitrous oxide. The surface area of the exposed copper nanoparticles is commonly determined using nitrous oxide (N_2O). The surface area is used to determine the efficacy of the active catalysts sites **[18]**. The method of determining the atomic surface area on the copper catalysts is based on the decomposition of the nitrous oxide on a copper surface. The decomposition process is followed by the release of a nitrogen molecule coinciding with the oxidation of the copper metal surface at moderate reaction temperatures this process avoids bulk oxidation of the metal particles.

$$N_2O\,(g) + 2Cu_s \rightarrow N_2\,(g) + (Cu\text{-}O\text{-}Cu)_s \quad \text{..... 3}$$

The reaction involves adsorption of N_2O on the surface of the copper nanoparticles followed by its decomposition into nitrogen and adsorbed oxygen atom. The reaction of the dinitrogen oxide on the copper surface corresponds to a surface stoichiometry of Cu_s/ $O_{adsorbed}$ of 2:1. The calculations for the surface area are done assuming the low index copper planes (100), (110) and (111). The chemisorption temperature plays an important role and there is an optimum temperature at which only the surface oxidation of the copper nanoparticles is possible. The optimum temperatures is in the

range of 70-100 ℃. Temperatures above this range result in bulk oxidation of the copper particle. At lower temperatures nitrous oxide decomposition is greatly lowered and therefore the monolayer coverage of the adsorbate is not representative of the entire exposed copper surface area **[19, 20]**.

Mellor et al.**[21]** used a pulsed chromatographic method to determine the copper surface area. Certain features had to be considered to get reliable results; these included 1) the mass of sample 2) the copper surface atomic density 3) the reaction temperatures and 4) the volume of nitrous oxide used. Therefore, from the optimisation process Mellor et al.**[21]** concluded that the optimum conditions for determining the Cu surface using the chromatographic technique are: copper surface atomic density of 1.35×10^{19}, reaction temperature (90 ℃) and sample mass ($\sim$ 1 g).

Experimental

Apparatus

A Varian 3300 gas chromatograph equipped with a thermal conductivity detector connected to a Clarity DataApex software peak integrator was used. Helium gas was used as the carrier gas. Nitrogen, hydrogen and nitrous oxide gases were obtained from Afrox and were used without any further purification.

Two six port valves were connected to both the reactor and the gas chromatograph (GC). The GC was equipped with a porapack Q column to allow the separation of the different gases. Known volumes of nitrous oxide were injected in the helium stream using the six port valve via a connected sample loop. Before the analysis of the catalyst samples the detector was calibrated for nitrogen gas using different sample loops to obtain a calibration curve for calculating the amount of nitrous oxide converted during the reaction using the relationship based on equation 3.

The catalyst was subjected to pre-treatment steps equivalent to the treatment steps that were applied to the catalyst prior to synthesis of the carbon nanofibers. This was

done so as to make sure that the sample surface area studied using the chemisorption technique is representative of the catalysts used to deposit the CNF_S.

Calculation of copper surface area

The surface area of the copper is calculated using the volume of nitrogen liberated during the reaction assuming the reaction occurs via reaction 1. The copper surface atomic density is calculated assuming amount that the (100), (110) and (111) low index planes on the copper surface have surface densities of 1.35×10^{19} atoms/m^2, 1.46×10^{19} atoms/m^2 and 1.68×10^{19} atoms/m^2

Table 4. 3: Relationship of the atomic site densities and the maximum amount of nitrous oxide that can decompose assuming full monolayer coverage.

Atomic site density (atoms/m^2)	V' of N_2O decomposed at STP (mL/m^2)[a]
1.35×10^{-19}	**0.251**
1.46×10^{-19}	0.271
1.68×10^{-19}	0.313

[a] obtained using the ideal gas equation (PV = nRT) and assigning an N_2O: Cu stoichiometry of 2:1

Volume of the reacted N_2O is converted to STP using the amount of N_2 liberated using the following equation:

$$V_{N_2O}(STP) = \frac{P_A \times 273\ K \times A_r \times V_{cal}}{T_r \times 760 Torr \times A_{cal}} \quad \ldots\ldots 4$$

P_A = ambient pressure (Torr)

T_r = chemisorption temperature (K)

A_r = Average nitrogen peak area due to the chemisorption reaction

A_{cal} = Nitrogen calibration peak

V_{cal} = Nitrogen calibration gas volume (mL)

The copper surface area ($m^2.g^{-1}$) is thus approximated using the equation:

$$S_{Cu} = {V_{N_2O}(STP)} \Big/ {V'_{N_2O}(STP) \times m} \text{ .... } 5$$

m = mass of sample (three trial runs for each sample with m ~ 0.1, 0.5 and 1g)

4.1.3.5 Obtained surface areas of the different catalysts.

Figure 4.7, shows the trace analysis an example of the outgoing gases (i.e. the produced N_2 and unreacted N_2O) during analysis. It is observed that after the first gas injection the nitrogen peak is high and it then decreases after subsequent injections. Five injection pulses were needed to ensure complete reaction of the exposed copper surface atoms with nitrous oxide.

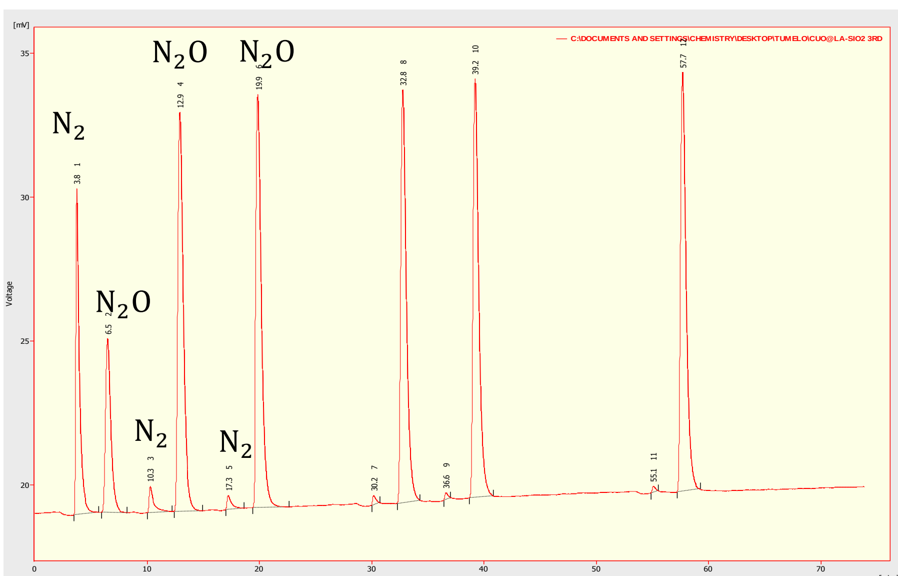


Figure 4. 7: Typical gas trace during the nitrous oxide chemisorption process, nitrogen gas was eluted first followed by the unreacted nitrous oxide. Helium was used as the carrier gas.

Table 4. 4: Calculated surface area of the Cu catalysts using N2O chemisorption determined from equation 4 and 5.

Sample name	Average Cu atomic surface area $(m^2/g)^a$
CuOK	0.16
$CuOK@SiO_2$	0.64
$CuONPs/SiO_2$	9.65
$CuO@LA/SiO_2$	6.33

a = average surface area calculated from three trial runs using different catalyst masses ranging from 0.1-1g. Results agree with each other with a ± 10 error bar, using surface atomic density 1.35×10^{-19} assuming equal areas of the (100), (110) and (111) planes.

The calculated atomic surface (Table 4.4) indicated that the metal nanoparticles after the reduction process have an increased number of surface atoms at the set reaction conditions (i.e. conditions in which the carbon nanofibers are grown, T= 300 ℃ and atmospheric pressure $\sim$ 1 bar). After reduction the large copper aggregates resulting from the CuOK and $CuOK@SiO_2$ precursors have very few exposed surface atoms thus resulting in a low atomic surface area. It has been noted that the surface to bulk atomic ratio of metal nanoparticles increased as the particles became smaller. The supported Cu nanoparticles (CuONPs and $CuO@La/SiO_2$) displayed a high atomic surface area in comparison to the large Cu particles of (CuOK and $CuOK@SiO_2$). The high surface areas indicate that the metal nanoparticles do not undergo sintering during the reduction process and therefore it is expected that these metal nanoparticles are in the nano-regime when they come into contact with the acetylene gas during the fiber growth process.

4.1.4 References

1. Gu A, Wang G, Zhang X, Fang B: **Synthesis of CuO nanoflower and its application as a H_2O_2 sensor**. *Bulletin of Materials Science* 2010, **33**(1):17-20.
2. Pan K, Ming H, Yu H, Liu Y, Kang Z, Zhang H, Lee ST: **Different copper oxide nanostructures: Synthesis, characterization, and application for C-N cross-coupling catalysis**. *Crystal Research and Technology* 2011, **46**(11):1167-1174.
3. Ren G, Hu D, Cheng EWC, Vargas-Reus MA, Reip P, Allaker RP: **Characterisation of copper oxide nanoparticles for antimicrobial applications**. *International journal of antimicrobial agents* 2009, **33**(6):587-590.
4. Lim Y-F, Choi JJ, Hanrath T: **Facile synthesis of colloidal CuO nanocrystals for light-harvesting applications**. *Journal of Nanomaterials* 2012, **2012**:4.
5. Meyer B, Polity A, Reppin D, Becker M, Hering P, Klar P, Sander T, Reindl C, Benz J, Eickhoff M: **Binary copper oxide semiconductors: From materials towards devices**. *physica status solidi (b)* 2012, **249**(8):1487-1509.
6. Yasuda Y, Ide E, Morita T: **Evaluation of Copper Oxide-Based Interconnecting Materials**. *Open Surface Science Journal* 2011, **3**:123-130.
7. Dang TMD, Le TTT, Fribourg-Blanc E, Dang MC: **Synthesis and optical properties of copper nanoparticles prepared by a chemical reduction method**. *Advances in Natural Sciences: Nanoscience and Nanotechnology* 2011, **2**(1):015009.
8. Suzuki K, Tanaka N, Ando A, Takagi H: **Size-selected copper oxide nanoparticles synthesized by laser ablation**. *Journal of Nanoparticle Research* 2012, **14**(5):1-11.
9. Palacios-Hernández T, Hirata-Flores GA, Contreras-López OE, Mendoza-Sánchez ME, Valeriano-Arreola I, González-Vergara E, Méndez-Rojas MA:

Synthesis of Cu and Co metal oxide nanoparticles from thermal decomposition of tartrate complexes. *Inorganica Chimica Acta* 2012, **392**:277-282.

10. Estruga M, Roig A, Domingo C, Ayllón JA: **Solution-processable carboxylate-capped CuO nanoparticles obtained by a simple solventless method**. *Journal of Nanoparticle Research* 2012, **14**(8):1-9.
11. Kida T, Oka T, Nagano M, Ishiwata Y, Zheng XG: **Synthesis and application of stable copper oxide nanoparticle suspensions for nanoparticulate film fabrication**. *Journal of the American Ceramic Society* 2007, **90**(1):107-110.
12. Bhoware S, Maubane MS, Phaahlamohlaka T, Shaikjee A, Coville NJ: **Cu grown carbon nanofibers–variation of their chemical and physical properties**. *Chemical Physics Letters* 2013.
13. Zhao Y, Zhu JJ, Hong JM, Bian N, Chen HY: **Microwave-Induced Polyol-Process Synthesis of Copper and Copper Oxide Nanocrystals with Controllable Morphology**. *European Journal of Inorganic Chemistry* 2004, **2004**(20):4072-4080.
14. Li L, He S, Song Y, Zhao J, Ji W, Au C-T: **Fine-tunable Ni@porous silica core–shell nanocatalysts: Synthesis, characterization, and catalytic properties in partial oxidation of methane to syngas**. *Journal of Catalysis* 2012, **288**(0):54-64.
15. Holzwarth U, Gibson N: **The Scherrer equation versus the'Debye-Scherrer equation'**. *Nature Nanotechnology* 2011, **6**(9):534-534.
16. Frenken JWM, Stoltze P: **Are Vicinal Metal Surfaces Stable?** *Physical Review Letters* 1999, **82**(17):3500-3503.
17. Tao AR, Habas S, Yang P: **Shape control of colloidal metal nanocrystals**. *Small* 2008, **4**(3):310-325.
18. Fadoni M, Lucarelli L: **Temperature programmed desorption, reduction, oxidation and flow chemisorption for the characterisation of**

heterogeneous catalysts. Theoretical aspects, instrumentation and applications. *Studies in Surface Science and Catalysis* 1999, **123**:289-342.

19. Evans JW, Wainwright MS, Bridgewater AJ, Young DJ: **On the determination of copper surface area by reaction with nitrous oxide**. *Applied Catalysis* 1983, **7**(1):75-83.
20. Chen C-S, Lin J-H, Lai T-W, Li B-H: **Active sites on Cu/SiO2 prepared using the atomic layer epitaxy technique for a low-temperature water–gas shift reaction**. *Journal of Catalysis* 2009, **263**(1):155-166.
21. Mellor JR: **The water-gas shift deactivation studies**. Johannesburg: Faculty of Science, University of the Witwatersrand; 1993.

4.2 Synthesis of CNFs and purification by Soxhlet extraction

4.2.1 Synthesis of the carbon nanofibers

The synthesis of carbon nanofibers was carried out in an atmospheric catalytic chemical vapour deposition set-up (Figure 4.8). Catalyst powder (5 mg) was placed in a small quartz boat which was placed inside a quartz tube in the middle of a furnace. The furnace was then heated to 300 ℃ (or other set temperatures) at a ramping rate of 10 ℃/min while H_2 (100 ml/min) at atmospheric pressure was passed through the catalyst to activate it. After catalyst activation (30 min), acetylene (C_2H_2) was introduced, together with the H_2, into the reaction vessel at a flow rate of 100 ml/min each (total gas flow rate 200 mL/min) for 30 min. The system was allowed to cool to room temperature under a H_2 flow. Reactions were also performed at different temperatures of 220 and 250 ℃.

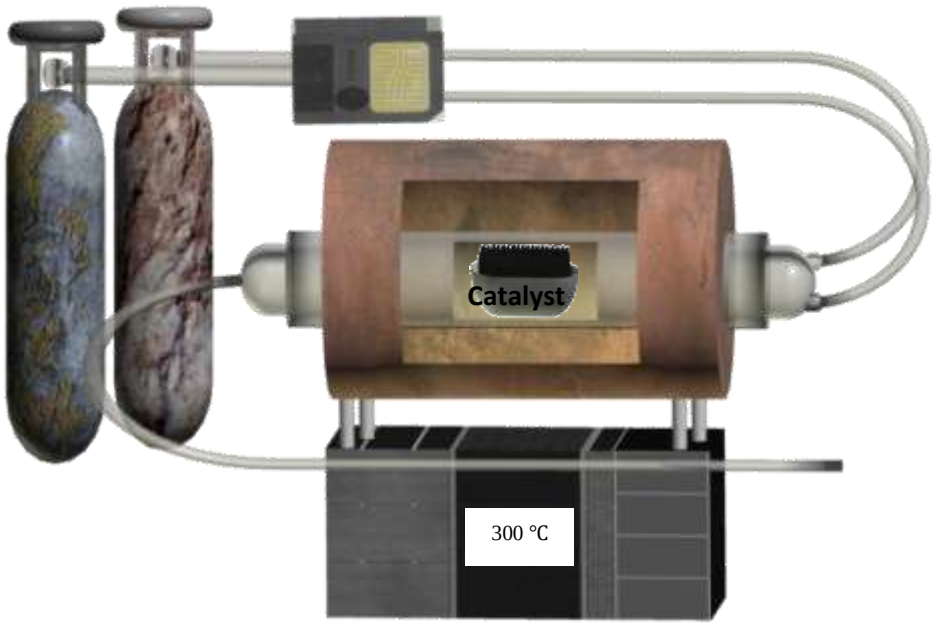


Figure 4. 8: CVD setup used to grow the carbon nanofibers.

4.2.2 TEM analysis of the carbon nanofibers.

The grown carbon nanofibers all have a characteristic brown colour rather the black colour associated with most carbon nanomaterials. The four catalyst systems were used to grow carbon nanofibers. TEM analysis revealed that a variety of carbonaceous materials were formed using the different catalysts with different morphologies (i.e. coiled carbon nanofibers and straight carbon nanofibers). The morphology of the carbon nanofibers appear to depend on the size of catalyst particles, provided the reaction conditions were kept the same for each catalyst system.

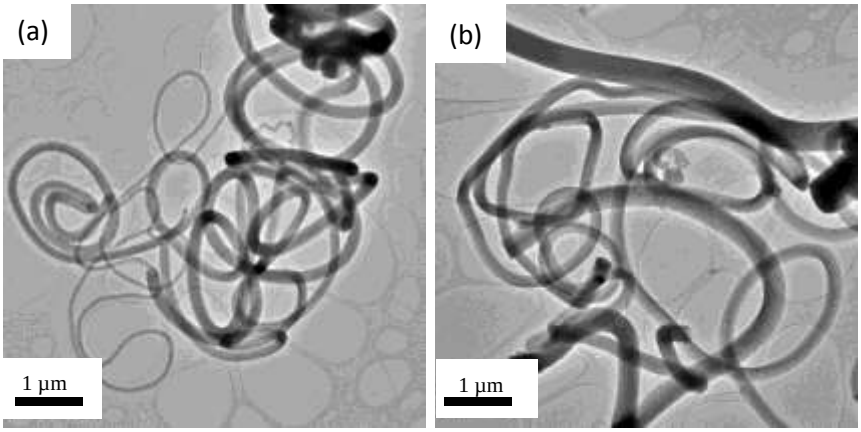


Figure 4. 9: Straight CNFs grown on the unsupported copper catalysts (CuOK)

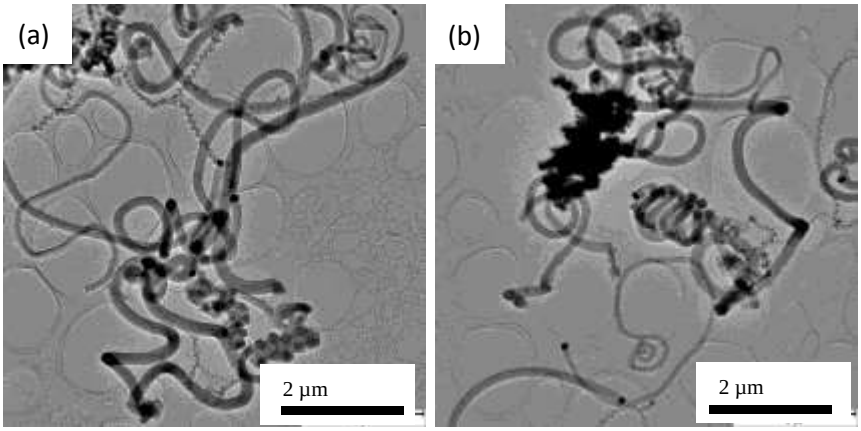


Figure 4. 10: TEM images of CNFs(straight and helical) synthesised using (CuOK@SiO_2)

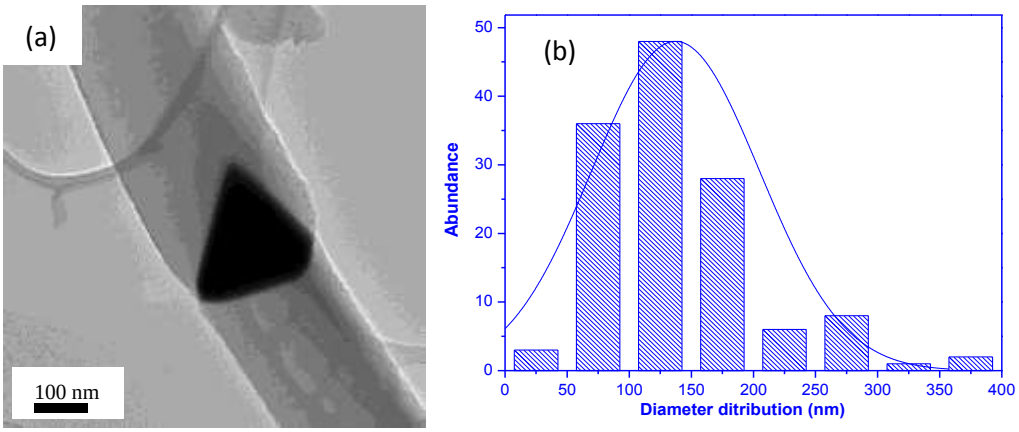


Figure 4. 11: Faceted Cu nanoparticle and diameter distributions of the straight carbon nanofibers.

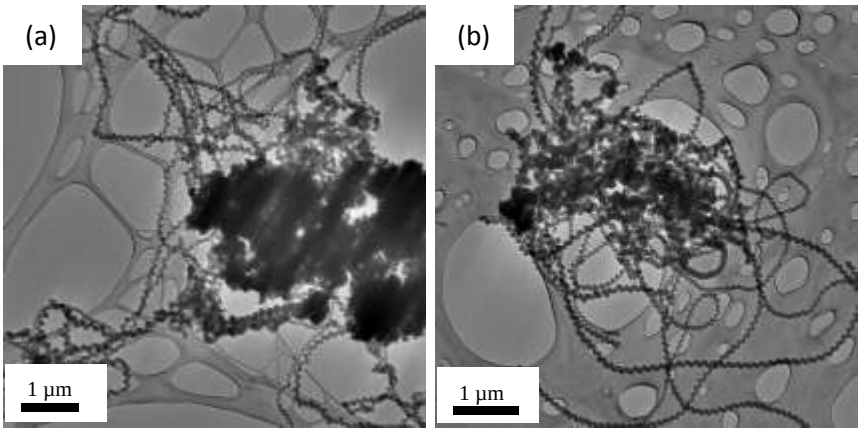


Figure 4. 12: Coiled CNFs grown on CuONPs/SiO_2

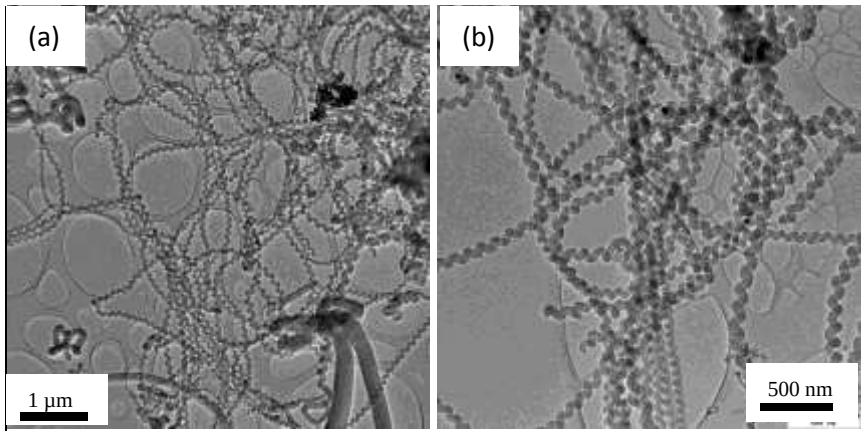


Figure 4. 13: Coiled CNFs grown by CuO@LA/SiO_2

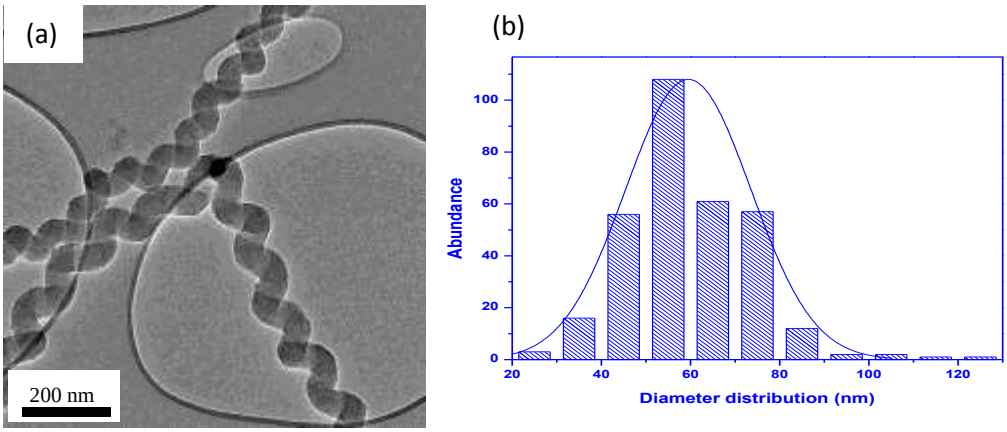


Figure 4. 14: Faceted Cu nanoparticle and diameter distributions of the helical carbon nanofibers

The results obtained show that the carbon nanofibers (both straight and coiled) grow on faceted copper nanoparticles (Figure 4.11(a) and 4.14(a)). There has been reports indicating that this faceting of the metal nanoparticles takes place immediately after the exposure of the Cu to carbon precursor **[1, 2]**. The unsupported catalyst particles yield straight carbon nanofibers (as seen in Figure 4.9 and 4.10) with large diameters ($\pm$120 nm). This is because the catalyst particles undergo sintering as the particles are not anchored on any support. Therefore upon heating and introduction of a highly reactive gas such as acetylene the copper particles agglomerate (or fragment) to lower the surface energy of the exposed copper atoms. The coated catalyst particles ($CuOK@SiO_2$) are already large at the time of acetylene introduction thus resulting in fibres with large diameters. Small copper nanoparticles tend to yield coiled carbon nanofibers, (Figure 4.12 and 4.13). There seems to be an optimum particle size for growing coiled carbon nanofibers since the particles imbedded in the fibre have average diameter of around $\pm$61 nm. This is approximately equal to the fiber diameter. Thus there is still agglomeration of the supported copper nanoparticles upon exposure to the acetylene gas. The limited sintering can also explain the faceting of the metal nanoparticles due to the growth of the smaller nanoparticles.

Table 4. 5: Carbon nanofiber yields.

Sample	Mass CNFs (g)	%yield=$(\frac{m_p - m_c}{m_c}) \times 100$[a]	%yield= $\frac{m_{Carbon}}{m_{Acetylene}} \times 100$[b]	%coiled CNFs
CNFs-CuOK	0.5115	10130	60	~0
CNFs-CuOK@SiO_2	0.1326	4985	16	≤ 5
CNFs-CuONPs/SiO_2	0.1977	3855	23	≥90
CNFs-CuO@LA/SiO_2	0.2168	4236	25	≥90

[a] m_p total mass of the product, m_c mass of catalyst powder used.

[b] $m_{acteylene}$ obtained from n of acetylene calculated using van der Waals equation of state for a real gas. $\mathbf{n^3\left(\frac{ab}{V^2}\right) - n^2\left(\frac{a}{V}\right) + n(RT + Pb) - PV = 0}$, where a and b are 4.516 bar L^2/mol^2 and 0.0522 L/mol respectively for acetylene **[3]**

Table 4.5 indicates the average yields for the different catalysts systems. The unsupported catalyst (CuOK) offered a higher carbon yield. This is due to the fact that the copper nanoparticles are not covered by an inactive phase. The supported catalyst contains silica spheres as the support and gave lower yield as compared to the unsupported catalyst. However this results to do not entail that the supported catalyst (CuONPs/SiO_2 and CuOLA/SiO_2) although growing carbon nanofibers with a different morphology is less active than the bare copper nanoparticles because the loading of copper particles supported on an inactive phase (SiO_2) is lower than that of the unsupported catalyst (CuOK). The silica sphere supported catalyst containing an equivalent amount of copper to that of the unsupported catalyst gave approximately

the same yield per carbon atom. Thus the growth rate of the straight and helical carbon nanofibers is approximately same when the growth conditions are kept constant. The silica coated copper oxide catalyst ($CuOK@SiO_2$) generated a lower carbon yield in comparison to its uncoated counterpart (CuOK). The silica layer lowered the rate of interaction of the carbon precursor (acetylene) with the exposed copper surfaces.

4.2.3 Effect of growth temperature on growth of carbon nanofibers.

Different temperature regimes below 300 ℃ were studied to elucidate the type of CNFs grown using catalysts CuOK and also to determine if the temperature of 300 ℃ is the optimum temperature. Growth of the carbon nanofibers at lower temperatures (i.e below 300 ℃) is limited as observed by the catalytic yield of the CNFs (Table 4.6). The electron microscopy images of the carbon nanofibers show that there is a different growth rate at different growth temperatures. The length of the carbon nanofibers decreased with decreasing growth temperature. This is shown in the TEM images (Figure 4.15 and 4.16). This implies that there is insufficient activation energy for the catalyst systems to deposit CNFs at an optimum rate under the low temperature growth conditions (H_2-100 sccm and C_2H_2-100 sccm, at atmospheric pressure). Another reason for the poor growth rate is the fact that the catalyst nanoparticles are not completely reduced at the lower temperatures as inferred from the TPR data. This leaves an oxide layer on the catalyst surface. The oxide layer then results in poor exposure of the copper surface planes which are more active for adsorbing and dissociating the carbon source **[4, 5]**

Table 4. 6: Table illustrating the effect of growth temperature on the yield of the carbon nanofibers

Sample	**Mass CNFs (g)**	**%yield=($\frac{m_p - m_c}{m_c}$)× 100**	**%yield= $\frac{m_{Carbon}}{m_{Acetylene}} \times 100$**	**Growth temperature**
SCNFs	0.5115	10130	60	300
SCNFs	0.0366	632	4	250
SCNFs	0.0242	384	3	220

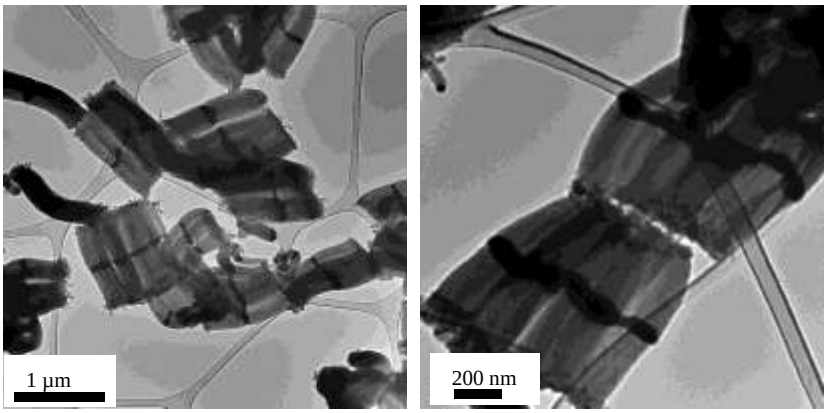


Figure 4. 15: TEM images of SCNFs grown at 220 ℃

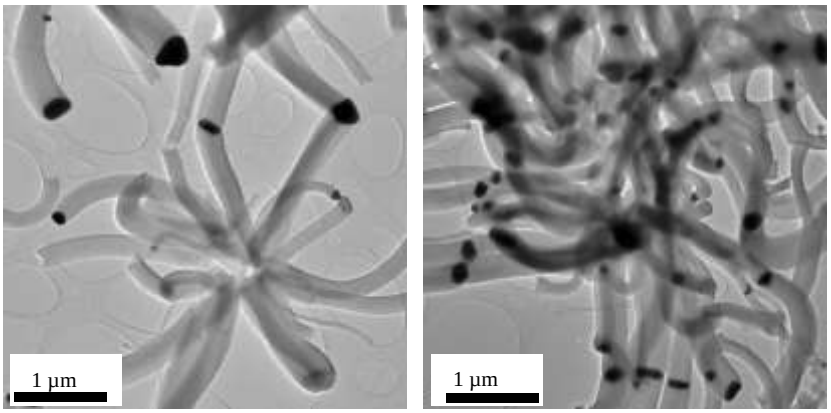


Figure 4. 16: TEM images of SCNFs grown at 250 ℃.

4.2.4 Soxhlet extraction studies.

It has been noted that carbon nanofibers grown at low temperatures are amorphous in nature (observed by IR spectroscopy and XRD studies) **[6, 7]**. This therefore shows that the growth of these materials proceeds by incomplete decomposition of the carbon source. The results of such incomplete decomposition are that the carbon materials contain a high content of polycyclic aromatic hydrocarbons (PAHs). These PAHs are known to be carcinogens **[8]** and they need to be removed. Soxhlet extraction using organic solvents (i.e. toluene) is a perfect method to carry out this procedure because most of the PAHs are soluble in the solvents. Possible PAHs expected are shown in Figure 4.17.

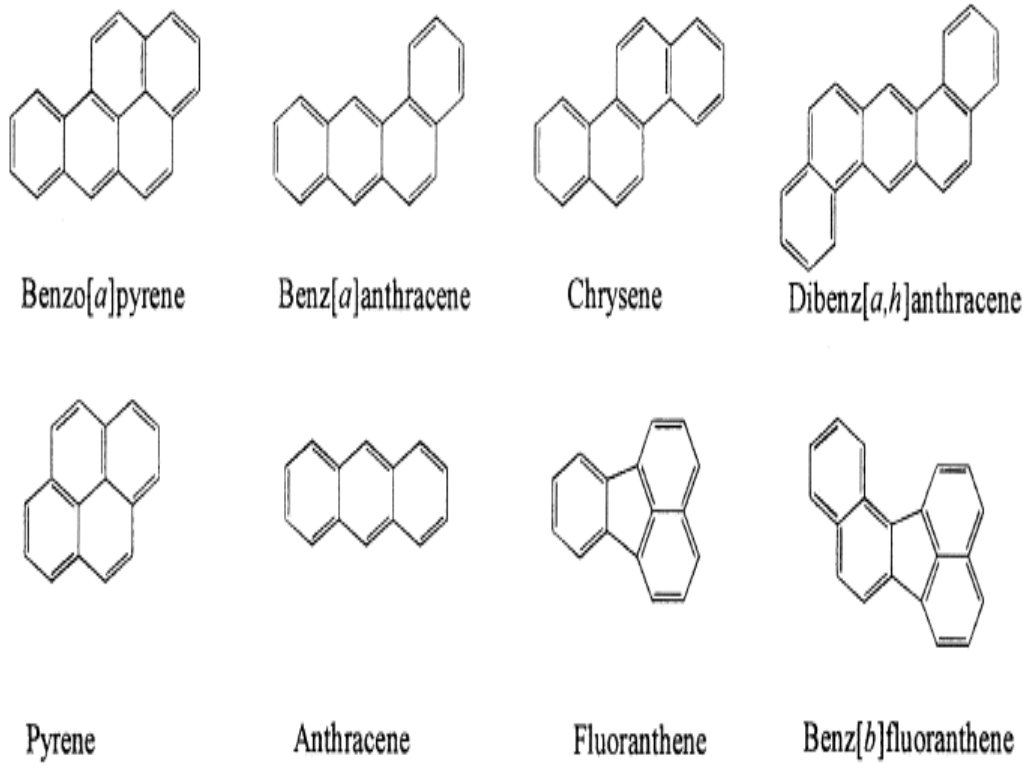


Figure 4. 17: Possible PAHs in the carbon nanofibers samples **[8]**

4.2.4.1 Soxhlet extraction procedure

The carbon nanofibers were studied to determine the effect of the PAHs on the carbon structure and surface properties. The extraction was performed on CNFs at different times using toluene at 140 ℃. CNFs synthesized using acetylene gas preheated at different temperatures were also subjected to the extraction and characterized using IR spectroscopy and TGA.

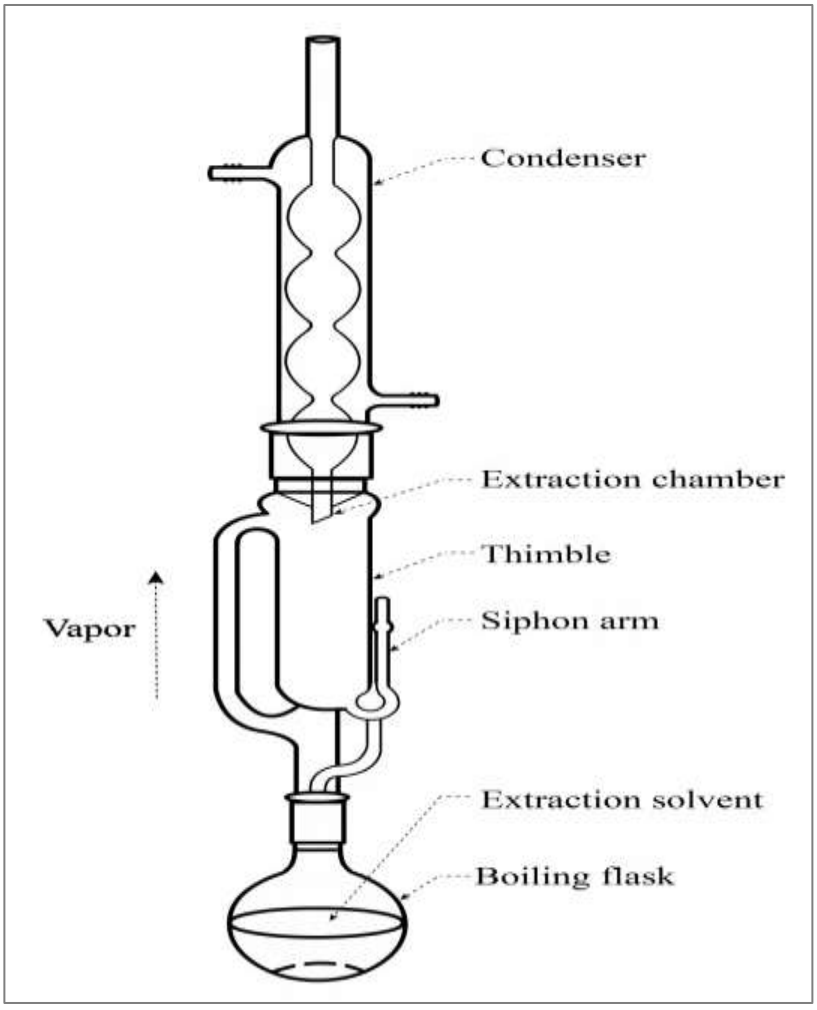


Figure 4. 18: Soxhlet extraction set-up.

Extraction at different times

As synthesised carbon nanofibers (SCNF) were extracted for different times (0.25, 0.5, 1, 2 and 6 hours). Complete extraction of the organics from the fiber structure was observed after 30 min extraction. This was based on the color of the toluene liquid inside the thimble. When the liquid in the thimble was yellow it indicates the presence of PAHs.

4.2.4.2 IR spectroscopy

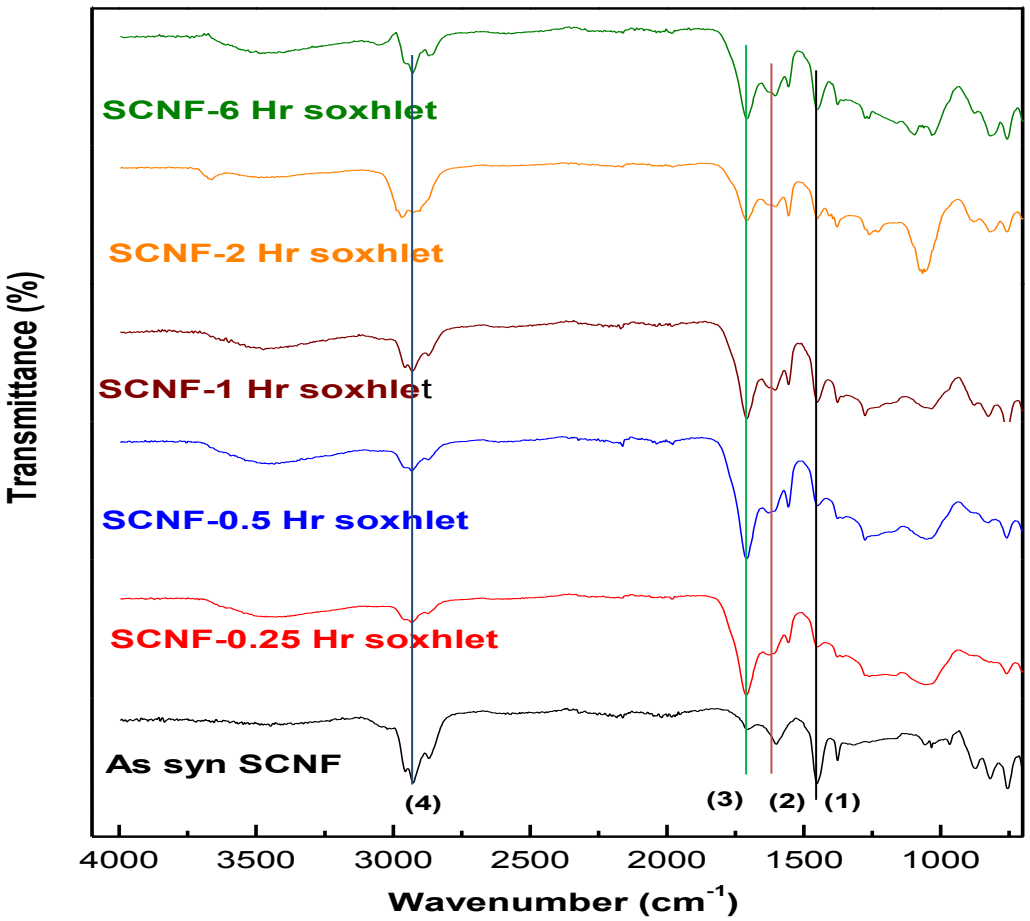


Figure 4. 19: IR spectra of the CNFs after different Soxhlet extraction times.

The IR spectra (Figure 4.19) display the surface structural characteristics of the carbon nanofibers that have been subjected to Soxhlet extraction at different times. Four different spectral vibrational modes are seen to vary in intensity with the extraction time: (1) peak 1451 cm^{-1}, (2) 1602 cm^{-1} (3) 1702 cm^{-1}, (4) 2900 cm^{-1}. Peak (1) which is due to C-H vibrations of $-CH_2$, decreases in relative intensity as extraction proceeds. The observation shows that C-H groups are extracted from the fiber. The peak at 1602 cm^{-1} which has been attributed to a C=C vibration associated with aromatic groups also showed decreased intensity after extraction at different times. This therefore confirms that the extraction procedure removes the PAH groups adsorbed on the fiber surfaces. Peak (4) is due to C-H vibrations of alkyl groups and peak (3) is due to carbonyl group (C=O) vibrations **[9]**. The peak intensity of the carbonyl groups increases relative to the C-H peak intensity. We attribute the change in the peak intensities to the oxidation of the alkyl groups during Soxhlet extraction because the process was performed in open air.

4.2.4.3 TGA and DTG analysis

TGA (Figure 4.20) analysis of the Soxhlet extracted CNFs was also performed and the data shows the PAH extraction of the carbon nanofibers only slightly affected the decomposition temperature of the fibers. It was observed that carbon nanofibers that had been subjected to longer extraction times only showed an increase in thermal stability of the CNFs by a ± 10 ℃ change in temperature. It is however clear that the extraction procedure removes some of the easily solubilized materials. The carbon materials that are not fully purified showed only one decomposition peak as shown in Table 4.7. After complete Soxhlet extraction a second decomposition peak appeared at temperatures about 400 ℃. This indicates that the volatile PAH material that were adsorbed on the CNFs dominated the TGA curves before the extraction process.

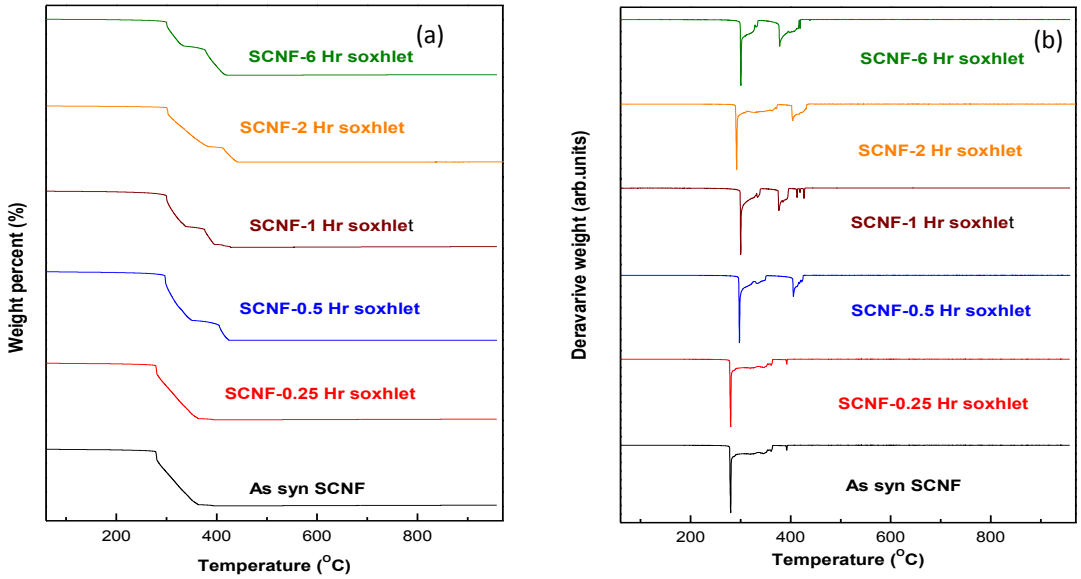


Figure 4. 20: TGA and DTG of the soxhlet extracted CNFs

Table 4. 7: Decomposition temperatures of the extracted straight carbon nanofibers.

Sample name	First decomposition temperature (℃)	Second decomposition temperature (℃)
As syn SCNF	279	-
SCNF- 0.25 hr soxhlet	280	-
SCNF- 0.5 hr soxhlet	297	404
SCNF- 1 hr soxhlet	300	376
SCNF- 2 hr soxhlet	291	403
SCNF- 6 hr soxhlet	300	378

4.2.4.4 Effect of preheating acetylene on the CNFS surface functional groups.

To validate that the extraction process indeed works, carbon nanofibers were synthesised in a double stage furnace. The acetylene was preheated at different temperatures so as to influence the way it decomposes on the surface of the catalysts. Pre-heating temperatures used were 500 ℃ and 750 ℃ (close to the thermal decomposition of acetylene of 770 ℃). The surface functional groups appear to be influenced by the preheating temperature (Figure 4.21(a)). The vibrational modes are similar for the carbon nanofibers synthesised without preheating the gas feed at different temperatures. However the relative intensities in each product are different for the pre-heated samples. For the CNFs synthesised by preheating the acetylene at 750 ℃, the intensity representing the vibrational mode of carbonyl groups (1702 cm^{-1}) is high showing a high content of C=O relative to the C-H alkyl groups (2900 cm^{-1}). Preheating the acetylene at 500 ℃ did not affect the IR spectrum of the synthesised material since the spectrum is not significantly different from the spectrum in Figure 4.19 of the CNFs obtained when the acetylene was fed into the reactor without any pre-treatment.

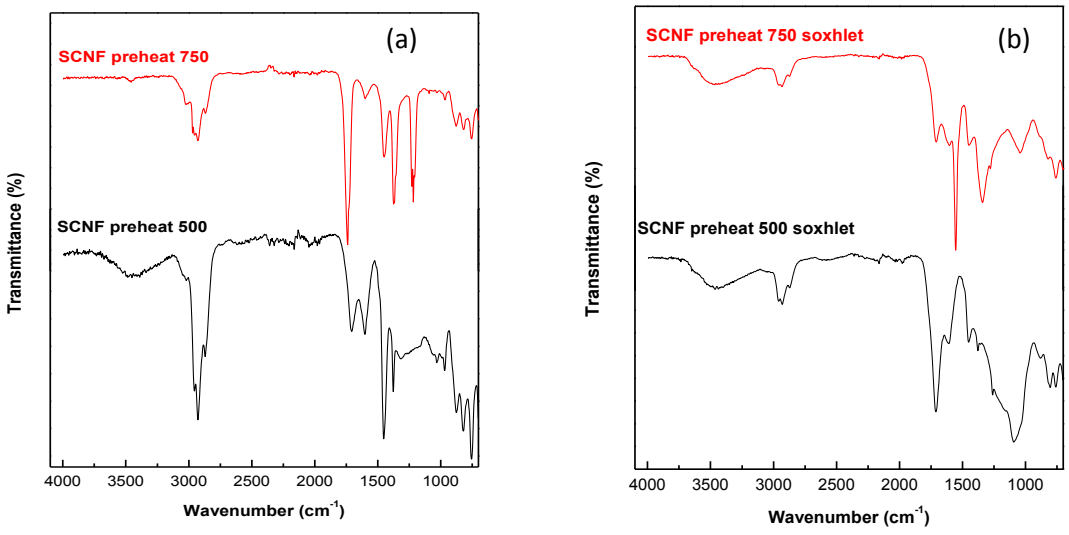


Figure 4. 21: IR data (a) before and (b) after Soxhlet extraction as a function of acetylene preheating.

After Soxhlet extraction the IR spectra (Figure 4.21(b)) of the carbon nanofibers displayed few vibrational bands thus indicating that most of the vibrations where due to adsorbed hydrocarbons on the surface of the fibres. The C-H (1451 cm^{-1}) peak due to a methylene group is decreased after the extraction process.

4.2.4.5 TGA analysis of the CNFs synthesized by preheating C_2H_2

The thermal stability data for the CNFs grown by pre-heating the inlet gas stream before Soxhlet extraction is shown on Figure 4.22(a),(b) and Table 4.8. The fibres undergo an oxidation before decomposition as shown by an increase in weight percentage highlighted by circles in Figure 4.22(a) before the temperature reaches the decomposition of the fibers. This might also be as a result of Cu being oxidised to CuO. The decomposition temperature of these fibers is high compared to the fibers that were synthesised without preheating the gas stream. We observe (in Figure 4.22(c) and (d)) that purification of the CNFs using Soxhlet extraction reduces the decomposition temperature of the fibers. This therefore indicates that the surface properties of the carbon nanofibers are altered by Soxhlet extraction. The adsorbed hydrocarbons that do not form an integral part of the fiber are removed in the process.

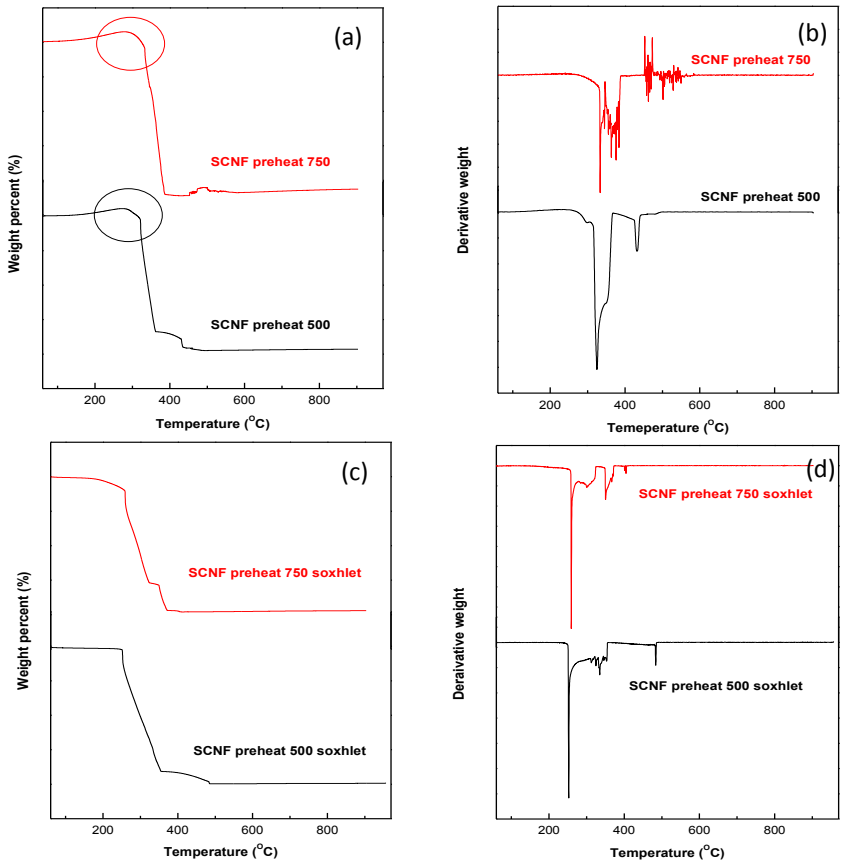


Figure 4. 22: TGA and DTG of CNFs obtained by pre-heating C2H2, before soxhlet (a) and (b), after soxhlet extraction (c) and (d)

Table 4. 8: Decomposition temperatures of the extracted straight carbon nanofibers

Sample name	First decomposition temperature (℃)	Second decomposition temperature (℃)
SCNF preheat 500	324	431
SCNF preheat 750	333	-
SCNF preheat 500 sox	252	-
SCNF preheat 750 sox	258	350

It is therefore concluded that purification of carbon nanofibers to remove polycyclic aromatic hydrocarbons can be performed using a simple Soxhlet extraction procedure. Characterization of the carbon nanofibers before and after Soxhlet extraction using FTIR and TGA analysis shows that there is removal of some adsorbed hydrocarbons, as evidenced by the disappearance of some of the vibrational peaks in the IR spectra and variation of the fiber thermal stability. The presence of the polycyclic aromatic hydrocarbons in the CNFs show that the growth mechanism of this fibres follow a polymer like pathway (as discussed in the literature review, Section 2.3) where C and H atom are both present in the fiber structure in significant amounts.

4.2.5 References

1. Shaikjee A, Franklyn PJ, Coville NJ: **The use of transmission electron microscopy tomography to correlate copper catalyst particle morphology with carbon fiber morphology**. *Carbon* 2011, **49**(9):2950-2959.
2. Shaikjee A, Coville NJ: **Catalyst restructuring studies: The facile synthesis of tripod-like carbon fibers by the decomposition of trichloroethylene**. *Materials Letters* 2012, **68**(0):273-276.
3. Reid RC, Prausnitz JM, Poling BE: **The properties of gases and liquids**. 1987.
4. Jian X, Jiang M, Zhou Z, Yang M, Lu J, Hu S, Wang Y, Hui D: **Preparation of high purity helical carbon nanofibers by the catalytic decomposition of acetylene and their growth mechanism**. *Carbon* 2010, **48**(15):4535-4541.
5. Jian X, Jiang M, Zhou Z, Zeng Q, Lu J, Wang D, Zhu J, Gou J, Wang Y, Hui D: **Gas-Induced Formation of Cu Nanoparticle as Catalyst for High-Purity Straight and Helical Carbon Nanofibers**. *Acs Nano* 2012, **6**(10):8611-8619.
6. Qin Y, Jiang X, Cui Z: **Low-temperature synthesis of amorphous carbon nanocoils via acetylene coupling on copper nanocrystal surfaces at 468 K:**

a reaction mechanism analysis. *The Journal of Physical Chemistry B* 2005, **109**(46):21749-21754.

7. Du F, Liu J, Guo Z: **Shape controlled synthesis of Cu< sub> 2</sub> O and its catalytic application to synthesize amorphous carbon nanofibers**. *Materials Research Bulletin* 2009, **44**(1):25-29.
8. Phillips DH: **Polycyclic aromatic hydrocarbons in the diet**. *Mutation Research/Genetic Toxicology and Environmental Mutagenesis* 1999, **443**(1–2):139-147.
9. Nakanishi K: **Infrared Absorption Spectroscopy, Nankodo Co**. *Ltd, Tokyo* 1962:38.

4.3 Studies on the effect of annealing the CNFs

4.3.1 Introduction

It has been noted that the synthesis of carbon nanofibers using a copper catalysts at low temperatures generates carbons that are amorphous **[1, 2**]. The amorphous nature of the material would however render the carbon materials impractical for many applications that require a substantial amount of order in the fiber axis. High temperature treatment of carbon materials in an inert atmosphere has been instrumental in increasing the graphitization of carbon **[3, 4].** In their review Ramos et al. give a detailed analysis of how the properties of carbon nanomaterials vary with the annealing process. Techniques varying from Raman spectroscopy to BET surface area analysis can be used to determine the robustness of the carbon material attained after annealing **[3]**. The effect of annealing amorphous carbon on field emission properties of carbon have been documented **[4]**. The authors observed that annealing induced conversion of sp^3 carbon to sp^2 carbon. By using Raman spectroscopy they showed (in Figure 4.23) that annealing increased the sp^2 crystal domains sizes (L_a) and that with the I_D/I_G ratio varied when the transition from amorphous carbon to nanocrystalline graphite occurred **[4]**.

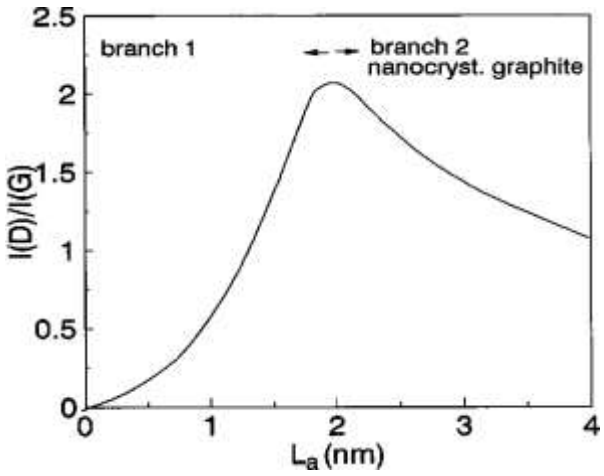


Figure 4. 23: Relationship between Raman I_D/I_G and the correlation length (La) of sp^2 clusters **[4]**

4.3.2 Experimental

In these studies, as synthesised carbon nanofibers (both the straight and helical) were annealed inside the same CVD set up (Figure 4.24) that was used to grow the carbon materials. The annealing was performed in an inert atmosphere using nitrogen at a flow rate of 50 $ml.min^{-1}$. After annealing, the carbon nanomaterials were then subjected to Soxhlet extraction using toluene at 140 ℃ until all the polycyclic aromatic hydrocarbons (PAHs) were removed (approximately 2 hours). Characterization techniques employed were FTIR spectroscopy, BET surface area analysis, Raman spectroscopy, X-ray diffraction and transmission electron microscopy.

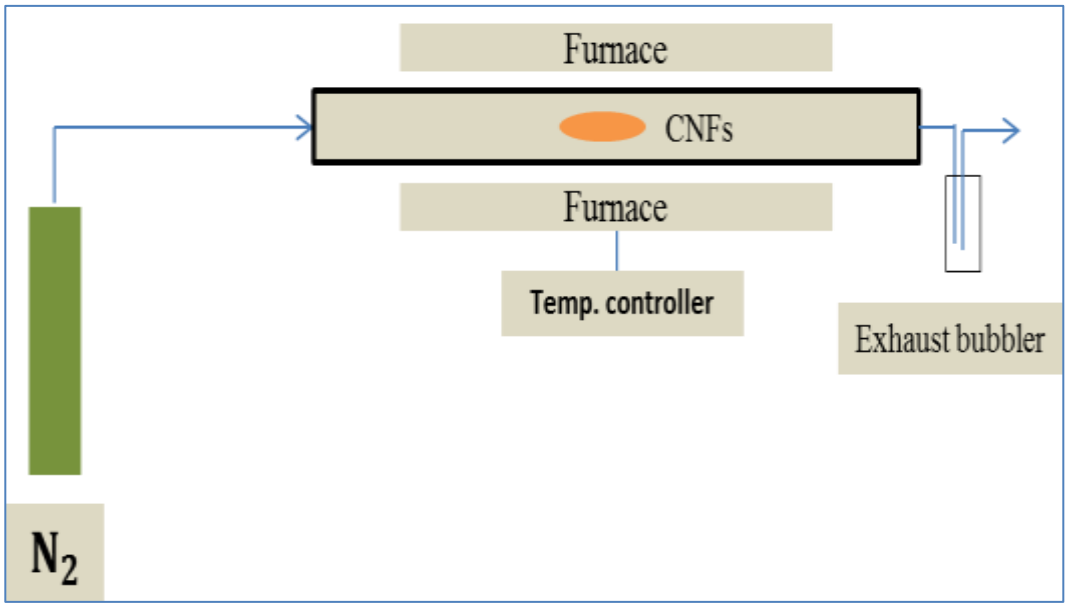


Figure 4. 24: CVD set-up used for annealing the CNFs

4.3.3 FTIR spectroscopy of the CNFs annealed at different temperatures

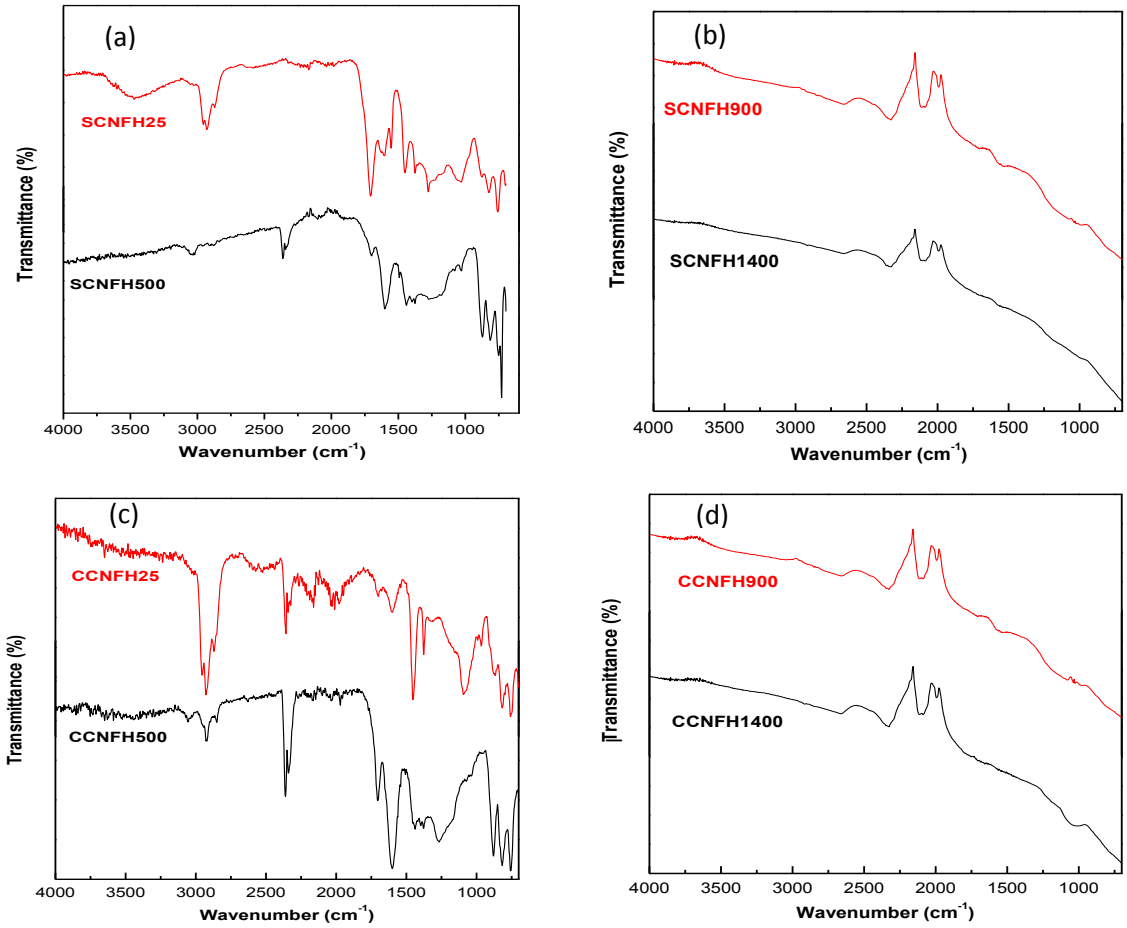


Figure 4. 25: FTIR spectra of the annealed carbon nanofibers SCNF post heated at 25 and 500 ℃ (a), 900 and 1400 (b). CCNF post heated at 25 and 500 ℃ (c), 900 and 1400 (d).

FTIR spectra analysis shown in Figure 4.25 was used to qualitatively study the surface composition of the annealed carbon nanofibers. The as synthesised carbon materials (S/CCNFH25) in Figure 4.25(a) and (c), displayed surface functional groups that can be associated with tetrahedral carbon in the CNFs. The most prominent peaks occur at 2950 cm^{-1} (which can be associated with sp^3 C-H stretching/vibrational modes of alkyl groups ($-CH_3$)) and 1705 cm^{-1} (assigned to a carbonyl (C=O) group). This carbonyl group has been attributed to post synthesis

oxidation of the CNFs when they are removed from the reactor setup **[1]** and during Soxhlet extraction**.** The band at 1602 cm^{-1} is assigned to the C=C vibrations of the aromatic groups and the peak at 1450 cm^{-1} is then ascribed to C-H band vibrations of a methylene group ($-CH_2$) **[5, 6]**. It is clear from the FTIR spectra that the as synthesised carbon nanofibers have a high content of hydrogen atoms compared to carbon nanofibers synthesised at higher temperatures **[7]**. There is a significant change in the surface functional groups of the carbon nanofibers when the material is annealed at higher temperatures in an inert atmosphere. A gradual loss of the hydrogen atoms is observed (rationalized in Figure 4.26) as noted in the IR spectrum of the S/CCNFs annealed at 500 ℃ as seen in Figure 4.25 (a) and (c). It is also observed that alkyl groups on the carbon nanofibers are removed as seen from the residual peaks at 3020 and 1602 cm^{-1} corresponding to H-C and C=C vibrational bonds of aromatic groups on the CNFs. Annealing the carbon nanofibers at higher temperatures (i.e. 900 and 1400 ℃) results in the effusion of all the hydrogen atoms and in a complete rehybridization of the carbon atoms to sp^2 carbon. We observe this effect in the two FTIR spectra of (S/CCNFH900 and S/CCNFH1400 (Figure 4.25 (b) and (d)) which display patterns that parallel the IR spectrum of graphite (material composed entirely of sp^2 carbon).

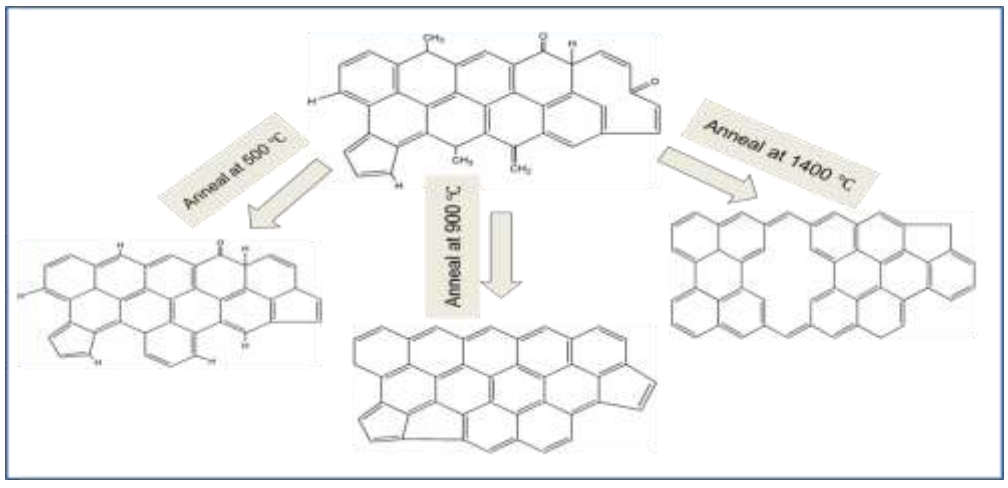


Figure 4. 26: Schematic displaying structural evolution of CNFs with annealing temperature

4.3.4 Raman data of the annealed CNFs

Raman spectroscopy using laser radiation in the visible region (514 nm) was used to probe the degree of graphitization of the carbon nanofibers in response to the annealing temperature. Carbon peaks mostly observed in the Raman spectra are the D and G bands associated with the sp^2 hybridized carbon breathing modes. The ratio of the D to G band intensities is frequently used to elucidate the amount of disorder or order in the carbon materials provided the carbon materials contain only sp^2 carbon **[8-10]**. A third peak can be observed on a Raman spectrum called the T peak in the carbon material that is being analysed has a high content of sp^3 hybridized carbon. The degree of graphitization of the carbon material is thus deduced from the I_D/I_G ratio and the presence of the T peak on the Raman spectrum **[11]**. From the Raman measurements shown in Figure 4.27 (a) and (b), the as synthesised carbon nanofibers are not Raman active and can only fluoresce under the laser radiation. This carbon material is highly amorphous and has a high amount of functional groups. Annealing of the carbon material does add some stability to the carbon structure since there is an appearance of the D and G bands for the material annealed at 500 ℃ and above. Raman spectra of S/CCNFH500 (CNFs annealed at 500℃) shows a low I_D/I_G ratio (≈ 0.6). However the D peak is very broad and upon de-convolution (Figure 4.27(d)), of the spectrum we get a third peak which can be attributed to the carbon sp^3 content of the CNFs. This is supported by the presence of a peak at 3000 cm^{-1} in Figure 4.27(c). The high I_G/I_D ratio of the carbon material annealed at 500 ℃ is partly explained as a result of the laser beam heating the carbon material during the sampling of the spectrum. This effect occurred even when using very low power intensity. Carbon nanofibers annealed at 900 and 1400 ℃ are composed entirely of sp^2 hybridized carbon show that the carbon materials have attained some degree of order with the I_D/I_G of approximately one. The narrowing of the D peak area also affirms the increase in the structural uniformity of the carbon nanofibers. An increase of the I_D/I_G ratio with the annealing temperature is noted in Table 4.9, and arises due to an increase in the cluster size ”L_a”(i.e. crystallite size) of an annealed polymeric

carbon. Hence the transition from amorphous polymeric carbon to nanocrystalline graphite show that the Raman intensity I_D/I_G, is proportional to the crystallite size ($\mathbf{L_a \propto I_D/I_G}$) **[4]**. The dispersion of FWHM for the D peak is large in all the three samples, this is because the annealed carbon nanofibers do not form perfectly ordered long range graphitic planes in the material which is due to the introduction of (C_4,C_5,C_8, etc.) into the lattice structure.

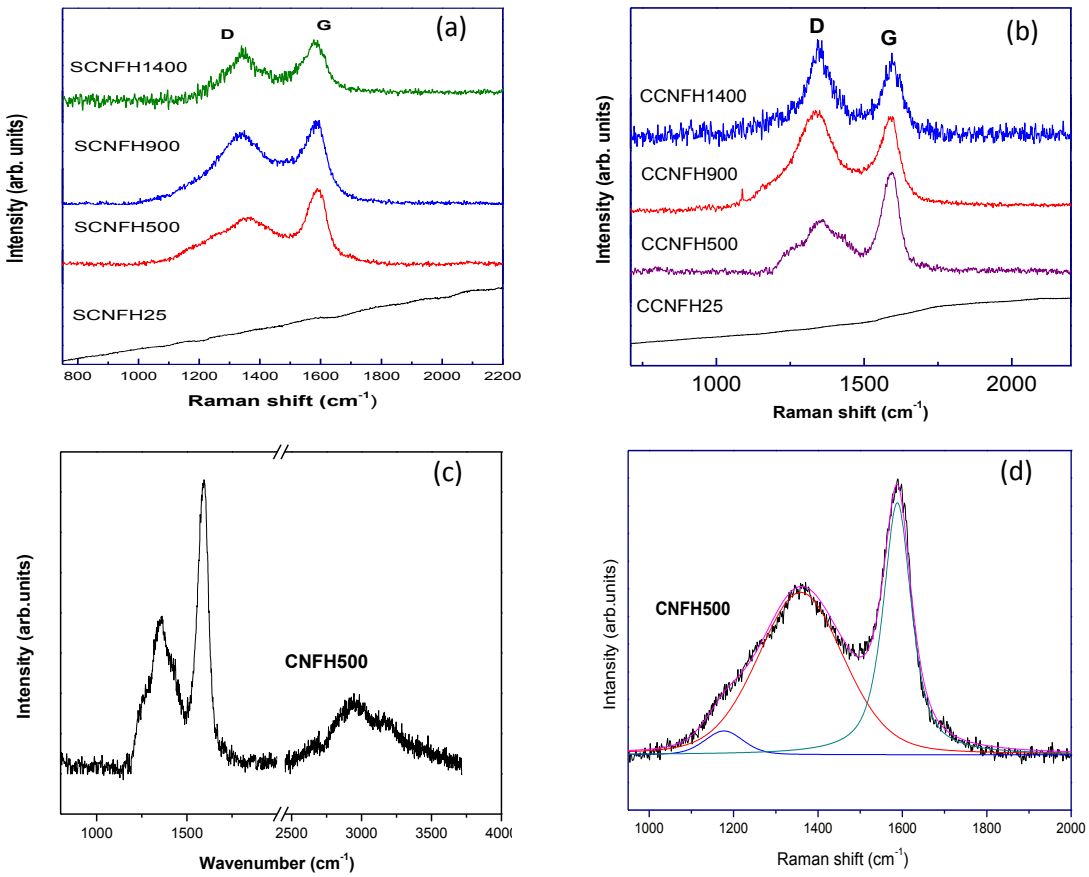


Figure 4. 27: Raman spectra of the carbon nanofibers, straight fibers (a), helical fibers (b), Typical spectrum of fibers annealed at 500 ℃ (c) and deconvoluted (using pseudo-Voigt function) Raman spectrum of CNFs annealed at 500 ℃ (d).

Table 4. 9: Raman D and G band peak position, intensity and area ratios of the CNFs

Sample name	D band peak position (cm^{-1})	G band peak position (cm^{-1})	I_D/I_G ratio	A_D/A_G ratio
SCNFH500	1360	1588	0.64	1.60
SCNFH900	1343	1590	0.88	1.54
SCNFH1400	1445	1586	0.95	1.42
CCNFH500	1354	1590	0.54	1.04
CCNFH900	1349	1590	1.05	1.46
CCNFH1400	1342	1594	1.12	1.39

4.3.5 Nitrogen adsorption-desorption results (BET)

Surface areas (Figure 4.28 and 4.29) of the carbon nanofibers were found to increase relative to the as synthesised CNFs with annealing temperature up to 900 ℃. A sharp decrease of the surface occurred when the annealing temperature is raised to 1400 ℃. This increased effect is rationalized by the opening of micropores which increases the pore volume of the material as the carbon material evolves from having a high sp^3 carbon to a more ordered carbon structure with sp^2 hybridization. The very low surface area carbon annealed at 1400 ℃ is attributed to the collapse of the porous nature of the materials at this annealing temperature. From the BET results we observe that the carbon nanofibers annealed at 500 ℃ and 900 ℃ are mesoporous with high surface areas and pore volumes.

Table 4. 10: Surface area of the annealed SCNFs (straight carbon nanofibers)

sample	Pore volume (cm^3/g)	BET surface area (m^2/g)	pore diameter (nm)
SCNFH25	0.1538	135	4.87
SCNFH500	0.1762	272	2.83
SCNFH900	0.1193	185	2.89
SCNFH1400	0.0796	39	8.05

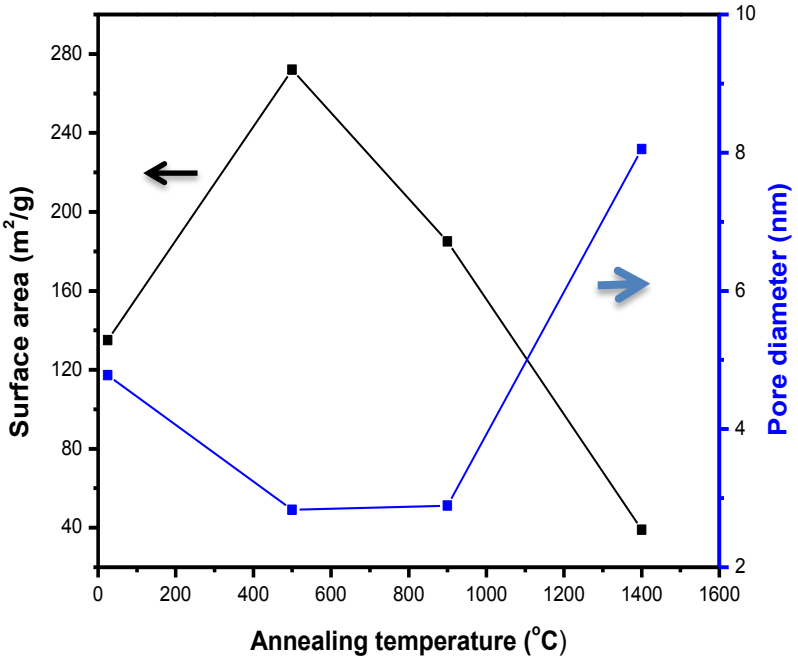


Figure 4. 28: Variation of surface area and pore diameter with temperature

Table 4. 11: Surface area of the annealed CCNFs (coiled carbon nanofibers)

sample	Pore volume (cm^3/g)	BET surface area (m^2/g)	pore diameter (nm)
CCNFH25	0.1632	171	3.86
CCNFH500	0.1966	255	3.37
CCNFH900	0.2618	364	2.57
CCNFH1400	0.1447	47	12.14

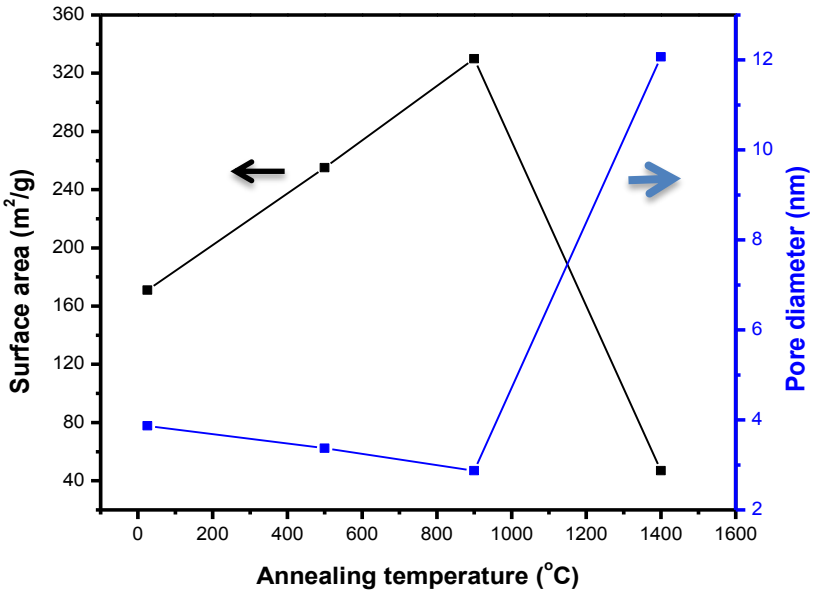
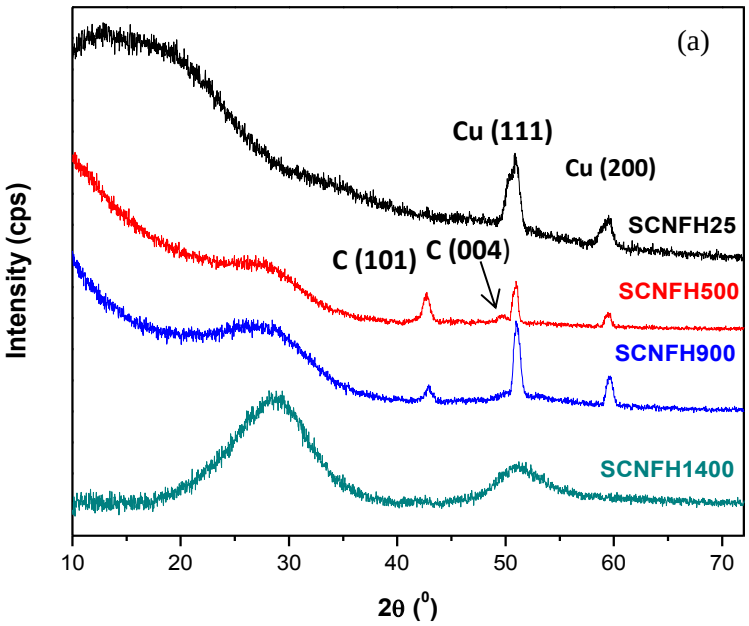


Figure 4. 29: Variation of surface area and pore diameter with temperature

4.3.6 XRD analysis

The X-ray diffraction patterns in Figure 4.30(a) and (b) of the annealed carbon nanofibers show that the carbon nanofibers did not attain complete crystallization even at the high temperature annealing temperature of 1400 ℃. It is however very clear that a structural evolution of the material occurs with the annealing temperature.

The as synthesised carbon shows more scattering with a broad hump at the low Bragg angle. This confirms that the as synthesised carbon is amorphous, as observed from FTIR spectroscopy. It is also noted that the carbon annealed at 500 and 900 ℃ displays almost similar diffraction patterns which show that the structural order in the two materials is more or less the same. For this reason their XRD patterns explain why the two materials have similar porosity (both mesoporous as shown by the BET results (Figure 4.28 and 4.29). The carbon (101) diffraction peak is observed only for the carbon nanofibers annealed at 500 and 900℃. However the (101) diffraction peak disappears in the fibers annealed at 1400 ℃, This is due to the destruction of the fibre structure (i.e. the graphitic planes) due to thermal expansion of the amorphous fibers. It is also noted that the carbon annealed at 1400 ℃, although not fully graphitized, there shows increase in the structural ordering (as compared to carbon annealed at 500 and 900℃). A clear and broad distinct peak at 25^{o} Bragg angle is seen, The peak is broad because the material is not highly crystalline to reflect the graphitic nature of carbon nanotubes (or other graphitic materials).No copper metal peaks are observed for the carbon annealed at 1400 ℃. The copper was removed by sublimation during the heating process (i.e. melting point of copper 1083 ℃ **[12]**).



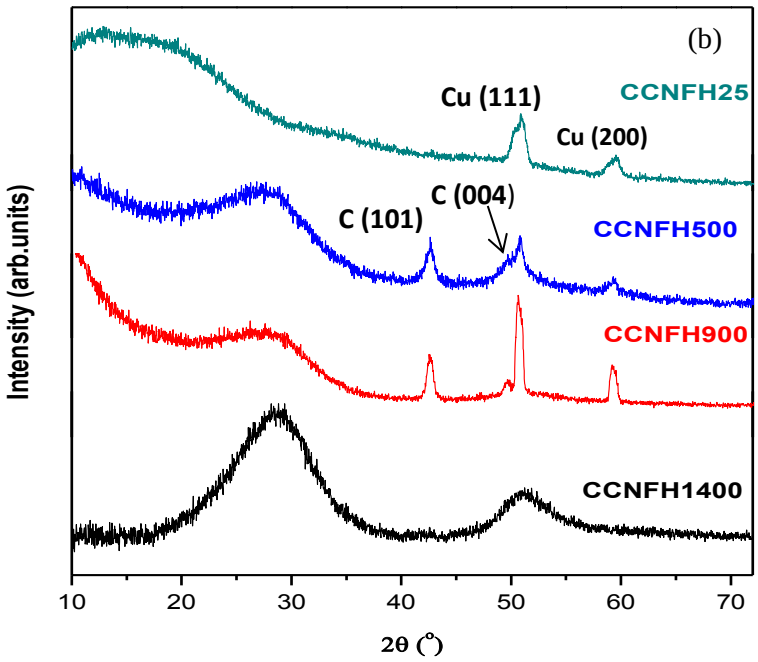


Figure 4. 30: XRD patterns of thermally treated carbon nanofibers, straight CNFs (a) and helical CNFs (b).

To rationalize this non graphitization as observed in the XRD patterns we have to take into account that the CNFs are very amorphous. They have a high content of sp^3 hybridized carbon and many structural defects. It is then suggested that although annealing of the material at these temperatures (500, 900 and 1400℃) does heal the defects in the carbon nanofibers it does not introduce C6 rings into the carbon structure. The material will still have many topological defects such as C5 and C8 carbon rings (Figure 4.31). Therefore we can deduce that since a perfect graphitic crystal (high content of C6 rings) is not attained by annealing, the diffraction patterns will resemble the ones obtained in this study.

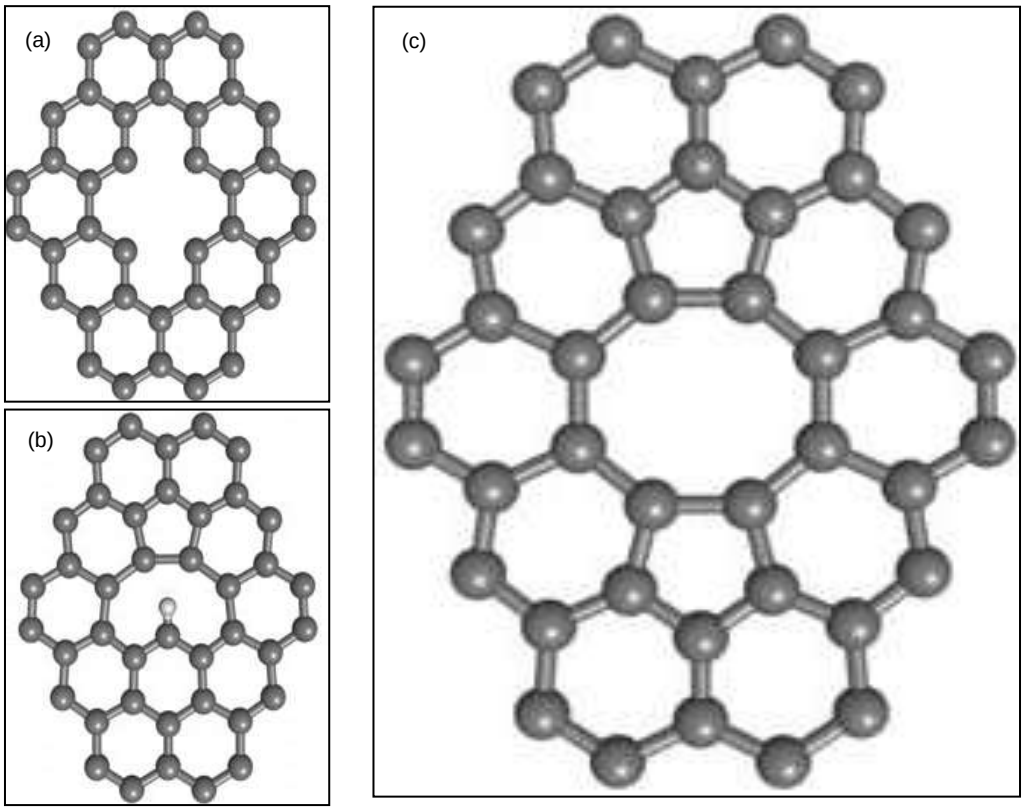


Figure 4. 31: possible defects and vacancies on the as synthesised CNFs (CCNFH25) (a-b), defects present after annealing (C4, C5 or C8 rings).

4.3.7 CNF mass loss during the annealing process

Annealing the carbon materials also induces significant mass loss due to the removal of the volatile materials and less robust carbon materials on the fibers. The mass loss increases with the annealing temperature from 500-1400 ℃, the greatest mass loss occurs when annealing the as synthesised carbon nanofibers at 500 ℃ (Table 4.12).

Table 4. 12: Percentage mass loss during the annealing steps

Sample	Annealing temperature (℃)	Mass lost (%)[a]
SCNFH500	500	46
SCNFH900	900	51
SCNFH1400	1400	52
SCNFH500	500	47
SCNFH900	900	51
SCNFH1400	1400	52

a = % mass loss = $\left(\frac{m_i - m_f}{m_i}\right) \times 100$, m_i – initial mass and m_f – final mass after annealing.

The mass loss between 900 and 1400 ℃ is higher almost equal, however the loss is only a few percentages higher than the mass loss at 500 ℃. This is due to the fact that most of the volatile loosely bound compounds get removed at the annealing temperature of 500 ℃.

4.3.8 TEM images of the annealed carbon nanofibers

Transmission electron microscopy analysis of the annealed carbon nanofibers indicates a different thermal response based on their different morphologies. Straight carbon nanofibers do not undergo any morphological change at the different annealing temperatures. The TEM images display that all the straight fibers remain straight and we do not observe any breakage of the carbon materials (Figure 4.32). Helical carbon nanofibers however break into shorter fibers at high annealing temperatures as shown in Figure 4.33, it is therefore suggested that breakages are due to thermal expansion of the carbon material during the annealing process. Breakages

most probably occur at the helical carbon nanofiber nodes possibly because of a high concentration of defects at these sites.

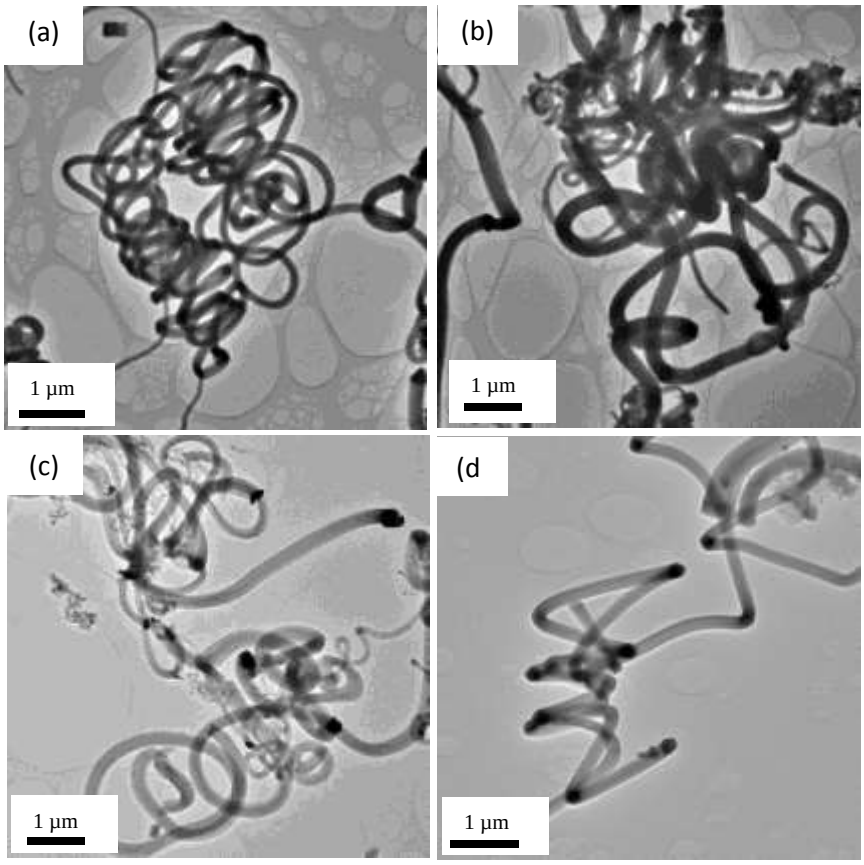


Figure 4. 32: TEM images of the straight annealed at different temperatures 25 ℃ (a), 500 ℃ (b), 900 ℃ (c) and 1400 ℃ (d).

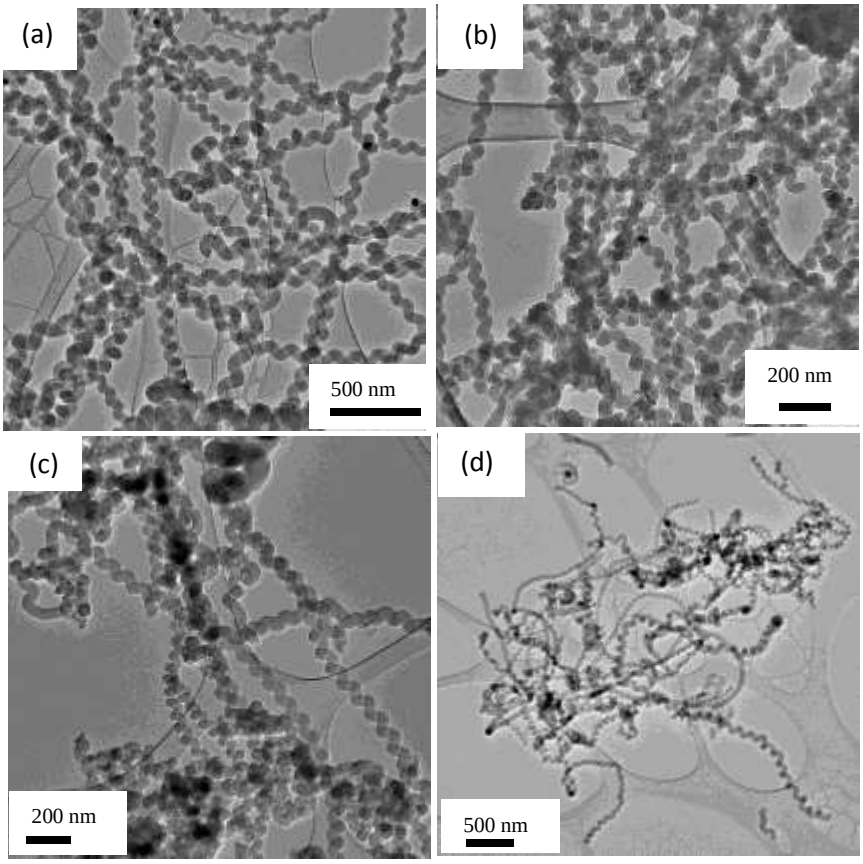


Figure 4. 33: TEM images of the straight annealed at different temperatures 25 ℃ (a), 500 ℃ (b), 900 ℃ (c) and 1400 ℃ (d).

The lengths of the broken fibers varied greatly because the breakages did not occur at specific points since the breaking points (which are the helical nodes) were evenly distributed on helical fiber axis.

4.3.9 Concluding remarks

CNF_s grown at low temperature are amorphous without any structural order. Annealing of the CNFs induces a sequential conversion of the carbon atoms from sp^3 to sp^2 carbon and this improves the fiber stability. It was observed that the conversion is a stepwise process and depends on the annealing temperature. The CNFs are still highly defective even after annealing at high temperature (1400 ℃) indicating that the

amorphous polymeric CNFs cannot attain highly graphitized texture because of the presence of topological defects in the fiber structure. It has been suggested that the growth mechanism of these CNFs is a polymerization process involving only the surface interaction of carbon and the hydrogen with the catalyst template. This VSS mechanism can be extended further to explain why the CNF synthesised at high temperature (> 500 ℃) are graphitic, which is due to the self-healing ability of the catalysts to remove defects on the growing graphitic planes. This can then explain why post heating of polymeric amorphous CNFs does not yield a graphitized structure because the graphitic order has to be induced during the growth of the carbons by the catalyst.

4.3.10 References

1. Du F, Liu J, Guo Z: **Shape controlled synthesis of Cu< sub> 2</sub> O and its catalytic application to synthesize amorphous carbon nanofibers**. *Materials Research Bulletin* 2009, **44**(1):25-29.
2. Qin Y, Yu L, Wang Y, Li G, Cui Z: **Amorphous helical carbon nanofibers synthesized at low temperature and their elasticity and processablity**. *Solid state communications* 2006, **138**(1):5-8.
3. Ramos A, Cameán I, García AB: **Graphitization thermal treatment of carbon nanofibers**. *Carbon* 2013 (in press).
4. Ilie A, Ferrari A, Yagi T, Robertson J: **Effect of sp^2 -phase nanostructure on field emission from amorphous carbons**. *Applied Physics Letters* 2000, **76**(18):2627-2629.
5. Qin Y, Jiang X, Cui Z: **Low-temperature synthesis of amorphous carbon nanocoils via acetylene coupling on copper nanocrystal surfaces at 468 K: a reaction mechanism analysis**. *The Journal of Physical Chemistry B* 2005, **109**(46):21749-21754.

6. Jian X, Jiang M, Zhou Z, Yang M, Lu J, Hu S, Wang Y, Hui D: **Preparation of high purity helical carbon nanofibers by the catalytic decomposition of acetylene and their growth mechanism**. *Carbon* 2010, **48**(15):4535-4541.
7. Borowiak-Palen E, Steplewska A, Rümmeli MH: **On the use of Cu catalysts for tailoring carbon nanostructures in alcohol-CVD**. *physica status solidi (b)* 2009, **246**(11-12):2448-2452.
8. Ferrari A, Robertson J: **Resonant Raman spectroscopy of disordered, amorphous, and diamondlike carbon**. *Physical Review B* 2001, **64**(7):075414.
9. Dresselhaus MS, Dresselhaus G, Saito R, Jorio A: **Raman spectroscopy of carbon nanotubes**. *Physics Reports* 2005, **409**(2):47-99.
10. Ferrari A, Robertson J: **Interpretation of Raman spectra of disordered and amorphous carbon**. *Physical Review B* 2000, **61**(20):14095.
11. Gilkes K, Sands H, Batchelder D, Robertson J, Milne W: **Direct observation of sp^3 bonding in tetrahedral amorphous carbon using ultraviolet Raman spectroscopy**. *Applied Physics Letters* 1997, **70**(15):1980-1982.
12. Cahill J, Kirshenbaum A: **the density of liquid copper from its melting point (1356° k.) To 2500° k. And an estimate of its critical constants1, 2**. *The Journal of Physical Chemistry* 1962, **66**(6):1080-1082.

4.4 Functionalization of the carbon nanofibers

4.4.1 Introduction

Carbon nanomaterials are known to be inert in nature, Therefore their functionalization is a very important step to increase the number of binding sites on the surface of the carbon nanomaterials and allow their good dispersion in solvents **[1]**. Functionalization of carbon nanomaterials can be performed in solution or solvent free environments **[2, 3]**. Acid solutions (nitric, sulphuric and hydrochloric acids) are the most commonly employed chemicals for the functionalizing of carbon nanomaterials and introducing oxygen functionalities, because they have been found to be the most efficient in introducing functional groups on the carbon nanomaterial surface **[1, 4]**. In this section the synthesized and annealed carbon nanofibers were functionalized using nitric acid and sulphuric acid. The functionalization technique is employed oxygen groups (C=O, C-O-C, OH, etc) on the surface of the carbon nanomaterials, thus improving their ability of interact with metal ions **[5]**.

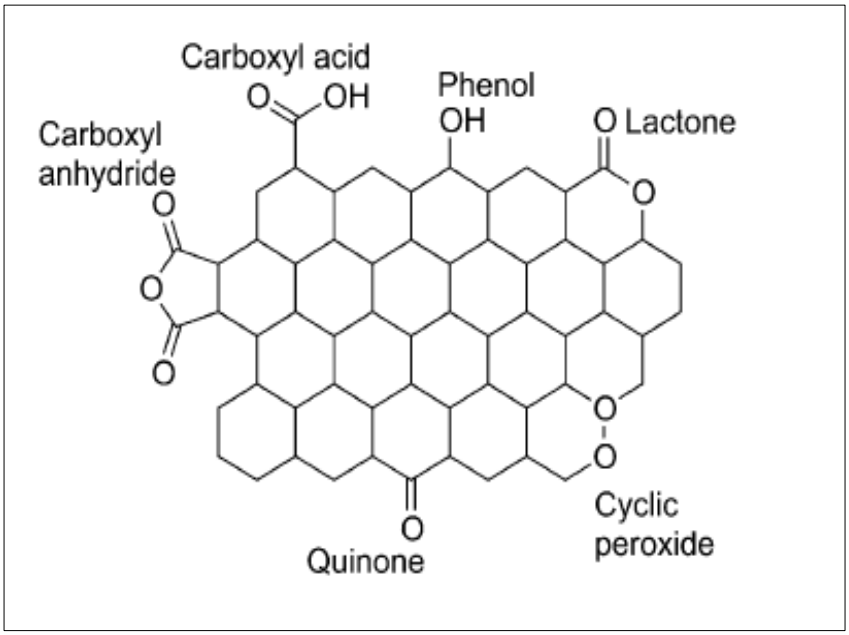


Figure 4. 34: Possible functional groups on the CNFs after functionalization **[5, 6]**

4.4.2 Experimental

A functionalization technique was performed as follows: a given amount of raw carbon nanofibers (mass ~1-2 g) were dispersed in 100 ml of an acid solution (i.e. 55% HNO_3, 35% HNO_3 and 46% H_2SO_4) in a 250 mL round bottomed flask. The solution was then ultrasonicated for 10 minutes at room temperature. The mixture was then refluxed at the chosen temperature (80 or 85 ℃) for a significant amount of time (2 or 4 hours) on a magnetic stirrer. After the oxidation procedure the fibers were then washed with large quantities of deionized water (~ 4 L) to remove all the acid and the copper ions that were formed from the copper metal embedded on the fibers, the final pH of the washed fibers was approximately 7.

4.4.3 Results and discussion

The CNFs were named:

- **CNFH 25 F80**: CNF annealed at 25 ℃, funtionalised using 55% HNO_3 at 80 ℃ for 2 hours.
- **CNFH 500 F80**: CNF annealed at 500 ℃, funtionalised using 55% HNO_3 at 80 ℃ for 2 hours.
- **CNFH 900 F80**: CNF annealed at 900 ℃, funtionalised using 55% HNO_3 at 80 ℃ for 2 hours.
- **CNFH 1400 F80**: CNF annealed at 1400 ℃, funtionalised using 55% HNO_3 at 80 ℃ for 2 hours.

4.4.3.1 BET surface area

It was observed that functionalization of the materials using mild conditions (i.e. at 80 ℃, 2 hours using 55% HNO_3) resulted in a decrease in the material pore volume. As a consequence the BET surface area underwent a dramatic drop (Table 4.13) compared with the annealed unfuntionalised/unoxidised carbon nanofibers (i.e. from 272 to 15 m^2/g for carbon materials annealed at 500 ℃). The pore size distribution of

the oxidized carbon nanofibers range changed from 4-50 nm. The pores are removed on functionalization, the blockages therefore leave only the large voids which adsorb a small amount of the adsorbate gas (in this case N_2) thus accounting for the low surface area **[7]**. It is also possible that the pore closure is attributed to the introduction of surface functional groups that did not penetrate into the integral fiber structure. Therefore the functional groups were introduced mostly on the carbon nanofiber surface resulting in coverage of the fiber which prevented optimum adsorption of the nitrogen gas, hence yielding the low carbon surface area.

Table 4. 13: BET results of functionalized CNFs at 80 ℃ using 55 % nitric acid.

Sample name	Surface area (m^2/g)	Pore volume (cm^3/g)	Pore diameter (nm)
CNFH 25 F80	17	0.084	28.2
CNFH 500 F80	15	0.076	40.2
CNFH 900 F80	63	0.071	4.5
CNFH 1400 F80	58	0.105	7.2

4.4.3.2 Infrared spectroscopy of the CNFs

Infrared spectroscopy was employed to determine the types of functional groups introduced on the fiber materials after oxidization. It is known that functionalization of carbon nanomaterials in acidic solution introduces oxygen onto the carbon material **[1]**. Carbon nanomaterials that were composed of a substantial amount of sp^3 carbon and alkyl groups (CNFH 25 and CNFH 500 (Figure 4.34 (b)) were easily oxidized. IR

spectra of CNFH 25 F80 and CNFH 500 F80 **(**Figure 4.34(a)) revealed that oxidation of the material removes the alkyl C-H vibration at 2950 cm^{-1}. As the alkyl (C-H) and other sp^3 hybridized carbons groups are lost, peaks due to carbonyl groups (C=O) at 1720 cm^{-1} and carbon-carbon (C-C) groups of polyaromatic -C=C- groups at 1581 cm^{-1} are formed. The peak at 1348 cm^{-1} is assigned to the (C-O-C) of the lactone groups . The carbon materials annealed at 900 and 1400 ℃, that contain only sp^2 hybridized carbon do not show a big change in their surface functional groups other than showing small vibrational peaks at wavenumber 1720 and 1580 cm^{-1} **[8, 9]**. The lack of a significant amount of functional groups on the carbon nanofibers containing only sp^2 carbon is expected because of the robustness **[1]** of the materials.

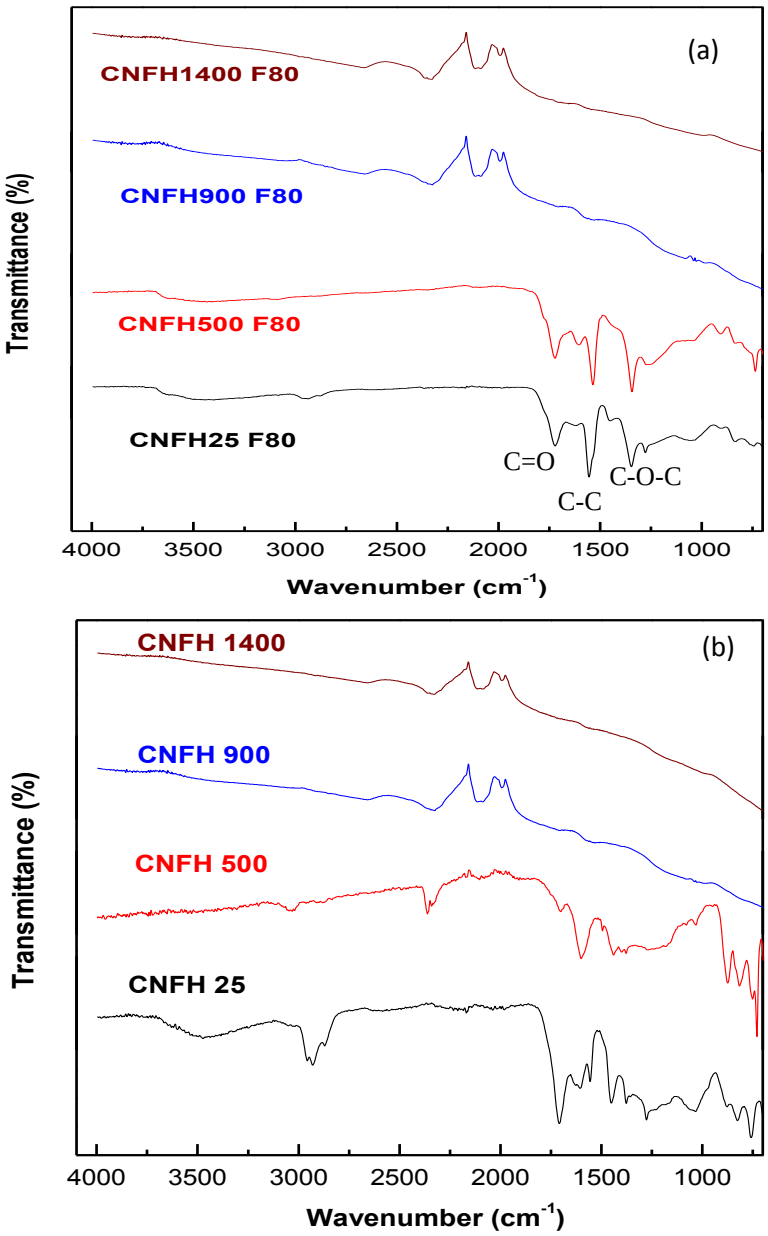


Figure 4. 35: IR spectra of the (a) CNFs functionalized at 80 ℃ using 55 % nitric acid and (b) Unfunctionalized CNFs.

4.4.3.2 TEM analysis of the carbon nanofibers (CNFs)

TEM imaging was employed to analyze the morphology of the carbon nanofibers after functionalization. The images shown in Figure 4.35(a-d)) demonstrate that there was no change in the fiber structure after the oxidation, apart from the removal of the copper nanoparticles embedded in the fibers and some surface roughening (Figure 4.35(e-f)) of the fibers this etching is because of the acidic solution. The morphology of all the fibers (i.e. fibers annealed 25, 500, 900 and 1400 ℃) remains intact because the functionalization process is not severe enough to break the fibers into pieces.

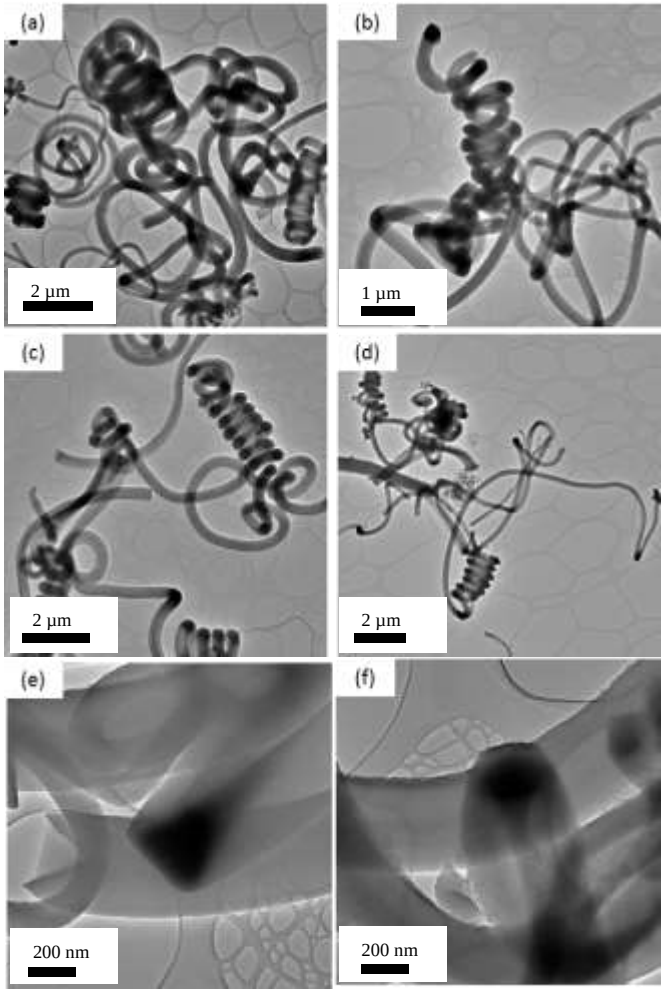


Figure 4.36: TEM images of functionalized CNFs, CNFH25 F80 (a), CNFH500 F80 (b), CNFH900 F80 (c), CNFH1400 F80 (d) and CNFH25 F80 magnified image (e and f).

4.4.3.3 Optimization of the functionalization process.

Because functionalization of the CNFs using 55% HNO_3 reduced the surface of the CNFs to optimize the functionalization process different functionalization processes using different acid solutions were employed on the straight carbon nanofibers annealed at 900 ℃.

Four further functionalization procedures were employed:

The carbon nanofibers were functionalized using 35 % HNO_3 for 2 hours at 80 ℃ (**CNFH900 F80 35%).**

The carbon nanofibers were functionalized using 55 % HNO_3 for 4 hours at 85 ℃ (**CNFH 900 F85 4hrs**).

Carbon nanofibers functionalized using 1:1 (V/V) of 55 % HNO_3 and 50% H_2SO_4 85 ℃ for 2 hours (**CNFH900 NS 4:1**).

Carbon nanofibers functionalized using 4:1 (V/V) of 55 % HNO_3 and 50% H_2SO_4 at 85 ℃ for 2 hours (**CNFH900 NS 1:1**).

4.4.3.3.1 BET surface area

Nitrogen adsorption results using BET technique (Table 4.14) were performed. High surface areas were observed because the functionalization using the strong oxidizing solution not only results in the surface coverage of functional groups on the carbon nanofibers but bulk oxidation also occurs. This opens up the structure of the carbon nanofibers. The wet etching treatment (with stronger acid solutions) therefore creates graphitic defects **[1]** not only on the surface but also opens meso and micropores deep inside the carbon nanofibers. It is observed that functionalization of the carbon nanofibers at mild conditions (i.e. at 80 ℃ using 35 % nitric acid) results in low surface area of the material. The surface area of the carbon nanofibers increases when the functionalization process is severe. This is shown by the high surface area (395

m^2/g) of the fibers functionalized using the 1:1 V/V solution of nitric and sulphuric acid.

Table 4.14: BET surface area and pore structure of the CNFs after functionalizing using the different acid solution.

Sample name	Surface area (m^2/g)	Pore volume (cm^3/g)	Pore diameter (nm)
CNFH900 F80 35%	12	0.021	7.2
CNFH 900 F85 5hrs	162	0.124	3.4
CNFH900 NS 4:1	204	0.131	2.5
CNFH900 NS 1:1	395	0.211	2.08

4.4.3.3.2 Infrared spectroscopy analysis

Optimization of the functionalization process performed on the carbon nanofibers annealed at 900 ℃, was also studied using IR spectroscopy. The severity of the functionalization solution is the parameter that dictates the amount and type of surface functional groups formed on the fibers **[1]**. The two bands at 1722 and 1585 cm^{-1} were used to monitor the degree of functionalization on the carbon nanofiber' structure. The intensity of these peaks increases with the oxidizing strength of the acid solution (Figure 4.36 (a-b)) These results indicate bulk oxidation of the carbon nanofibers. The acid sites increase the propensity of the carbon materials to bind active metal for catalysis reactions **[10]**.

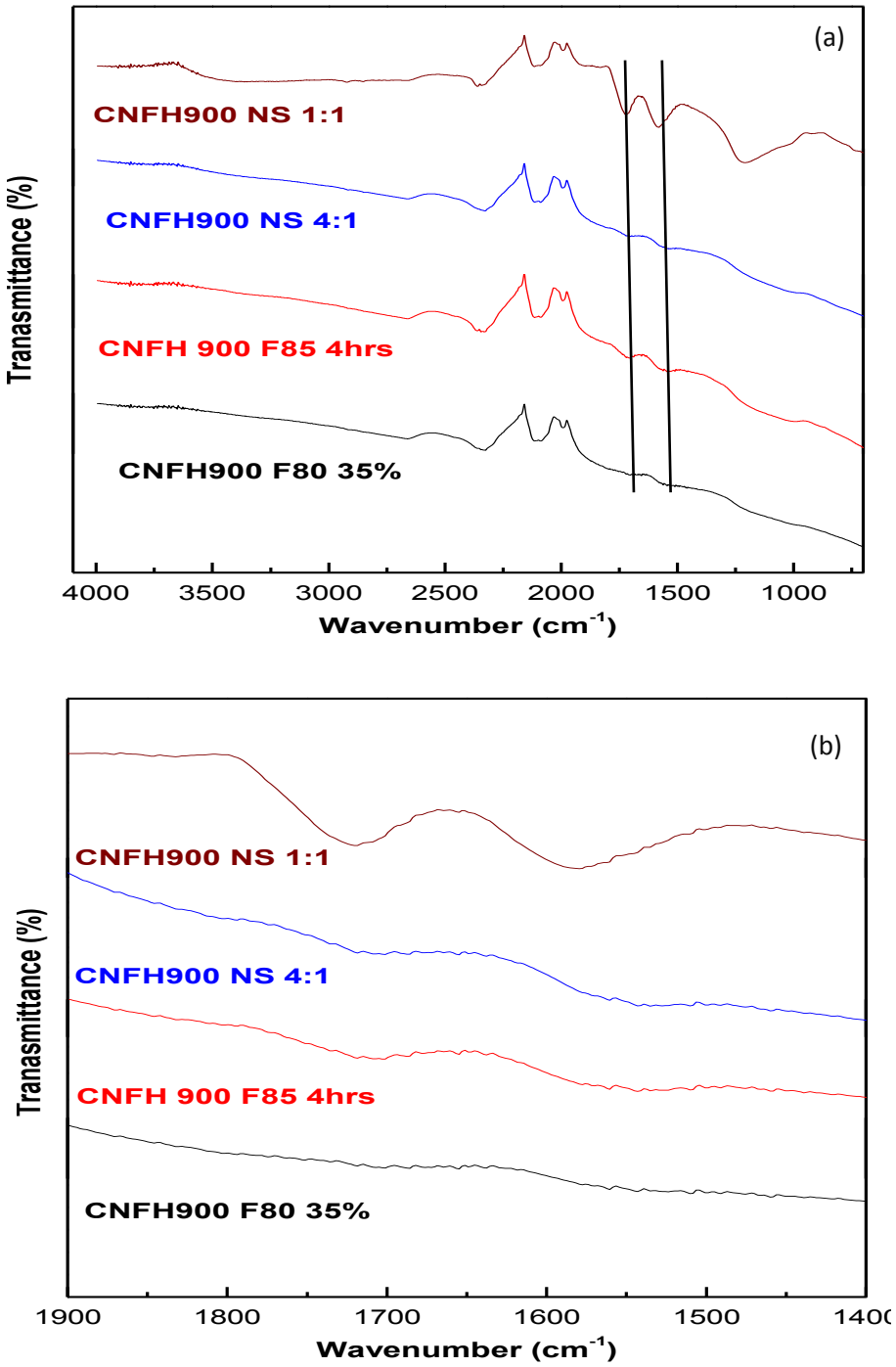


Figure 4. 37: (a) FTIR spectra of functionalized CNFs (optimization process), CNF H 900 and (b) the zoomed portion ranging from 1400-1900 wavenumber.

4.4.3.3.3 TEM analysis of the CNFs for functionalized using different acid solutions.

Functionalization using the less severe acid solutions did not destroy the structural integrity of the carbon nanofibers (Figure 4.37), however employing an oxidizing agent containing high concentration of sulphuric acid (1:1 v/v with HNO_3) results in the breakages of the carbon nanofibers (from lengths of ~ 20 µm to less than 5 µm Figure 4.37(d)) thus suggesting that the acid mixture (1:1 V/V nitric acid and sulphuric) was too severe towards the carbon material structure.

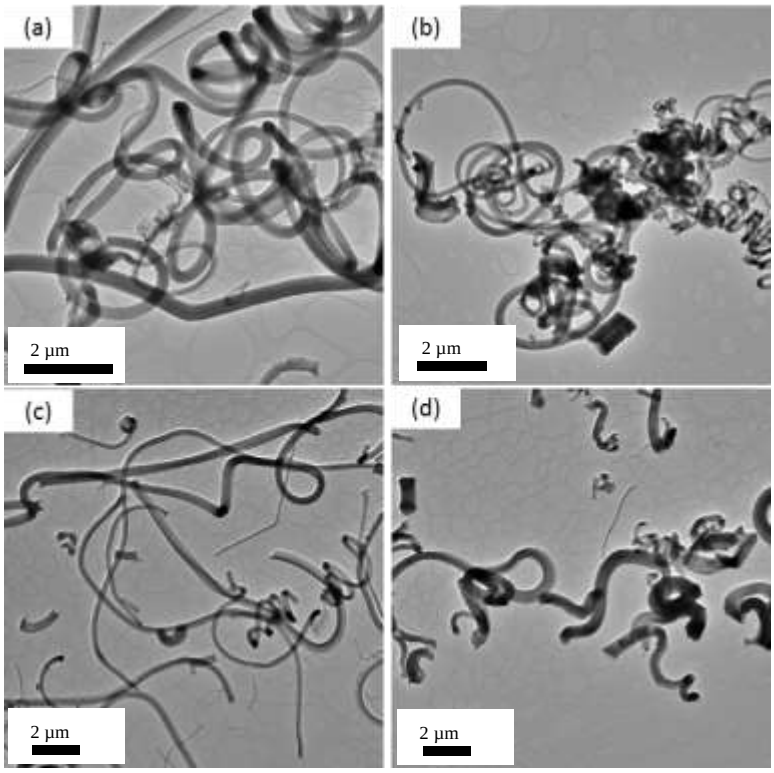


Figure 4.38: TEM images of the CNFs functionalized using different solution, CNFH900 F80 35%) (a), CNFH 900 F85 5hrs (b), CNFH900 NS 4:1 (c) and CNFH900 NS 1:1 (d)

4.4.3.3.4 Raman spectroscopy analysis.

Raman spectroscopy analysis of the functionalized straight CNFs gave spectra (Figure 4.38-39) which are not very different from the spectra of unfunctionalised straight CNFs. The area and intensity ratios of the D and G band are similar to the unfunctionalised CNFs in section were the CNFs were functionalized at 80 ℃ using 55 % HNO_3.

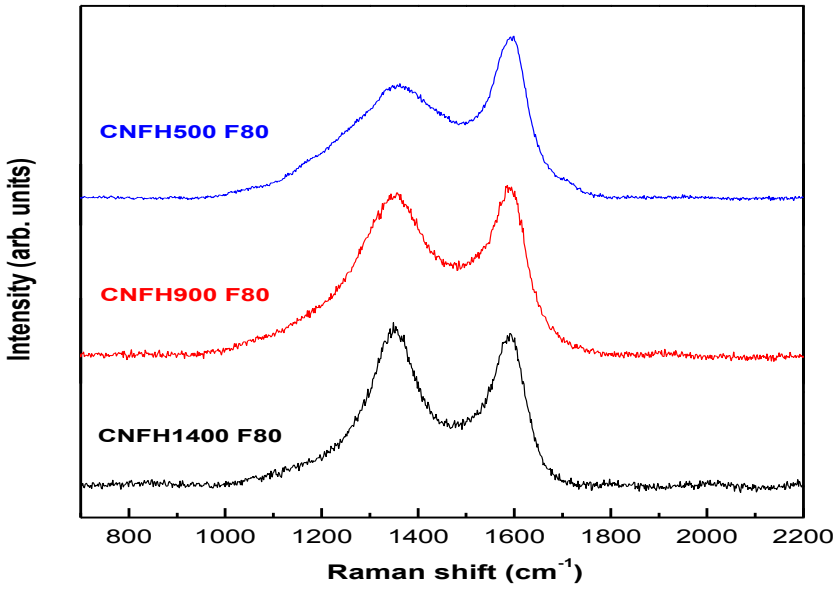


Figure 4. 39: Raman spectra of annealed functionalized CNFs (annealed at 500, 900 and 1400 ℃), Functionalised using HNO_3 at 80 ℃ for 2 hours.

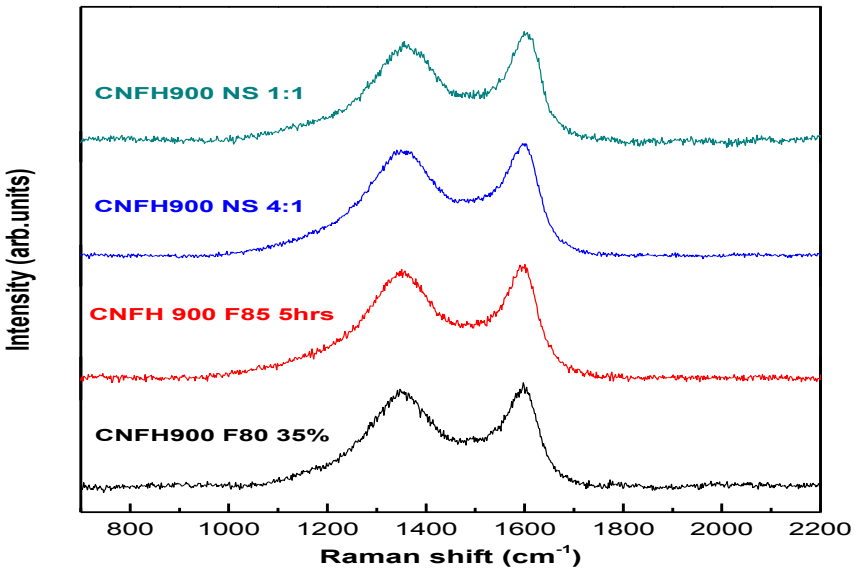


Figure 4. 40: Raman spectra of functionalized CNFs (optimization process) all annealed 900 ℃

Table 4. 15: Raman D and G band peak position, intensity and area ratios of the functionalized CNFs annealed at different temperatures.

Sample name	D band peak Position (cm^{-1})	G band peak position (cm^{-1})	I_D/I_G ratio	A_D/A_G ratio
CNFH500 F80	1363	1599	0.71	1.45
CNFH900 F80	1356	1585	0.96	1.67
CNFH1400 F80	1349	1590	1.07	1.51

Table 4. 16: Raman D and G band peak position, intensity and area ratios of the CNFs all annealed at 900 ℃ for functionalization optimization.

Sample name	D band peak Position (cm^{-1})	G band peak position (cm^{-1})	I_D/I_G ratio	A_D/A_G ratio
CNFH900 F80 35%).	1347	1597	0.91	1.58
CNFH 900 F85 5hrs	1351	1600	0.96	1.79
CNFH900 NS 1:1	1349	1602	0.95	1.55
CNFH900 NS 4:1	1356	1599	0.96	1.64

The Raman spectra therefore indicate that even though the different functionalization solution did affect the structure of the CNFs (see the FTIR, BET and TEM results). The ID/IG values do not reflect changes in a constant way, due to the sp^2/sp^3 as well as the defect in the CNFs. The bond structures and polarity of the carbon atoms on the CNFs are therefore not significantly destroyed by the oxidizing agents. This therefore leaves the amount of sp^2 and sp^3 hybridized carbon atoms in the fiber structure in the same ratio as in the unfunctionalised CNFs resulting in relatively the same Raman spectra.

4.4.4 References

1. Klein KL, Melechko AV, McKnight TE, Retterer ST, Rack PD, Fowlkes JD, Joy DC, Simpson ML: **Surface characterization and functionalization of carbon nanofibers**. *Journal of Applied Physics* 2008, **103**(6):061301-061301-061326.
2. Lakshminarayanan PV, Toghiani H, Pittman Jr CU: **Nitric acid oxidation of vapor grown carbon nanofibers**. *Carbon* 2004, **42**(12):2433-2442.
3. Okpalugo T, Papakonstantinou P, Murphy H, Mclaughlin J, Brown N: **Oxidative functionalization of carbon nanotubes in atmospheric pressure filamentary dielectric barrier discharge (APDBD)**. *Carbon* 2005, **43**(14):2951-2959.
4. Hung NT, Tuong NM, Rakov E: **Acid functionalization of carbon nanofibers**. *Inorganic Materials* 2010, **46**(10):1077-1083.
5. Rodríguez-reinoso F: **The role of carbon materials in heterogeneous catalysis**. *Carbon* 1998, **36**(3):159-175.
6. Sun B, Xu K, Nguyen L, Qiao M, Tao FF: **Preparation and Catalysis of Carbon-Supported Iron Catalysts for Fischer–Tropsch Synthesis**. *ChemCatChem* 2012, **4**(10):1498-1511.
7. Joo Y, Sim J, Jeun Y, Lee SU, Sohn D: **Opening and blocking the inner-pores of halloysite**. *Chemical Communications* 2013.
8. Zhou J-H, Sui Z-J, Zhu J, Li P, Chen D, Dai Y-C, Yuan W-K: **Characterization of surface oxygen complexes on carbon nanofibers by TPD, XPS and FT-IR**. *Carbon* 2007, **45**(4):785-796.
9. Moyo M: **Cobalt and iron supported on carbon spheres catalysts for Fischer Tropsch synthesis**. Faculty of Engineering and the Built Environment, University of the Witwatersrand; 2012.
10. Motchelaho MA, Xiong H, Moyo M, Jewell LL, Coville NJ: **Effect of acid treatment on the surface of multiwalled carbon nanotubes prepared from Fe–Co supported on CaCO< sub> 3</sub>: Correlation with Fischer–**

Tropsch catalyst activity. *Journal of Molecular Catalysis A: Chemical* 2011, **335**(1):189-198.

Chapter 5: Results and discussion: FT studies

5.1 Fischer-Tropsch catalytic studies using the helical and straight CNFs

5.1.1 Introduction

In this chapter application of the carbon nanofibers was evaluated as catalyst supports for Fischer-Tropsch (FT) synthesis. It has to be noted that carbon nanofibers (CNFs) have been used as supports for Fischer Tropsch synthesis before **[1, 2].** The pioneering work by Bezemer et al **[1]** was based on the use of carbon nanofiber supports. In their study they were able to determine the particle size effects on the turn over frequency of the cobalt active phase during the FT reaction. It was observed that TOF decreased from 23 to 1.4×10^{-3} when the metal particle sizes changed from 16-2.6 nm. Bezemer et al **[1]** were able to use the model catalysts based on carbon nanofiber supports to determine the optimum particle size for Fischer-Tropsch synthesis to be between 6-8 nm **[1, 3, 4]**. Diaz et al. **[5]** studied different cobalt catalysts supported on carbon nanofibers grown at 450, 600 and 750 ℃ with different porosities which affected the activity and selectivity of the catalysts. The authors observed that the cobalt catalysts supported on carbon nanofibers prepared at 450 and 600 ℃ had small pore radii (5.52 and 5.77 nm respectively) and showed high activity (with high CH_4 selectivity and high water gas shift activity), while carbon nanofibers grown at 750 ℃ with a lager pore radius (9.46 nm) resulted in high C5+ selectivity but had low overall catalytic activity because of nanoparticles sintering**.**

Most of the reports on application of carbon nanofibers (CNFs) as FT catalyst supports have been based on graphitic type nanofibers. There are no reports on the use of CNFs grown at low temperature. As described in earlier chapters, these are highly amorphous materials and can be structurally modified by annealing. The modified carbon nanofibers both straight and helical nanofibers annealed at 500 and 900 ℃, were studied for application as catalyst supports for a cobalt catalyst.

5.1.2 Experimental

5.1.2.1 Preparation of carbon nanofiber supported Fischer-Tropsch catalysts.

Conventionally FT catalysts are commonly prepared using homogenous deposition precipitation (HDP) and incipient wetness impregnation (IWI) procedures. In this study catalysts were prepared using urea ($CO(NH_2)_2$) and hydrazine (N_2H_4) deposition and simple impregnation procedures.

5.1.2.2 Catalysts preparation by urea deposition (HDP).

The HDP method was performed as follows. $Co(NO_3)_2$.$6H_2O$ (0.988 g) and urea (0.611 g) were added together to give a Co:urea mol ratio of 3:1 in de-ionized water (50 mL). To achieve a cobalt loading of 10%, 2 g of functionalized carbon nanofibers (CNFs) were dispersed in 200 mL deionized water inside a 500 mL round bottomed flask. The cobalt and urea solution was then added dropwise onto the CNF mixture at 90 ℃ while stirring (∼1 h). The sample was then heated to 90 °C for 30 minutes to hydrolyze the urea while under reflux. The sample was then left in the oil bath at 90 °C for 12 h. The solvent was then removed by drying under vacuum at 90 °C using a rotary vapour. The catalyst was dried at 100 ℃ for 12 hours.

5.1.2.3 Catalysts preparation by hydrazine deposition (HDP).

Functionalized carbon nanofibers (2 g) were dispersed in 200 mL ethanol solvent. To this solution a cobalt nitrate in 50 mL ethanol solution ($Co(NO_3)_2$. $6H_2O$, 0.988 g) was added and then the mixture was stirred for 30 minutes. Then a hydrazine solution in ethanol (N_2H_4: Co mol ratio of 90:1) and an ammonia solution (mol ratio of 4:1 to the Co atoms) were simultaneously added dropwise while stirring (Figure 5.1). The solution the stirred for 6 h, filtered and then dried at 100 ℃ for 12 h.

The reaction at ambient temperature was based on this reaction:

$$Co^{2+} + N_2H_4\,(\text{excess}) + 4NH_4OH \rightarrow 2Co^0 + N_2 + H_2O$$

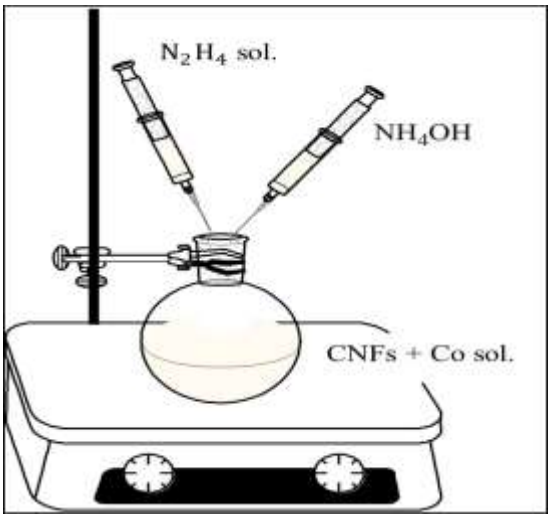


Figure 5. 1: Set up for hydrazine deposition reaction

5.1.2.4 Catalysts prepared by incipient wetness impregnation (IWI).

Co-CNF was prepared by impregnation. An appropriate amount of cobalt precursor ($CoNO_3$. $6H_20$, 0.988 g) solution (5 mL) was slowly impregnated unto 2 g of functionalized carbon nanofibers. The catalyst was then dried at 100 ℃ for 12 hours.

All the catalysts were calcined at 200 ℃ for 3 hours under nitrogen gas.

The catalysts were then characterized and studied for Fischer-Tropsch synthesis using the techniques mentioned in Chapter 3.

5.1.3 Results and discussion

Three catalysts were prepared using the low surface area CNFs (i.e. straight CNFs annealed at 900 ℃ and functionalised using 55% HNO_3 for 2 h) by employing the incipient wetness impregnation, urea HDP and hydrazine deposition methods.The last two catalysts (catalyst number 4 and 5) were prepared using urea HDP on the CNFs with a higher surface area (i.e. SCNFs functionalised using (a) 55% HNO_3 at 85℃ and (b) 4:1 v/v solution of 55% HNO_3 and 46% H_2SO_4 80 ℃)

Catalyst codes are as follows:

1. **10% Co/SCNFH900 F80 2hrs IWI**: Co catalyst supported on CNF functionalized at 80 ℃ for 2 h prepared by IWI
2. **10% Co/SCNFH900 F80 2hrs HDP**: Co catalyst supported on CNF functionalized at 80 ℃ for 2 h prepared by urea HDP
3. **10% Co/SCNFH900 F80 2hrs N_2H_4 HDP**: Co catalyst supported on CNF functionalized at 80 ℃ for 2 h prepared by hydrazine HDP
4. **10% Co/SCNFH900 F80 NS 4:1 HDP**: Co catalyst supported on CNF functionalized using H_2SO_4 and HNO_3 at 80 ℃ for 2 h prepared by urea HDP
5. **10% Co/SCNFH900 F85 4HRS HDP**: Co catalyst supported on CNF functionalized at 85 ℃ for 4 h prepared by urea HDP.

5.1.3.1 TEM analysis

TEM analysis was employed to determine whether the catalyst particles were truly supported on the CNF supports and to also obtain a rough estimate of the metal particle sizes loaded on the CNFs. The first three catalysts supported on the low surface area CNFs, although prepared using different loading techniques, all displayed large metal aggregates (with particle sizes up to 100 nm circled with red circles) on the CNFs. Some of the metal aggregates were not even supported on the CNFs (Figure 5.2-5.4). These catalyst supports thus gave a very poor dispersion of the Co. The reason for the poor loading of Co metal is due to the inertness of the CNFs; thus relates to the functionalization methods employed on these CNFs supports. The CNFs employed for the three catalysts had low surface areas (Chapter 4) with low pore volumes which showed that the moderate functionalization conditions were not severe enough and thus there was not enough anchoring sites for the deposited metal nanoparticles on the CNFs (i.e SCNF H900 F80 2 hrs). It has been observed that unfuntionalized carbon nanomaterials are poor catalyst supports **[6]**, and this study vindicates such results. Even though the CNFs were not graphitic it

is clear that they still needed strong oxidation techniques to serve as good supports for the Co metal.

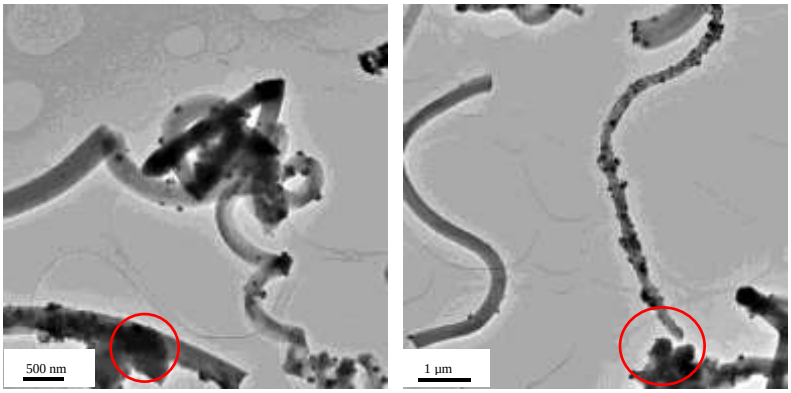


Figure 5. 2: TEM images of 10% Co/SCNFH900 F80 2hrs IWI

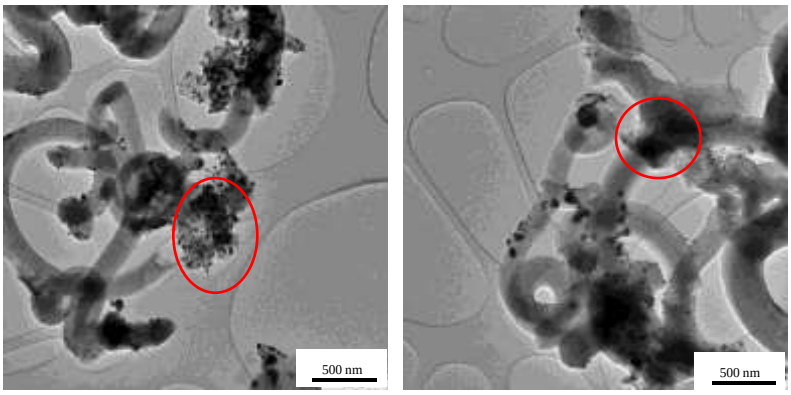


Figure 5. 3: TEM images of 10% Co/SCNFH900 F80 2hrs HDP

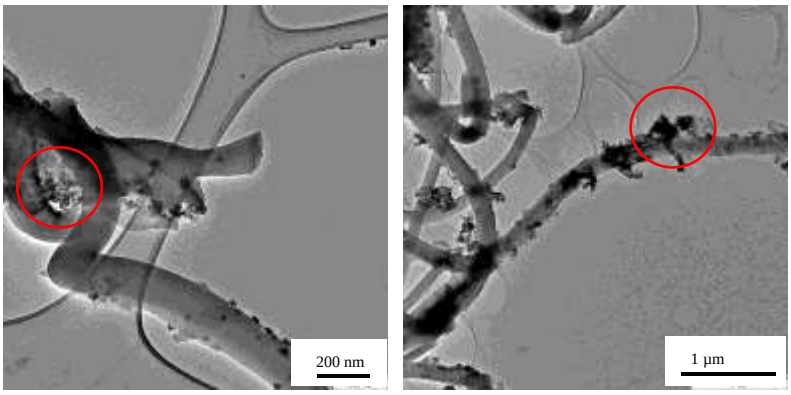


Figure 5. 4: TEM images of 10% Co/SCNFH900 F80 2hrs N_2H_4 HDP

To obtain a good loading of the Co metal on the CNFs, high surface area supports (i.e. the well functionalized CNFs) were used. TEM images of the two catalysts (i.e. 10% Co/SCNFH900 F80 NS 4:1 HDP and 10% Co/SCNFH900 F85 4HRS HDP) prepared by urea HDP are shown in Figure 5-6. The TEM images of these catalysts showed a sharp contrast from the catalysts shown in Figure 5.5-5.6. The Co metal nanoparticles were easily loaded and supported on the CNFs with estimated particles sizes of less than 20 nm (Table 5.1). This shows that harsh functionalization on the CNFs (although not highly graphitic) was required to improve the support capabilities.

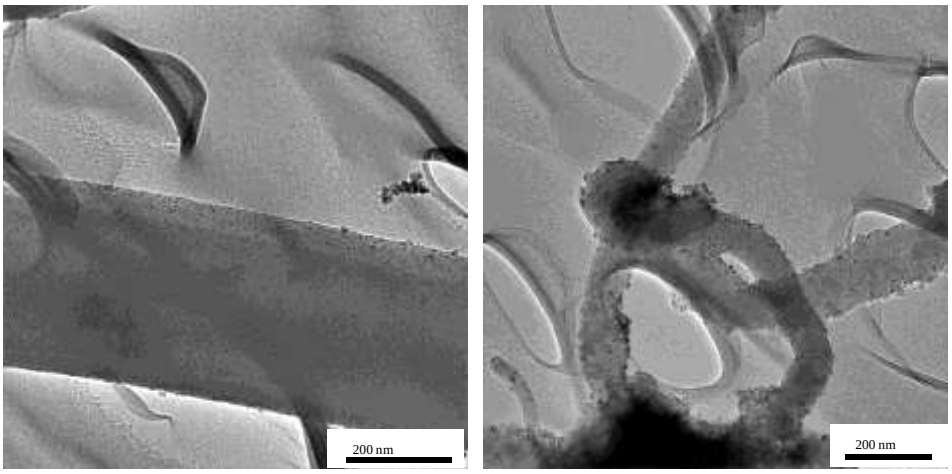


Figure 5. 5: TEM images of 10% Co/SCNFH900 F80 NS 4:1 HDP

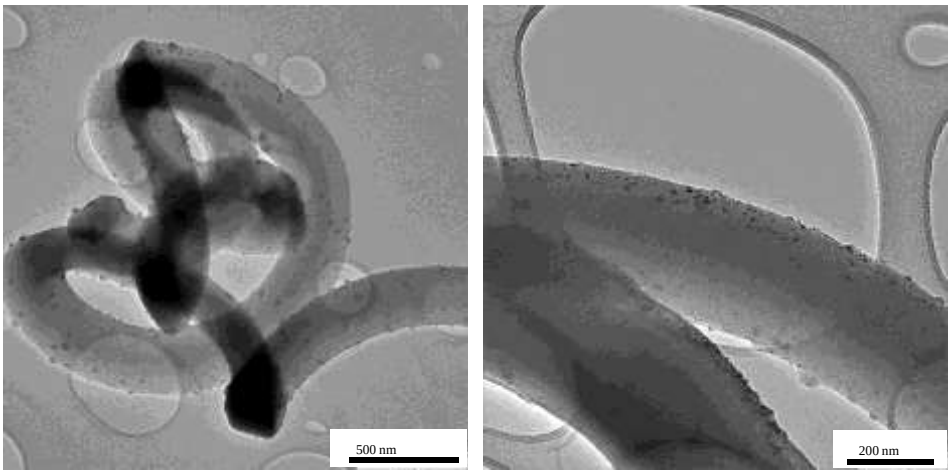


Figure 5. 6: TEM images of 10% Co/SCNFH900 F85 4HRS HDP

5.1.3.2 Cobalt phase analysis using XRD

From the XRD studies of the catalysts it was observed that after calcination all of the supported Co on the CNFs was in an oxide phase viz CoO or Co_3O_4 (elucidated using Ewa software and comparison of data for cobalt oxides, ICSD # **069374** and NIST **# N AL3340 2959**). The spinel Co_3O_4 phase appeared in very high proportions in the three catalysts which had large particle aggregates and poor dispersion (seen in Figure 5.2-5.4). However the two catalysts, 10% Co/SCNFH900 F80 NS 4:1 HDP and 10% Co/SCNFH900 F85 4HRS HDP prominently displayed the Co (II) oxide phase. The XRD patterns (Figure 5.7) therefore indicates that the catalysts were oxidised differently during the calcination process which can be related to the particle sizes on the different catalysts supports and the way in which the metal particles are bound on the CNFs surface.

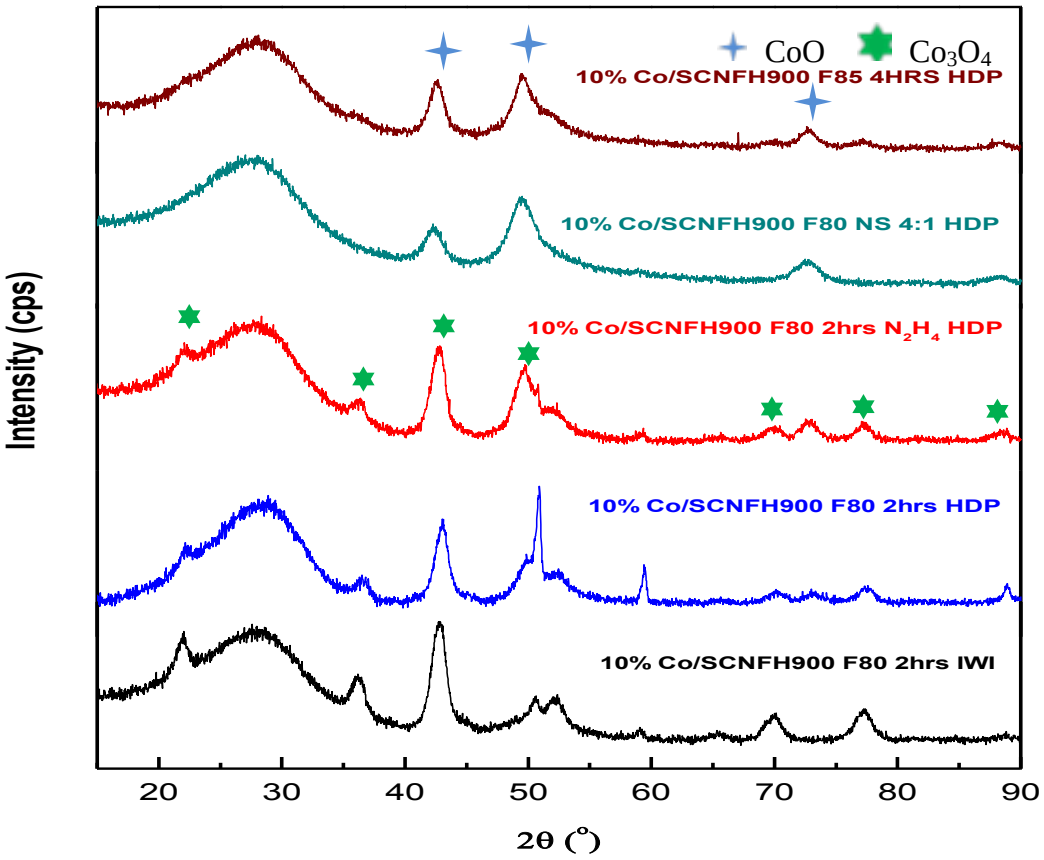


Figure 5. 7: XRD patterns of the different FT catalysts.

Table 5. 1: Co metal loading and particle sizes of the catalysts.

Sample name	Loading (%)	Actual loading (%)[a]	Average particle size (nm)		Oxide phase
			TEM	XRD	
10%Co/SCNFH900 F80 2hrs IWI	10	9.98	nq	7	Co_3O_4
10%Co/SCNFH900 F80 2hrs HDP	10	10.55	nq	8	
10%Co/SCNFH900 F80 2hrs N_2H_4 HDP	10	9.25	nq	7	
10% Co/SCNFH900 F80 NS 4:1 HDP	10	7.64	9	6	CoO
10% Co/SCNFH900 F85 4HRS HDP	10	9.76	10	8	

a- Analysis performed using ICP-OES, nq- not quantifiable size range to large (10-300 nm)

The catalysts (10%Co/SCNFH900 F80 2hrs IWI, 10%Co/SCNFH900 F80 2hrs HDP and 10%Co/SCNFH900 F80 2hrs N_2H_4 HDP) with big Co particle sizes and large particle size distribution gave XRD particles sizes in the nano regime (Table 5.1). It can be concluded that the average XRD particle sizes of 7, 8 and 7 nm for these catalysts are not accurate because the Scherrer equation is only applicable to small metal nanoparticles with a relatively narrow particle sizes distribution

5.1.3.3 TPR analysis of the catalysts.

Reduction profiles of the catalysts are shown in Figure 5.8. The reduction temperature of the different catalysts ranged from 300-500 ℃. The catalysts that were supported on the less functionalised CNFs (i.e. 10% Co/SCNFH900 F80 2hrs IWI, 10% Co/SCNFH900 F80 2hrs HDP and 10% Co/SCNFH900 F80 2hrs N_2H_4 HDP) displayed two reduction peaks (see Table 5.2) because of the two-step reduction of the spinel Co_3O_4 to CoO and then Co **[7]**. The 10% Co/SCNFH900 F80 2hrs IWI catalyst has a small peak at 233 ℃ which can be attributed to the decomposition of some of the nitrate ions left over on the catalyst **[8]**. The first reduction ($Co_3O_4 \rightarrow$ CoO) of these catalysts occurs at approximate temperatures of 300 ℃, and the second reduction peak (CoO → Co) was observed at 400-470 ℃. It is therefore clear that the first three catalysts had similar reduction profiles, independent of the catalyst preparation method. The other two catalysts (10% Co/SCNFH900 F80 NS 4:1 HDP, 10% Co/SCNFH900 F85 4HRS HDP) having a high composition of the CoO phase could only show a single distinct reduction peak at around 350 ℃ signalling the conversion of CoO to Co.

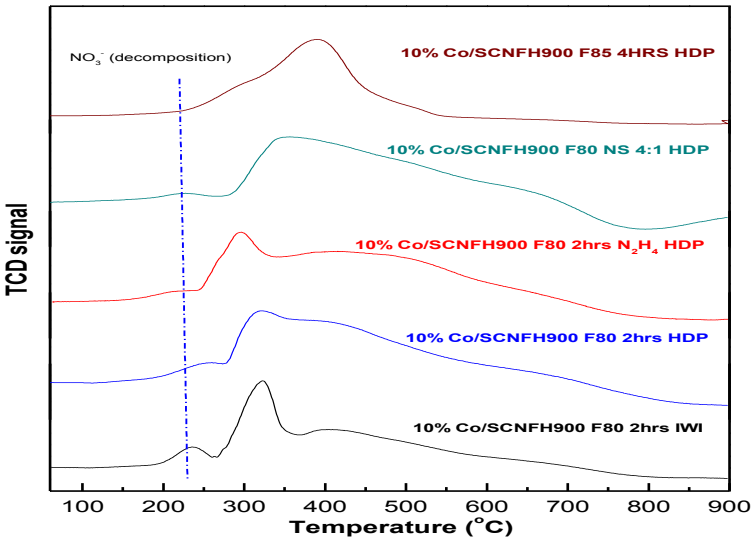


Figure 5. 8: TPR profiles of the Cobalt oxide phase

Table 5. 2: Reduction peaks of the Cobalt oxide phases

Sample name	First reduction peak (℃)	Second reduction peak (℃)
10% Co/SCNFH900 F80 2hrs IWI	321	403
10% Co/SCNFH900 F80 2hrs HDP	317	403
10% Co/SCNFH900 F80 2hrs N_2H_4 HDP	295	462
10% Co/SCNFH900 F80 NS 4:1 HDP	357	-
10% Co/SCNFH900 F85 4HRS HDP	390	-

5.1.3.4 Fischer-Tropsch catalytic performance of the catalysts

Selectivity and activity of the catalysts are given in Figures 5.9-5.10 and Table 5.3.

The first three catalysts (10% Co/SCNFH900 F80 2hrs IWI, 10% Co/SCNFH900 F80 2hrs HDP and 10% Co/SCNFH900 F80 2hrs N_2H_4 HDP) resulted in low Fischer-Tropsch activity (below 10% CO conversion). Poor dispersion of the metal particles on these CNFs (because the CNFs were not well functionalized and thus had weak anchoring sites) may be the reason why these three different catalysts displayed lower catalytic activity. The low number of exposed active sites that are responsible for dissociative adsorption of CO and H_2 of the syngas is responsible for these results. It is well documented that very weak metal support interactions lead to poor active metal dispersion **[9, 10]** resulting in undesirable FT activity of the catalysts.

Studies have shown a detailed relationship of FT catalyst particle sizes to their catalytic activity and selectivity when studying small Co particles (≤8 nm) **[1, 11, 12]**. Therefore for these catalysts the main parameter that resulted in the lower catalytic activity is the poor metal dispersion and the big Co particles sizes since lower dispersion is often associated with big metal particles sizes.

The last two FT catalysts supported on the optimally functionalized (CNFs (10% Co/SCNFH900 F80 NS 4:1 HDP and 10% Co/SCNFH900 F85 4HRS HDP) have very good Co nanoparticles anchored on the fiber structures and thus yielded good cobalt time yield data for the FT process. This is due to the fact that the Co nanoparticles are evenly dispersed and supported on the CNFs. Their catalytic activity in terms of percentage CO conversion was in the range of 28-35%. The improved activity of the catalysts is correlated to Co metal active sites with a particle size ranging from 4-10 nm which is known to be a typical particle size range for the study of Fischer-Tropsch synthesis **[1]**. The results confirm that good metal dispersion and smaller cobalt active sites are important for the catalyst system (dissociation, insertion and hydrogenation) to obtain a high activity. The results indicate that the CNFs subjected to a harsh functionalization procedure were ideal to serve as the Co catalyst supports (Figure 5.9). The catalysts 10% Co/SCNFH900 F85 4HRS HDP displayed cycling activity over the 120 h time on stream which may be due to poor heat distribution and wax covering the catalyst particles.

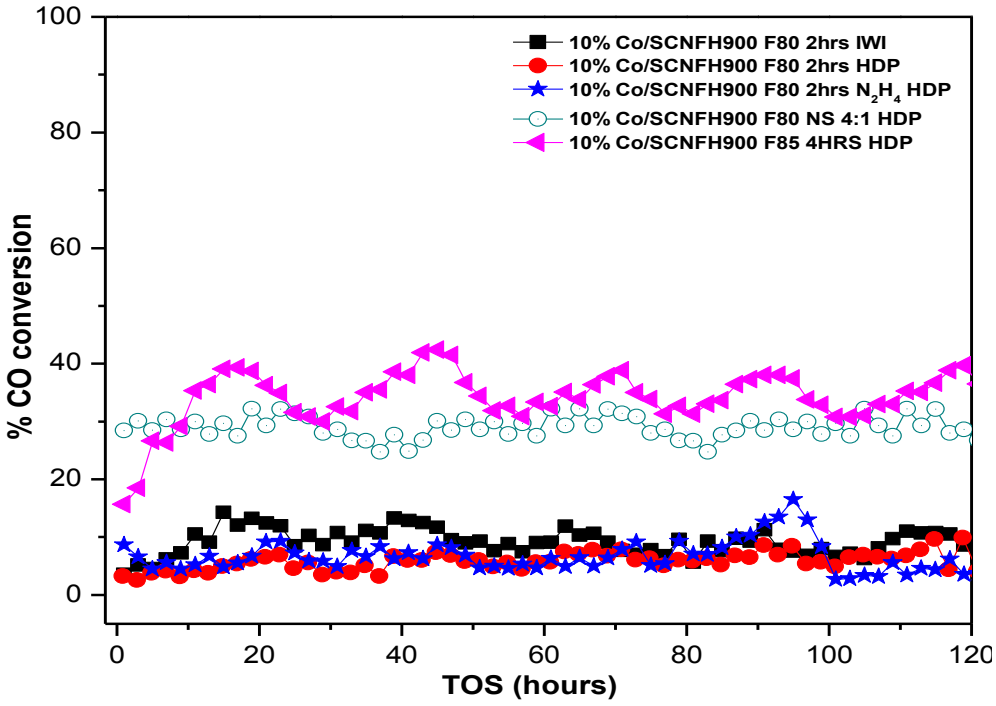


Figure 5. 9: Catalytic activity over 120 hours on stream

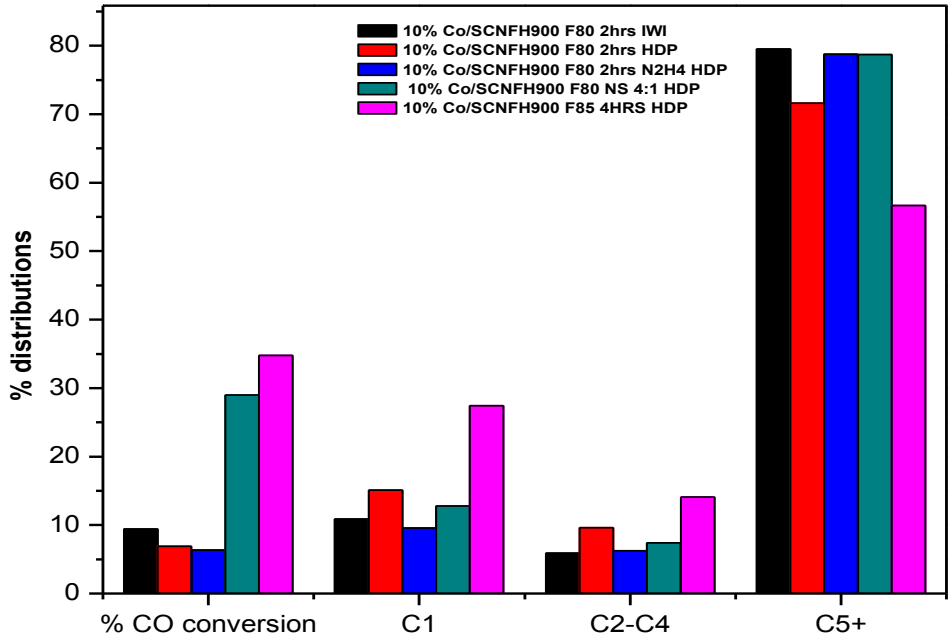


Figure 5. 10: Column chart showing difference in activities and selectivities.

Figure 5.10 and Table 5.3 show selectivities of the lower catalytic activity catalysts (10% Co/SCNFH900 F80 2hrs IWI, 10% Co/SCNFH900 F80 2hrs HDP and 10% Co/SCNFH900 F80 2hrs N_2H_4 HDP). The data is similar because at large Co metal particle sizes similar catalytic behavior under FT condition is expcted **[1, 11, 12]**. The catalysts showed low methane selectivity (9-15%) with greater than 65% C5+ selectivity. In contrast the catalyst 10% Co/SCNFH900 F85 4HRS HDP were highly selective to methane production (27%) and gaseous phase products (see Table 5.3). The high methane selectivity is attributed to the small cobalt crystallites supported on the CNFs. It is not clear why catalyst 10% Co/SCNFH900 F80 NS 4:1 HDP resulted in lower methane selectivity and higher C5+ in comparison to the catalyst 10% Co/SCNFH900 F85 4HRS HDP even though they displayed almost equal metal size distributions as seen from XRD and TEM images (Figure 5.5 and 5.6). The difference is however tentatively ascribed to the fact that catalyst 10% Co/SCNFH900 F80 NS 4:1 HDP is based on the CNFs functionalized using H_2SO_4 and some residual sulfur is left over in the CNFs serving as a promoter to lower the methane selectivity **[13]**.

Figure 5.11 shows the gas phase olefin to paraffin ratio of the five catalyst systems. It is seen that the low activity catalysts formed more olefin products when compared to the other two catalysts (CNFs (10% Co/SCNFH900 F80 NS 4:1 HDP and 10% Co/SCNFH900 F85 4HRS HDP). The distinct selectivities show that the catalysts followed different polymerization mechanism which can be associated with the H_2/CO ratio on the Co metal surface.

Table 5. 3: Fischer-Tropsch synthesis performance on the cobalt catalysts.

Catalyst	**% CO conversion**	**Product selectivity (mol %)**			
		C1	C2-C4	C5+	CO_2
10% Co/SCNFH900 F80 2hrs IWI	9.4	10.9	5.9	79.5	-
10% Co/SCNFH900 F80 2hrs HDP	6.9	15.1	9.6	71.6	-
10% Co/SCNFH900 F80 2hrs N2H4 HDP	6.3	9.6	6.2	78.8	-
10% Co/SCNFH900 F80 NS 4:1 HDP	29.0	12.8	7.4	78.7	-
10% Co/SCNFH900 F85 4HRS HDP	34.8	27.5	14.1	56.6	-

Syngas flow rate= 10 mL/min

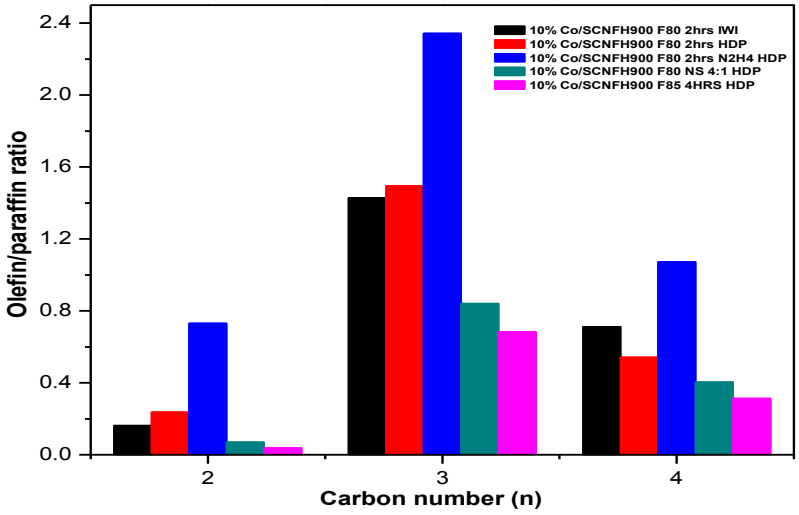


Figure 5. 11: Olefin to paraffin ratio of Co catalysts supported on carbon nanofibers.

5.1.4 Fischer Tropsch synthesis: Comparison of linear and helical CNFs as supports.

The Fischer-Tropsch synthesis was performed using CNFs with different morphologies (straight and helical) supports and annealed at 500 and 900 ℃. All the CNFs were functionalized using 55% HNO_3 for 4 hours at 85 ℃ which is just above the boiling point of HNO_3

The four catalysts were code named:

1. **10% Co/SCNFH500**: 10% cobalt supported on straight CNFs annealed at 500 ℃.
2. **10% Co/SCNFH900**: 10% cobalt supported on straight CNFs annealed at 900 ℃.
3. **10% Co/CCNFH500**: 10% cobalt supported on helical CNFs annealed at 500 ℃.
4. **10% Co/CCNFH900**: 10% cobalt supported on helical CNFs annealed at 900 ℃.

5.1.4.1 TEM analysis of the catalysts.

TEM analysis (Figure 5.12 and 5.13) of the CNF supported Co catalysts showed that the different CNFs were all capable of serving as supports for the metal nanoparticles. Some authors have also noted that both helical and straight fibers can serve as catalysts supports **[14, 15]**. The metal particle sizes on the different CNF supports ranged from 4-10 nm. Average cobalt metal particles supported of CNFs annealed at 900 ℃ were observed to be bigger than the particles sizes of Co metal supported on the CNFs annealed at 500 ℃. Catalyst 10% Co/SCNFH500 had Co crystallite sizes of 7 nm compared to 10 nm for the catalyst system 10% Co/SCNFH900. The same was observed for the helical CNFs with Co metal sizes on 10% Co/CCNFH900 and 10% Co/CCNFH900 at an average of 4 nm and 7 nm respectively. This difference in particle sizes arises because of the degree of functionalization on the fiber axis. The

CNFs annealed at 500 ℃ had increased functional groups (deduced from IR spectroscopy) and thus were able to disperse small Co nanoparticles better than the fibers annealed at 900 ℃. The helical CNFs were able to support the Co nanoparticles without any further breakages which were observed during the annealing process. The stability is also observed on the straight CNFs because these CNFs had no defects that arise due to the helical morphology.

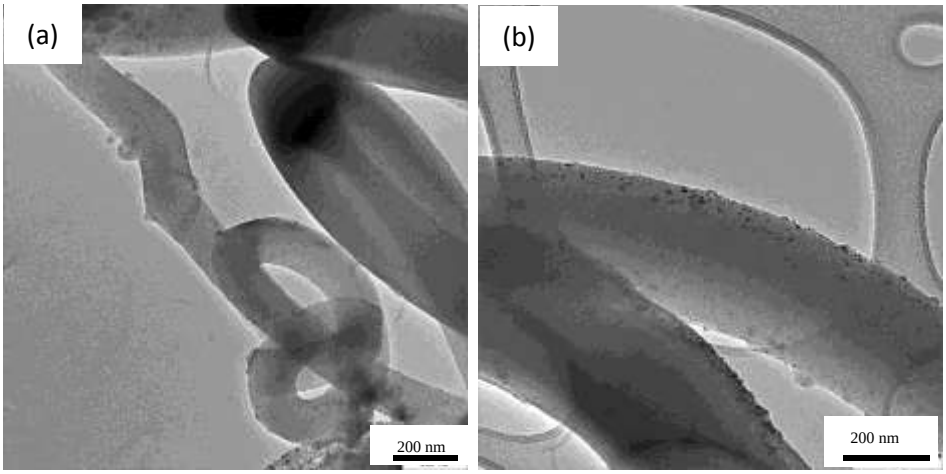


Figure 5.12: TEM images of Co supported on straight CNFs, (a) 10% Co/SCNFH500 and (b) 10% Co/SCNFH900

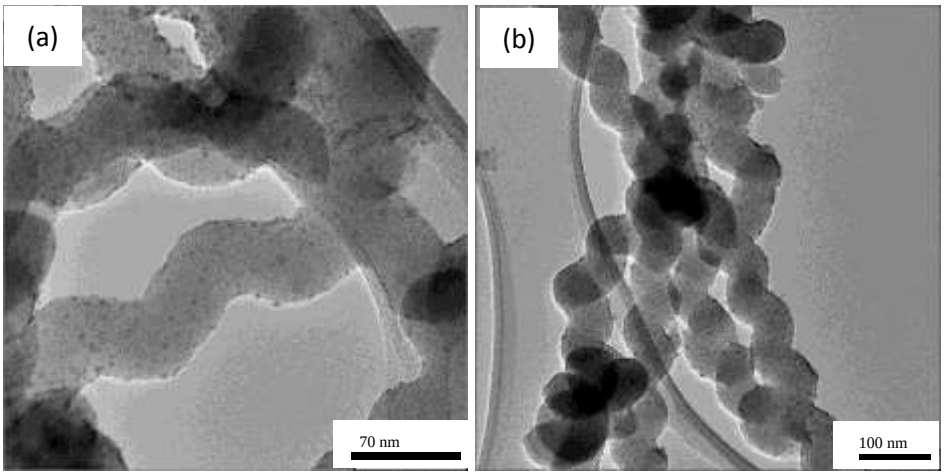


Figure 5. 13: TEM images of Co supported on helical CNFs, (a) 10% Co/CCNFH500 and (b) 10% Co/CCNFH900

5.1.4.2 XRD studies.

Co (II) oxide phases were the dominant phases on all four catalysts systems (Figure 5.14). The Co precursor were fully oxidised and all the nitrate counter ions were removed. The particles sizes calculated using the Scherrer equation (see Table 5.4) were similar to the size distribution seen from the TEM images. The broad peak at Bragg angle of 25^{o} shows that the CNFs are not fully graphitized and some of the CoO peaks overlap with the CNFs diffraction peaks (at 2θ= 43 and 50^{o}).

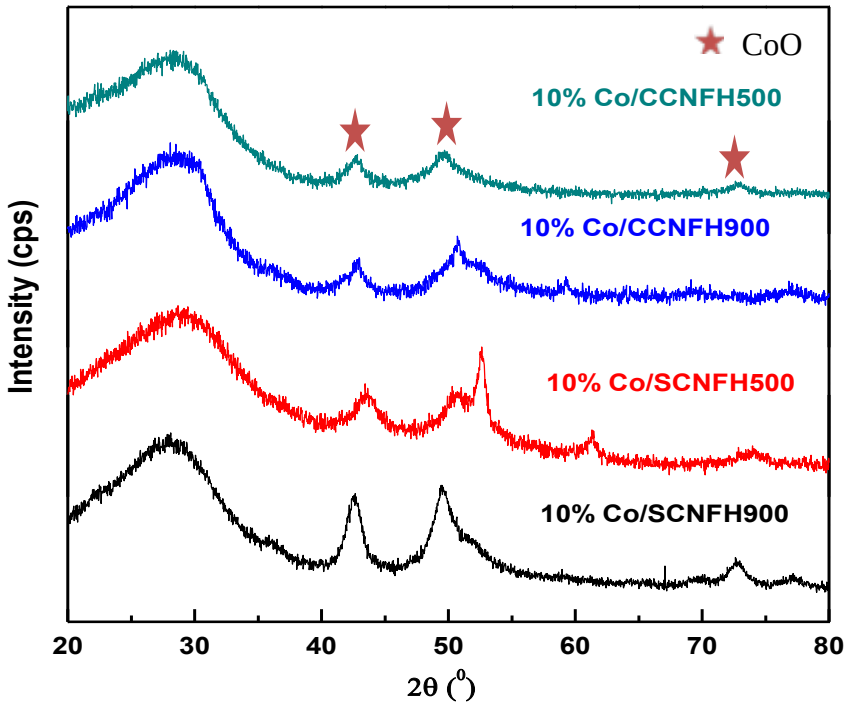


Figure 5. 14: XRD patterns of the catalysts using S/CCNF supports

Table 5. 4: Co metal loading and particle sizes of the catalysts.

Sample name	Loading (%)	Actual loading (%)[a]	Particle size (nm)	
			TEM	XRD
10% Co/SCNFH500	10	8.09	9	7
10% Co/SCNFH900	10	9.76	10	8
10% Co/CCNFH500	10	8.94	5	7
10% Co/CCNFH900	10	8.63	7	9

a- Analysis performed using ICP-OES.

XRD Co particles sizes (calculated by the Scherrer equation) and TEM images show good correlation.

5.1.4.3 Reduction profiles of the catalysts.

H_2-TPR analysis displayed a single major peak arising at temperatures ranging from 350-400 ℃, and therefore indicating a single reduction step from the CoO to Co (Figure 5.15) metal. XRD analysis also showed the CoO phase as the predominant phase in the catalysts systems. The reduction reaction is: $CoO \rightarrow Co$.

A second major negative peak is seen at temperatures above 700 ℃ arises from the gasification reaction of the carbon support **[6]**.

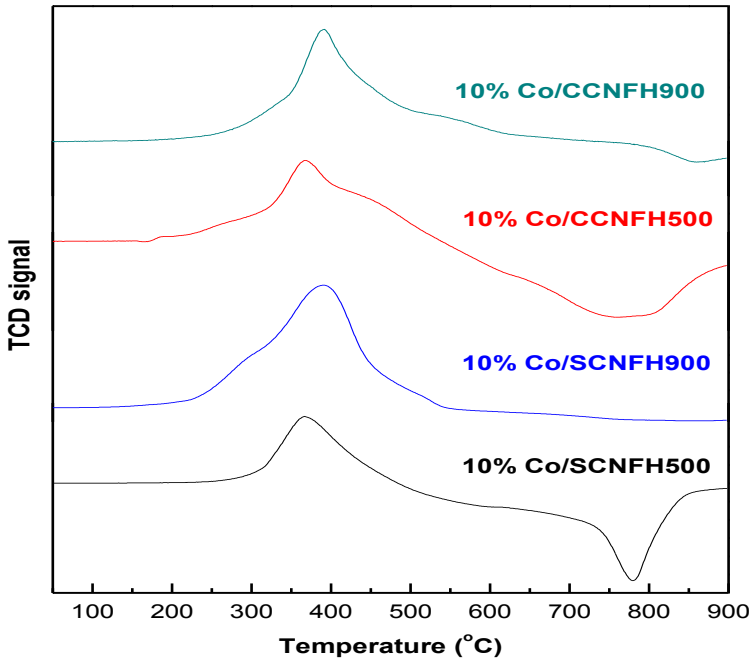


Figure 5. 15: TPR profiles Co catalysts supported on the annealed straight and helical CNFs

Table 5. 5: Reduction peaks of the catalysts.

Sample name	First reduction peak (℃)
10% Co/SCNFH500	367
10% Co/SCNFH900	390
10% Co/CCNFH500	364
10% Co/CCNFH900	385

5.1.4.4 Fischer-Tropsch reactor studies.

Catalytic evaluation of the systems was performed for a period of 120 hours. Pseudo-steady state activity was observed after (~20 h) for all the catalysts (Figure 5.16 (a) and (b)). The Co nanoparticles supported on CNFs annealed at 500 ℃ had ±15 % higher activity to CO conversion than the catalysts supports annealed at 900 ℃. The catalyst 10% Co/SCNFH500 and 10% Co/CCNFH500 had average percentage CO conversions of 38 and 40% respectively. The conversions were lower for the catalyst 10% Co/SCNFH900 and 10% Co/CCNFH900 yielded approximately 30% CO conversion. The results therefore show the different support morphologies, both helical and straight, did not have any fundamental effect on the Co active sites during the FT process, This was not unexpected because characterization by different techniques of the annealed CNFs (spectroscopy, XRD and BET) gave results that showed the fundamental properties of the CNFs were similar to each other. However, a small effect is observed when the CNFs are annealed at different temperatures (i.e. at 500 and 900 ℃). This difference may be because the CNF annealed at 900 contained only sp^2 carbon, and the CNFs annealed at 500 had both sp^2 and sp^3 hybridized carbon. The presence of sp^3 carbon serves as good metal anchors (because they were easily functionalised) for the Co particles which then prevents metal agglomeration during heat treatment (i.e. the reduction step) and during the FT synthesis. The Co particles supported on the CNFs annealed at 500 ℃ remained smaller that the Co particles supported on the CNFs during the FT process and thus keeping high activity over 120 h.

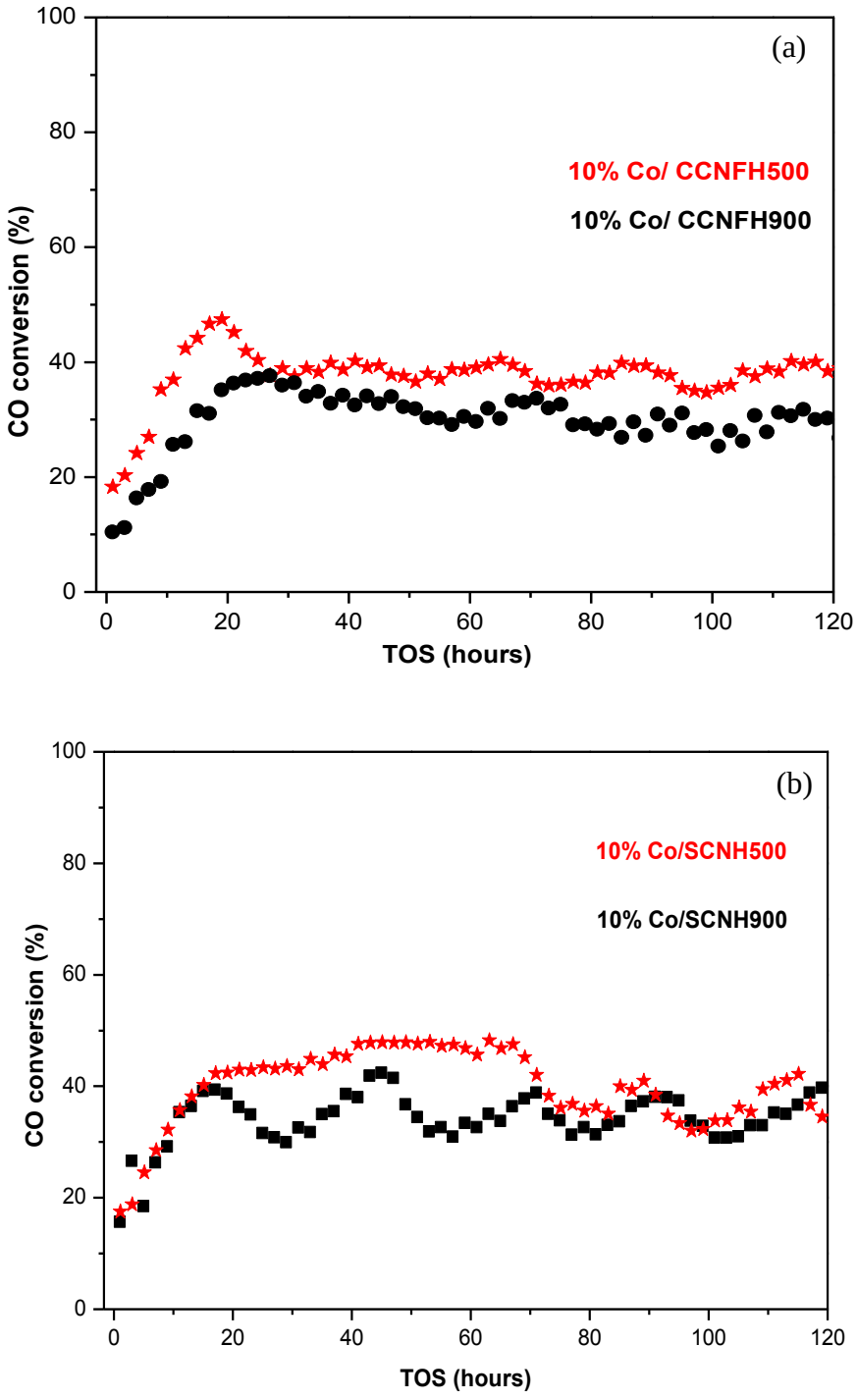


Figure 5. 16: Activity of the catalysts over 120 hours on stream (a)10% Co/SCNFH500 and 10% Co/SCNFH500, (b) 10% Co/CCNFH500 and 10% Co/CCNFH900

From Figure 5.17 and Table 5.6, it can be seen that the catalytic selectivity of the four catalysts showed high activity towards methane selectivity (> 15%). Xiong et al. **[15, 16]** also obtained high methane selectivity on the high activity cobalt catalysts supported on carbon nanomaterials. This high activity of the catalysts towards methane production is associated with the small metal particle sizes (i.e. by high H_2 coverage on the small Co crystallites) because of the electronic effects associated with the quantum effects associated with small nanoparticles **[17, 18]**. The Co on the helical CNF supports showed higher methane selectivity than the Co on the straight CNF supports (Table 6). The four catalysts also have approximately equal activity towards gas phase products with that Co supported on the straight CNFs annealed at 500 ℃ giving a better C5+ selectivity than all the other catalysts. The straight CNFs therefore had better selectivity than their helical counterparts. This could relate to the observation that the straight CNFs were robust and did not break into smaller pieces during the annealing and functionalization process and thus their structure and pore structure was less compromised during annealing.

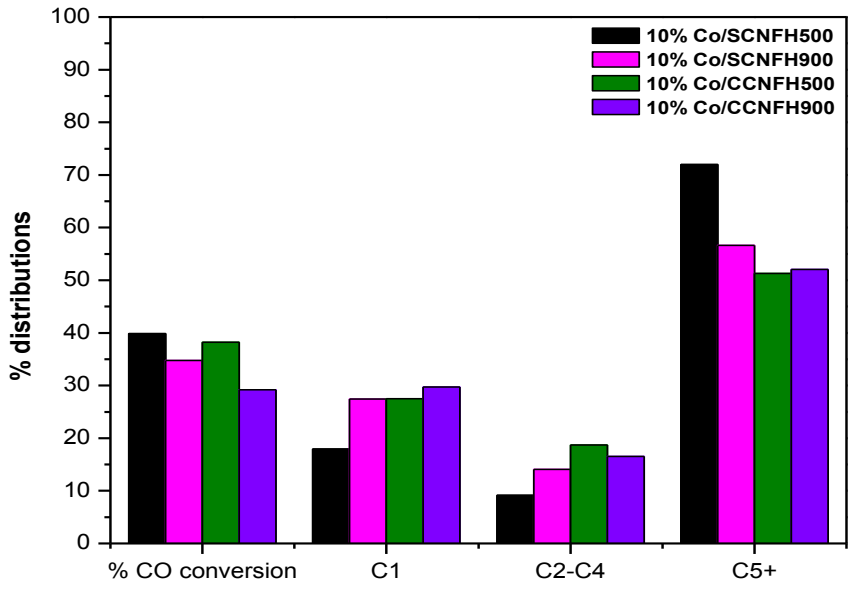


Figure 5. 17: Average activities and selectivities of the FT catalysts

Table 5. 6: Catalytic performance of Co supported on the straight an helical CNFs

Catalyst	**% CO conversion**	**Product selectivity (mol %)**			
		C1	C2-C4	C5+	CO_2
10% Co/SCNFH500	39.8	18.0	9.1	72.0	-
10% Co/SCNFH900	34.8	27.4	14.1	56.6	-
10% Co/CCNFH500	38.2	27.5	18.7	51.3	-
10% Co/CCNFH900	29.2	29.7	16.5	52.1	-

Syngas flow rate= 10 mL/min

5.1.4.5 Concluding remarks

CNFs were used as catalysts supports for Fischer-Tropsch synthesis. CNFs (both straight and helical) annealed at 500 and 900 ℃ were chosen as the preferred supports because of their high surface area and better thermal stability. The CNF, although not highly graphitized, showed that they still required harsh functionalisation procedures. CNFs functionalised at moderate conditions led to poor dispersion of the Co metal on the support. The Co supported on both the helical and straight CNFs (after optimised functionlaisation) showed high CO conversion activity. The catalysts also displayed high activity to methane production because of the small cobalt particle sizes.

5.1.5 References

1. Bezemer GL, Bitter JH, Kuipers HP, Oosterbeek H, Holewijn JE, Xu X, Kapteijn F, van Dillen AJ, de Jong KP: **Cobalt particle size effects in the Fischer-Tropsch reaction studied with carbon nanofiber supported catalysts**. *Journal of the American Chemical Society* 2006, **128**(12):3956-3964.
2. Keyser MM, Prinsloo FF: **Loading of cobalt on carbon nanofibers**. *Studies in surface science and catalysis* 2007, **163**:45-73.

3. Bezemer G: **Cobalt supported on carbon nanofibers as catalysts for the Fischer-Tropsch synthesis,** Utrecht University; 2006.
4. Bezemer GL, Falke U, van Dillen AJ, de Jong KP: **Cobalt on carbon nanofiber catalysts: auspicious system for study of manganese promotion in Fischer–Tropsch catalysis**. *Chemical Communications* 2005(6):731-733.
5. Díaz JA, Martínez-Fernández M, Romero A, Valverde JL: **Synthesis of carbon nanofibers supported cobalt catalysts for Fischer–Tropsch process**. *Fuel* 2013 (in press).
6. Motchelaho AMM: **Iron and cobalt catalysts supported on carbon nanotubes for use in the Fischer-Tropsch synthesis**. Faculty of Engineering and the Built Environment, University of the Witwatersrand; 2011.
7. Song D, Li J: **Effect of catalyst pore size on the catalytic performance of silica supported cobalt Fischer–Tropsch catalysts**. *Journal of Molecular Catalysis A: Chemical* 2006, **247**(1):206-212.
8. Song H, Zhang L, Ozkan US: **Effect of synthesis parameters on the catalytic activity of Co-ZrO2 for bio-ethanol steam reforming**. *Green Chemistry* 2007, **9**(6):686-694.
9. Soled SL, Iglesia E, Fiato RA, Baumgartner JE, Vroman H, Miseo S: **Control of metal dispersion and structure by changes in the solid-state chemistry of supported cobalt Fischer–Tropsch catalysts**. *Topics in catalysis* 2003, **26**(1-4):101-109.
10. Khodakov AY: **Enhancing cobalt dispersion in supported Fischer-Tropsch catalysts via controlled decomposition of cobalt precursors**. *Brazilian Journal of Physics* 2009, **39**(1A):171-175.
11. Prieto G, Martínez A, Concepción P, Moreno-Tost R: **Cobalt particle size effects in Fischer–Tropsch synthesis: structural and< i> in situ</i> spectroscopic characterisation on reverse micelle-synthesised Co/ITQ-2 model catalysts**. *Journal of Catalysis* 2009, **266**(1):129-144.
12. Borg Ø, Dietzel PD, Spjelkavik AI, Tveten EZ, Walmsley JC, Diplas S, Eri S, Holmen A, Rytter E: **Fischer–Tropsch synthesis: cobalt particle size and**

support effects on intrinsic activity and product distribution. *Journal of Catalysis* 2008, **259**(2):161-164.

13. Tsakoumis NE, Rønning M, Borg Ø, Rytter E, Holmen A: **Deactivation of cobalt based Fischer–Tropsch catalysts: a review**. *Catalysis Today* 2010, **154**(3):162-182.
14. Hu G, Nitze F, Barzegar HR, Sharifi T, Mikołajczuk A, Tai C-W, Borodzinski A, Wågberg T: **Palladium nanocrystals supported on helical carbon nanofibers for highly efficient electro-oxidation of formic acid, methanol and ethanol in alkaline electrolytes**. *Journal of Power Sources* 2012, **209**(0):236-242.
15. Xiong H, Motchelaho MA, Moyo M, Jewell LL, Coville NJ: **Cobalt catalysts supported on a micro-coil carbon in Fischer–Tropsch synthesis: A comparison with CNTs and CNFs**. *Catalysis Today* 2012.
16. Xiong H, Motchelaho MAM, Moyo M, Jewell LL, Coville NJ: **Correlating the preparation and performance of cobalt catalysts supported on carbon nanotubes and carbon spheres in the Fischer–Tropsch synthesis**. *Journal of Catalysis* 2011, **278**(1):26-40.
17. den Breejen J: **Cobalt particle size effects in catalysis,** Utrecht University,. 2010.
18. van Dijk HAJ: **The Fischer-Tropsch synthesis: A mechanistic study using transient isotopic tracing**: Technische Universiteit Eindhoven Eindhoven; 2001

Chapter 6: General conclussions and reccomendations

6.1 Conclusions

The aim of the study was to synthesize carbon nanofibers using copper nanoparticles and then use the carbon as catalyst supports for the Fischer-Tropsch process. Using characterization techniques such as TGA, TPR, TEM, XRD, FTIR and Raman spectroscopy etc. the following conclusions are drawn from these studies:

Control of the copper oxide particle sizes to be used as catalysts for producing CNFs was studied, Surface area studies using nitrous oxide chemisorption of the reduced Cu nanoparticles remains high showed that the CuO did not sinter during reduction.

Carbon nanofibers grown on the Cu catalysts resulted in two morphologies, helical and straight CNFs were grown on the small supported copper Cu and the large Cu catalysts respectively. The CNF yield from these catalysts was up to 60% acetylene conversion. All the as synthesized CNFs are amorphous with a characteristic brown color.

Annealing of the CNFs at 500, 900 and 1400 ℃ increased the thermal stability and structural robustness of the carbon. The annealing of CNFs did not convert them to highly graphitized carbon because of topological defects present in the CNFs and possibly because the annealing temperatures were not high enough. Annealing also improved the CNF surface area generating carbon with a mesoporous nature after heat treatment.

The CNFs were purified to remove Cu particles and functionalized using nitric acid, however the CNFs, although not highly graphitic, still needed harsh functionalization

conditions to improve the surface activity (interaction) and surface area of the materials for application as catalyst supports.

The properly functionalized carbon nanofibers (both helical and straight CNFs) were used as catalyst supports and displayed good Co loading and dispersion on the CNFs surface.

Comparison of Fischer Tropsch activity of Co supported on CNFs annealed at 500 and 900 ℃ showed that Co supported on CNFs annealed at 500 ℃ showed better CO conversion than the Co supported on CNFs annealed at 900 ℃.

The activity and selectivity of Co supported on the straight and helical CNFs did not show any significant difference due to support effects associated with the different CNF morphologies. All these catalysts displayed high methane selectivity.

6.2 Recommendations

The helical carbon nanofibers broke during higher temperature annealing of > 900 ℃ at atmospheric pressure, thus it is suggested that annealing of the CCNFs under vacuum can be employed to avoid the breaking of the helical carbon nanofibers.

Annealing of the polymeric carbon nanofibers will require very high annealing temperatures (possibly >1500 ℃) to generate highly graphitic carbon nanofibers, especially the straight carbon nanofibers which did not break under high temperature treatment.

The application of the annealed CNFs still require greater understanding on the functionalization and pretreatment processes since it has been observed that the supported cobalt nanoparticles were highly selective to methane.